Universitat Politècnica de Catalunya

Institut de Tècniques Energètiques

Contributions to new challenges in radiotherapy. From Small Field Dosimetry to Stereotactic Body Radiation Therapy

Thesis dissertation defended by

Josep Puxeu Vaqué

Nuclear Engineering and Ionising Radiation PhD programme

Thesis Advisors: Dr. Mercé Ginjaume
and Dr. M Amor Duch

November, 2015

Als meus pares

UNIVERSITAT POLITÈCNICA DE CATALUNYA
BARCELONATECH
Escola de Doctorat

Curs acadèmic:

Acta de qualificació de tesi doctoral

Nom i cognoms
JOSEP PUXEU VAQUÉ

Programa de doctorat
ENGINYERIA NUCLEAR I DE LES RADIACIONS IONITZANTS

Unitat estructural responsable del programa
INSTITUT DE TÈCNIQUES ENERGÈTIQUES

Resolució del Tribunal

Reunit el Tribunal designat a l'efecte, el doctorand / la doctoranda exposa el tema de la seva tesi doctoral titulada ____ ____.

Acabada la lectura i després de donar resposta a les qüestions formulades pels membres titulars del tribunal, aquest atorga la qualificació:

☐ NO APTE ☐ APROVAT ☐ NOTABLE ☐ EXCEL·LENT

(Nom, cognoms i signatura) President/a	(Nom, cognoms i signatura) Secretari/ària

(Nom, cognoms i signatura) Vocal	(Nom, cognoms i signatura) Vocal	(Nom, cognoms i signatura) Vocal

______________________, _______ d'/de _________________ de _______________

El resultat de l'escrutini dels vots emesos pels membres titulars del tribunal, efectuat per l'Escola de Doctorat, a instància de la Comissió de Doctorat de la UPC, atorga la MENCIÓ CUM LAUDE:

☐ SÍ ☐ NO

(Nom, cognoms i signatura) President de la Comissió Permanent de l'Escola de Doctorat	(Nom, cognoms i signatura) Secretari de la Comissió Permanent de l'Escola de Doctorat

Barcelona, _______ d'/de ____________________ de _________

Abstract

The use of small fields has substantially increased in radiotherapy during recent years mainly due to expansion in the use of modulated techniques which are also used at some institutions for Stereotactic Body Radiotherapy (SBRT). The use of modulated techniques in lung SBRT is controversial due to the interplay effect. At the same time, small-volume dosemeters have appeared on the market in an attempt to try to cover new dosimetry necessities.

This PhD deals with different features related to small-field dosimetry. It first analyzes the influence of differences between ionization chambers of the same type on dosimetry factors determining 0.5% as the upper limit on the possible influence. Correction factors for PTW-31016 are also proposed and the effect of a particular chamber of this model has been found to be up to 2.8% for 0.5 cm square. These correction factors have been determined by Monte Carlo calculations and have been validated with measurements on flattened and unflattened beams by analyzing the main sources of influence. The last chapter is devoted to SBRT, and suggests a fast and accurate plan set-up together with PUMA, a method to evaluate the interplay effect in lung SBRT.

Keywords: Correction factors, small field dosimetry, k_{Q,Q_o}, $k^{f_{clin},f_{msr}}_{Q_{clin},Q_{msr}}$, SABR, SBRT, Monte Carlo simulation, ionization chamber

Preface

Radiotherapy has evolved significantly in recent years. Probably the most relevant change, from a clinical point of view, is the implementation of extracranial radiosurgery called SBRT (Stereotactic Body Radiotherapy) or SABR (Stereotactic Ablative Radiotherapy). The appearance in 2010 of a task group from the American Association of Physics in Medicine (AAPM) and more than 5000 references related to this technique over the last five years shows its importance. At the beginning of 2000, prior to the expansion of SBRT, improvements in the precision of linear accelerators combined with the increase in calculation speed of computer systems has led to the emergence of Intensity Modulated Radiotherapy (IMRT) and later, in 2007, Volumetric Modulated Arc Therapy (VMAT), where intensity modulation is performed on an arc. Both techniques imply the use of small treatment fields defined for stereotactic irradiation or as segments in IMRT techniques. Due to the great increase in their use, a new approach to reference dosimetry of small fields was proposed in 2008 since existing codes of practice were not designed to successfully cover small-field dosimetry. The most notable point of the new approach is the definition of a new correction factor that must be applied to the different detectors when small-field determinations are performed. More than 400 references have appeared during the last five years referring to small-field dosimetry, and these can be divided between characterization of detectors in small-field dosimetry on a new machine and/or the proposal of correction factors for some detectors.

This thesis consists on the study of three different topics which aim to address some of the present challenges in radiotherapy. They can be divided between the effect of detector geometric tolerances within an ionization chamber on basic dosimetric parameters, determination of correction factors for a particular detector in a new linear accelerator and the influence of geometric tolerances on these correction factors. Finally, the development of a method to analyze the effect of VMAT on lung SABR treatments is proposed.

The text is structured with a general introduction in Chapter 1, the description of the materials and the details of Monte Carlo simulations are given in Chapter 2. Chapter 3 describes the methodology used for the study of the three topics and Chapters 4 to 6 present the results and discussion of each of the topics. Finally, conclusions are summarized in Chapter 7.

Acknowledgments

Aquesta tesi constitueix el resultat de molts anys de recerca. Durant aquest llarg període han estat moltes les persones que, de manera més o menys directa han contribuït al fet que aquest escrit veiés finalment la llum. A tots vosaltres, us estic molt agraït i intentaré incloure-us en els següents paràgrafs.

En primer lloc, vull agrair a la meva tutora Dra. Mercè Ginjaume, per acceptar-me en el programa de doctorat i animar-me a fer la tesi un cop superada la suficiència investigadora. També a la Dra. M Amor Duch que acceptés ser cotutora dels meus treballs. Us estic molt agraït per la vostra dedicació i la vostra paciència.

Permeteu-me que dediqui els primers paràgrafs a aquelles persones que han fet que pogués arribar a començar la tesis.

Vull agrair als meus pares i als meus germans Jordi i Miquel tot el que heu fet per mi per tal que estudiés la carrera, així com el suport que em vau donar quan vaig decidir reorientar la meva vida i dedicar-me a la física mèdica. A tu, papa, per ensenyar-me a donar a les coses la importància que tenen i a perseverar en les adversitats; i a tu, mama, pel teu esperit positiu i la teva força en afrontar i superar qualsevol repte.

Si mirem enrere vull recordar alguns dels companys de la facultat que, durant aquells anys, vam compartir moltes discussions i apunts (eh, Nacho) i que, després, el temps ens ha distanciant, Valentí, Francesc, Germán, Santi, Manolo, Carlos, Cito... i d'una manera molt especial als que hem mantingut i enfortit l'amistat: els dos Davids, el Sergi, el Ferran, el Javi i, evidentment, també a tu, Neus, perquè és una sort gaudir de la vostra amistat i mantenir discussions sobre qualsevol tema.

Els primers anys de feina com a docent a Tarragona em varen ajudar a formar-me com a persona. Dels dos centres on vaig estar podria recordar a tots els companys de claustre i molts dels alumnes. M'agradaria, però, anomenar la Cinta, la Marisol, la Margarida, el Borja... Quan vaig començar tenia vint-i-dos anys i vosaltres vau ser una bona ajuda. També recordo de manera molt entranyable els sopars/discussions amb el Pere Pardines i el bon fer de Mn Gimenez... No m'oblido de tu, Noemi: te n'has lliurat perquè, la tesis, l'he escrit en anglès; si no, t'hauria demanat que la corregissis tota... Granell, les teves classes d'anglès també han estat importants i han facilitat moltes de les coses que he fet. Aquest paràgraf podria ser molt més llarg, ja que vosaltres (Jose, Ismael, Lluis Albert) també esteu cridats a aparèixer en els agraïments.

Aquesta tesis es conseqüència d'haver cursat l'especialitat de radiofísica, els primers passos en la descoberta d'aquest món els he d'agrair a dues persones: el Manel i el Víctor. A tu, Manel, per confiar en mi i permetre'm descobrir l'especialitat; i a tu, Víctor, per orientar-me en la preparació de l'examen. Gràcies a tots dos, no només pel que he escrit, sinó per l'ajuda i suport durant aquests anys.

Gràcies Carme per donar-me suport per preparar-me l'examen de l'especialitat i animar-me a començar la tesi. El temps ens ha dut per camins diferents, però sempre tindrem el suport que necessitem l'un de l'altre.

Vull deixar constància que aquest treball no hagués estat possible sense la M. Cruz Lizuain. Desde que llegué al hospital como residente siempre te mostraste dispuesta a escuchar y explicarme todo lo que se me ocurría. Me animaste a empezar esta aventura y desde entonces me has ayudado en todo lo que has podido. Me siento enormemente afortunado de poderme considerar amigo tuyo y quiero agradecerte públicamente los conocimientos que me has transmitido, las innumerables discusiones sobre cualquier tema, las correcciones de textos, los ánimos para emprender la experiencia escocesa, las cenas y botellas de vino invertidas para que esta empresa llegase a buen puerto y tantas y tantas cosas.

Quiero agradecer también al Dr. Pedro Andreo por ayudarme y guiarme en el estudio de la influencia de la geometria de las cámaras en los factores de corrección y por su paciencia en el largo proceso de simulación.

Fou en un congrés a Maastricht on, Imma, vas tenir la mala sort que ens coneguéssim. Des d'aquell moment em vaig convertir en el pesat que preguntava sobre com instal·lar PENELOPE al clúster, com parar simulacions que el col·lapsaven... Ja et vaig dir que si això mai s'acabava tindries un paràgraf per tu als agraïments. Moltes gràcies per la teva bona ajuda, a qualsevol hora . Parlant del clúster i tot i que sembla que al final hem tingut un molt mal desenllaç, vull agrair al Josep Pujal la seva paciència i el seu bon fer en la gestió i solució dels problemes del clúster i demanar perdó als companys de simulació als quals, inicialment i per desconeixement, havia endarrerit les seves simulacions.

Vull agrair també als companys del Servei de Física el seu suport durant tots aquests anys, a la Cristina, per animar-me sempre, al Rodolfo, per les discussions i les lliçons de futbol els dilluns; a l'Ignasi, per solucionar i explicar-me qualsevol tema informàtic; a l'Ismael, el meu resident referent amb el que ja varem començar fent el poster de la PinPoint fa anys; al Paco, company d'hores extra de tesi; al Pablo, *es estadísticamente significativa la correlación?*, i a la resta del servei pel vostre suport, especialment al "*turno tarde*" que m'heu arribat a portar menjar a l'accelerador mentre mesurava. Biel i Albert, gràcies també per la introducció al LaTex; a la Maite, per animar-me sempre, i també a la Sara, perquè "*tus erres pequeños, que te costaban criar, se hacen mayores*"..

I would like to express my sincere gratitude to people from Clatterbridge Hospital for their hospitality during my stage as a trainee, I deeply appreciate their time. Thanks to all of you, especially Philip, Helen, Allan Gately, Alison, Alan Nahum, Vanessa, Sue.

A very special thanks goes to Terry Kehoe and Sara Serridge for trusting me with the implementation of SABR project. I deeply acknowledge, from the very beginning, their warm welcome and their support throughout my stay at the Edinburgh Cancer Centre. I am very greatful for having had the opportunity to be part of such a group. Working at ECC was one of the most fulfilling and rewarding experiences, I have ever had, both from a professional and personal point of view. I thank all my colleagues (and also friends) from ECC... You know perfectly the personal circumstances I lived during those twenty months, thanks to all of you for that magical time. Thanks to Jane for the 'comforting' badminton sessions... (*you lost the worst player when I left... who is it now?*) and to Sankar for your wonderful attitude, you were always willing to help me with anything. Will, you were the best neighbour ever I could have, just thanks for being you and let me know when we will start the revolution. Thanks to Barbara for your warmth and your Scottish lessons.

This work has had invaluable support from you Bill, without your help this work probably have got nowhere. Greatful thanks for the countless discussions in your office, endless corrections everywhere, and your great attitude and support, I feel indeed fortunate to have met you.

Gràcies també a les dues institucions (ICO i ECC), per facilitar-me l'equipament poder fer totes les mesures. I also grateful to both institutions (ICO and ECC) for the use of their facilities and equipment.

Vull agrair també als membres del tribunal i als revisors internacionals que acceptessin formar-ne part.

Gràcies també Jordi per les discussions i el *ROC,* i per confirmar amb un anàlisis molt elaborat, que el 5% era un bon paràmetre per avaluar el PUMA.

Gràcies també a tots vosaltres, Montserrat, Marta, la resta de la família i els amics de sempre. Valtros heu fet que tot això no fos tant dur com semblava facilitant que pogués desconnectar en qualsevol moment. Gràcies a la Núria a l'Ignasi, al Joan i a tu, Bruna, que ja tenim ganes de conèixe't, amb un somriure vostre torneu el verdader valor i sentit a les coses.

Finalment, gràcies a tu, Alba, companya de camí, per la teva actitud i el teu suport en aquesta darrera etapa de la tesi i per haver confiat sempre en mi. Amb tu tot és més fàcil. Ara que gairebé ja en tenim una, anem a per la teva...

Perdoneu si algú no se sent representat en aquests agraïments. De ben segur que he pensat en tu mentre escrivia la tesi. Durant aquests anys he desitjat molts cops acabar-la per poder donar-vos a tots les gràcies per escrit.

List of Abbreviations

AAA Anisotropical analytical algorithm

AAPM American Association of Physics in Medicine

ALPO Average leaf pair opening

BPM Breaths per minute

CPE Charged particle equilibrium

CTV Clinical target volume

DICOM Digital imaging and communications in medicine

DVO Dose Volume Optimizer

ECC Edinburgh Cancer Centre

FF Flattened filter (beams)

FFF Flattening filter-free (beams)

FOF Field output factor

GTV Gross tumour volume

IAEA International Atomic Energy Agency

ICO Institut Català d'Oncologia

IMRT Intensity modulated radiotherapy

INTE Institut de Tècniques Energètiques

LINAC Electron linear accelerator

MC Monte Carlo

MLC Multileaf collimator

MPD Medical physics department

OAR Off axis ratio

OR Output ratio

PDD Percentage depth dose

PSDL Primary standard dosimetry laboratory

PSF Phase space files

PTV Planning target volume

PUMA Predicted upshot motion analysis

Q Beam quality index

ROI Region of interest

RTOG Radiation Therapy Oncology Group

SAD Source-to-axis distance

SD Standard deviation

SDD Source detector distance

SSD Source-to-Surface distance

SSDL Secondary standard dosimetry laboratory

TG Task Group

TLD Thermoluminescent dosemeter

TMR Tissue maximum ratio

TPR Tissue phantom ratio

TPS Treatment planning system

TRS Technical report series

UPC Universitat Politecnica de Catalunya

VMAT Volumetric modulated arc therapy

Contents

List of Figures

List of Tables

Chapter 1

Introduction

Cancer is a general term used to refer to a condition where the body's cells begin to grow and reproduce in an uncontrollable way. These cells can then invade and destroy healthy tissue, including organs. More than one in three people will develop some form of cancer during their lifetime and, along with cardiovascular disease, are the most common cause of death. The treatment of cancer has become one of the most prominent world health issues due to both its prevalence and mortality. More than 50% of cancer patients will receive radiotherapy at some stage during the course of their illness [1, 2] and this may be combined with surgery and/or chemotherapy.

1.1 Basic radiotherapy concepts

Radiotherapy aims to eliminate or mitigate disease by delivering high doses of radiation to diseased tissue whilst minimising the dose to healthy tissue. The equilibrium between these variables has led to the development of new radiotherapy techniques. Developments in the diagnosis detection process including computed tomography (CT), positron emission tomography (PET) and magnetic resonance (MR) imaging provide the necessary threedimensional (3D) anatomical information prior to treatment. This process allows better delineation of tumoral zones and a reduction of irradiation volumes. Different types of radiation (photons, electrons, protons and ions) and a wide range of energies can be used in radiotherapy. Our work is centred on the use of external megavoltage photon beams generated on a electron linear accelerator (LINAC).

Linear accelerators producing wide flattened photon beams (FF) have been used in clinical practice for more than 50 years. Photon beams are created by the impact of a narrow monoenergetic electron beam on a target. The impact of this electron beam produces a wide photon beam after passing through the target, which has a wide spectrum of energies due to the different interactions produced within the target and geometrically it has a higher fluence in the centre of the beam.(Figure 1.1).

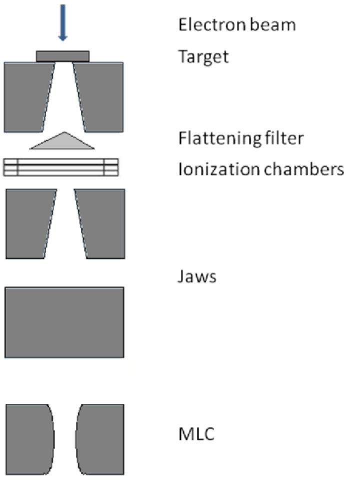

Figure 1.1: Basic linear accelerator scheme

Current conformed radiotherapy is based on the use of photon beams that are shaped by using two pairs of movable jaws situated perpendicularly allowing conformation of the radiation with asymmetric rectangles and the use of a multileaf collimator (MLC). The MLC is a device made up of individual "leaves" that can be positioned independently in the beam path in order to block it and create beam apertures with more irregular shapes allowing for a better conformation of the volume. (Figure 1.2)

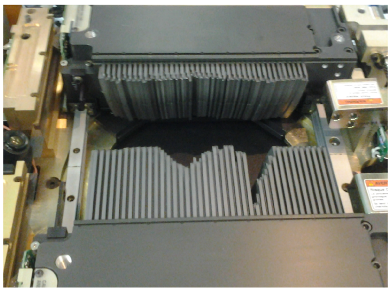

Figure 1.2: Multileaf collimator (MLC) from a Varian Medical Systems electron linear accelerator

In general, an homogeneous dose distribution on the planning target volume (PTV) is desired and consequently flattened (homogeneous) beams are an advantage. To create flattened beams, LINACs have a conical piece made of Cu, tungsten or stainless steel, called flattening filter, which when inserted in the path of the photon beam, reduces the photon fluence in the central part. The flattening filter is specific for each energy and has other important effects on the photon beam. It absorbs some of the photons with lower energy, which is a desired effect since photons with lower energies will tend to deposit their energy on the skin of the patient and, in general, photon beams are used to deliver doses to volumes that are within the body. However, flattening of the beam is achieved by absorbing part of the radiation in the central part and implies a reduction in the dose rate for the flattened beam compared with the unflattened beam.

To measure the amount of radiation delivered by the linear accelerator, a set of ionization chambers, called monitor chambers, are situated after the flattening filter. The chambers monitor the dose rate that the system delivers. In addition, these ionization chambers, strategically designed, also control other parameters of the beam. The Monitor Unit (MU) is defined as an arbitrary unit directly related with readings of the monitor chambers to measure the LINAC output. The equivalence between the MU and the dose delivered at a certain point will depend on each institution. A common equivalence is 100 MU corresponds to 1 Gy (see section 1.2.1) for a reference depth and field size under isocentric conditions with a fixed source-detector-distance (SDD) or with a fixed source-surface-distance (SSD). The most common photon energies used from a LINAC in radiotherapy range from 6 MV to 18 MV. For this range, the absorbed dose in water for a beam perpendicular to the surface follows a distribution in depth as presented in Figure 1.3.

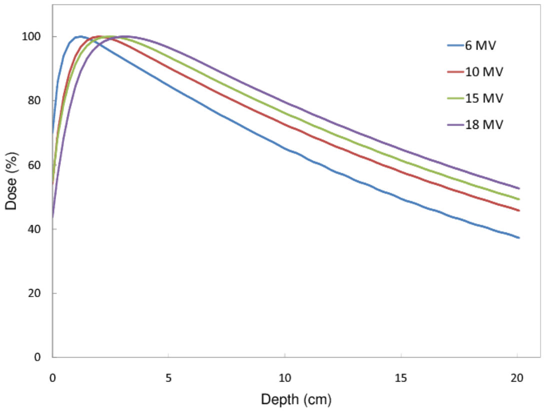

Figure 1.3: Percentage depth-dose profiles (PDD) for several photon energies for a square field of 10 cm side length

It can be observed that the maximum absorbed dose is situated at a certain depth which ranges from 1.2 cm to 4 cm approximately. The maximum absorbed depth dose not only depends on the energy, but also on the field size. To achieve an appropriate dose distribution in the tumoral volume while preserving the surrounding tissues, a combination of beams with different orientations and weights focused on the volume are used. This combination of orientations can also be created by using arcs centred on the tumour, which is known as arc-therapy, where one or more arcs are used. It is also possible to combine static beams and arcs in the same treatment plan. The appropriate combination of beam orientations and shapes makes it possible to achieve high dose to the target volume, whilst minimizing the doses to surrounding healthy tissue.

A reduction in computing time has enabled the development of new radiotherapy techniques. An advance in traditional techniques was the introduction of dynamic arcs, which consist of the use of one or several arcs, where each leaf of the MLC is adapted in each projection to maintain a fixed distance, selected by the user, to the volume. The following step is what is known as intensity modulated radiotherapy (IMRT). IMRT consists of one or several static orientations of the beam where photon fluence varies inside each treatment beam. Variations in the fluence are produced by changing the position of the MLC during beam delivery (sliding window) or by the irradiation of multiple conformations of the MLC on a fixed orientation (Step and shoot). Some years later, modulation of the photon fluence in an arc was introduced, with some extra degrees of freedom such as variable dose rate and arc rotation speed, known as Volumetric Modulated Arc Therapy (VMAT). The use of modulated techniques creates dose distributions with steeper dose gradients and a more pronounced concave and irregular conformation than with conformal techniques. Consequently, better preservation of healthy tissue/organs can be achieved with these improvements.

1.2 Basic dosimetry concepts

1.2.1 Absorbed dose definition

In 1950 the International Commission on Radiation Units and Measurements (ICRU) formalized the definition of absorbed dose (D) “in terms of the quantity of the energy per unit mass of irradiated material at the point of interest”. Absorbed dose is defined for all types of ionizing radiation, including charged and uncharged particles, as the mean energy imparted per unit mass, where $d\bar{\varepsilon}$ is the mean energy imparted to the infinitessimal mass dm.

$$D = \frac{d\bar{\varepsilon}}{dm} \tag{1.1}$$

In the International System of Units the unit for absorbed dose is the Gray (Gy) defined as:

$$1\,Gy = 1\,J/1\,kg$$

1.2.2 Relative dose-distribution parameters

Tissue phantom ratio (TPR) is defined as the quotient between the absorbed dose (or absorbed dose rate) in a phantom and the dose at the same point at a fixed reference depth. When the reference depth corresponds to the maximum absorbed dose depth, the ratio is named the Tissue Maximum Ratio (TMR) (equation 1.2).

$$TMR(z, f_{clin}) = \frac{D(z, f_{clin})}{D(z_{max}, f_{clin})} \tag{1.2}$$

Where z and z_{max} represent the depth and the depth at maximum dose and f_{clin} is the clinical field size.

High energy photon beams are normally characterized by their Beam quality Q. Beam quality is defined as the $TPR_{20,10}$ for a field size of 10 cm x 10 cm where the subindexes 20 and 10 signify depths at 20 cm and 10 cm. Q is generally determined in isocentric conditions that correspond to a source-detector distance (SDD) of 100 cm for common linear accelerators used in external radiotherapy.

Field Output Factor (FOF) is defined as the ratio between the absorbed dose to water in reference conditions and at any other field size, at a reference point in a phantom.

Percentage Depth Dose distribution (PDD) (equation 1.3) represents the relative absorbed dose deposited by a radiation beam into a medium as it varies with depth along the axis of the beam. The dose values are normalized at the maximum dose, yielding a plot in terms of percentage of the maximum dose. Dose measurements are generally made in water. For points outside the central axis, the Off Axis Ratio (OAR) (equation 1.4) is defined as the ratio of the dose at a point away from the central axis of the beam to the dose at the central axis point situated at the same depth.

$$PDD(z, f_{clin}, F) = \frac{D(z, f_{clin}, F)}{D(z_{max}, f_{clin}, F)} \times 100 \tag{1.3}$$

$$OAR(r, z, f_{clin}) = \frac{D(0, z, f_{clin})}{D(r, z, f_{clin})} \tag{1.4}$$

Where z and z_{max} represent the depth and the depth at maximum dose, f_{clin} is the clinical field size, r is the distance from the central axis and F is the source-to-surface distance.

1.2.3 Dosemeters

Before introduction of the formalism for absorbed dose determination in reference conditions, an overview of the dosemeters used is included.

The possible effects produced by the interaction of radiation with matter are varied and include changes in temperature, luminescence, chemical properties etc. A dosemeter is considered to be any device capable of providing a reading that is a measure of the dose in its sensitive volume, and with appropiate calibration to provide the desired quantity [3]. These changes need to meet a set of requirements such as repeatability, reproducibility, accuracy and sensitivity. In general, the dosemeter can present dependence on energy, dose rate, pressure, temperature, shape or accumulated dose. These and other characteristics must be determined before their use. Apart from physical detection principles, dosemeters can also be classified as active or passive depending on whether they can yield real time measurements or not.

1.2.3.1 Ionization chamber

The most common type of detector used in clinical practice in the determination of photon absorbed dose is the Ionization Chamber. Ionization chamber is an active detector which collects all the charges created by direct ionization within the gas or liquid through the application of an electric field. It only uses the discrete charges created by each interaction between the incident radiation and the medium. The charges are created by the ionization of air or liquid molecules present in the cavity by the electrons produced by the photoelectric effect, Compton scattering or pair production on the wall chamber or on the medium surrounding it.

All ionization chambers used and studied in this thesis are cylindrical.

Cylindrical chambers are composed of a cavity (sensitive zone) and a stem. The cavity, in general air filled, is defined by three electrodes, the polarization electrode or external electrode, connected directly to the polarization voltage. The collection electrode is connected to an electrometer which has a high impedance and collects the charge or current from the air cavity. Finally, the guard electrode, connected directly to the mass, defines the volume cavity and prevents the collection of leakage currents. The design of an ionization chamber is a compromise between having a cavity volume large enough to collect an appreciable amount of charge and small enough to assign a specific measurement to a point and to prevent important perturbations to the beam fluence.

Figure 1.4 shows a schematic diagram of a generic cylindrical ionization chamber of the Farmer type.

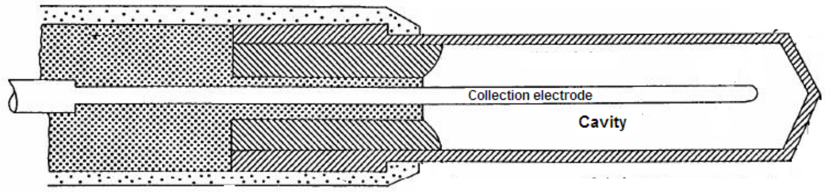

Figure 1.4: Scheme of a cylindrical ionization Farmer chamber

1.2.3.2 Diode

A diode is an active dosemeter based on the effects that ionizing radiation produces on a semiconductor. Excited electrons are transferred from the valence band to the conduction band of the crystal, generating electron-hole pairs. The electrons and holes generated drift in opposite directions due to the intrinsic electric field of the diode, and the charges can be collected. Commercial diodes are made of silicon doped with phosphorus (n-types) or boron (p-types). Their higher density in comparison with water shows a different response depending on the energy spectra which should be taken into account. Diodes have been traditionally used for relative dosimetric purposes, mainly due to their high sensitivity within a small volume which confers good spatial resolution. However, they can present a directional effect and are also influenced by accumulated doses which must be regularly monitored. An additional advantage is the fact they do not need to be connected to a high voltage supply.

1.2.3.3 Radiochromic film

Radiochromic or Gafchromic film is a translucent film that turns blue due to a polymerization process when irradiated by ionizing radiation. These changes are stable for temperatures below 60 °C. They can be scanned without any chemical process. As traditional film dosimetry, a calibration curve is needed since the changes in optical density are not linear with dose. The similar electron density to water make it a promising detector. Extended information about this passive dosemeter can be found in TG-55 from AAPM [4].

1.2.3.4 Thermoluminescent detector (TLD)

Thermoluminescent dosimetry is based on the capacity of some imperfect crystals to re-emit stored energy deposited by ionizing radiation in the form of light when heated. The emitted light is correlated with the absorbed dose. Even though they are not very common in clinical practice, thermoluminescent dosemeters (TLDs) are passive dosemeters that present several advantages such as small size, low fluence perturbation in MV beams and no directional dependence. In addition, some TLDs, such as LiF, have a relatively low effective atomic number and thus a good energy response.

1.2.4 Formalism for absorbed dose determination in reference conditions

In this thesis will be used the formalism and recommendations for absorbed dose determination in reference conditions described in the International Atomic Energy Agency (IAEA) Technical Reports Series (TRS) 398 [5]. A cylindrical ionization chamber is recommended for the determination of absorbed dose to water in high energy photon beams. The absorbed dose to water at the reference depth z_{ref} in water, in a photon beam quality Q_0 and in the absence of the chamber is given by:

$$D_{w,Q_o} = M_{Q_0} \cdot N_{D,w,Q_o}, \tag{1.5}$$

where M_{Q_0} is the chamber reading in the reference conditions used in the standards laboratory and N_{D,w,Q_o} is the calibration factor in terms of absorbed dose to water at a reference quality Qo for the specific ionization chamber (or dosemeter in general) obtained from a standard laboratory when it is centred at z_{ref}.

Quantities of influence such as pressure, temperature, electrometer calibration, polarity effect and ion recombination must be considered by applying necessary factors k_i to appropriately correct the reading M_Q to take into account the differences between final user and reference conditions in the standard laboratory. When the chamber (dosemeter in general) is used on a different beam quality rather than the reference quality Q_o it is necessary to introduce a chamber specific factor, k_{Q,Q_o}, which takes into account the difference between the reference beam quality Q_o (used in the calibration laboratory) and the actual user quality Q. A ^{60}Co photon beam is often used as a reference quality (Q_o), in this case $k_{Q,Q_o}$and N_{D,w,Q_o} are denoted as k_Q and $N_{D,w}$ respectively.

The common expression to obtain the absorbed dose to water in a beam quality Q different from the calibration quality Q_o, is given by equation 1.6, where M_Q has been corrected for the quantities of influence other than the beam quality.

$$D_{w,Q} = M_Q \cdot N_{D,w,Q_o} \cdot k_{Q,Q_o} \tag{1.6}$$

k_{Q,Q_o} can be obtained as:

$$k_{Q,Q_o} = \frac{N_{D,w,Q}}{N_{D,w,Q_o}} = \frac{D_{w,Q}/M_Q}{D_{w,Q_o}/M_{Q_o}} \tag{1.7}$$

Ideally this correction factor should be determined for each ionization chamber and beam quality used. However, in general, not all standard laboratories have beams with the same beam quality as the user [5].

According to Bragg-Gray theory, the absorbed dose in a medium (water in our case) D_w, is related to the mean absorbed dose in the air cavity of the ionization chamber $\overline{D}_{air}$, through a factor identified as the ratio of mass(collision) stopping power ratios water/air $s_{w,air}$.

$$D_w = \overline{D}_{air} \cdot s_{w,air} \tag{1.8}$$

For an ideal detector that does not perturb electron fluence, these factors would be identified as the Spencer-Attix stopping power ratios and could be analytically determined with a set of approximations [6, 7]. As there are no ideal detectors in the real world, a set of correction factors, p_Q, are introduced.

k_{Q,Q_o}values can also be obtained by the user by applying the following relation, derived from Bragg-Gray theory [8].

$$k_{Q,Q_o} = \frac{(s_{w,air})_Q}{(s_{w,air})_{Q_o}} \cdot \frac{(W_{air})_Q}{(W_{air})_{Q_o}} \frac{p_Q}{p_{Q_o}} \tag{1.9}$$

Where:

$(s_{w,air})_Q$ is the Spencer Attix water/material stopping power ratio for the beam quality Q.

$(W_{air})_Q$ is the mean energy expended in air per ion pair formed for the beam quality Q.

p_Q is the overall perturbation correction factor which includes all departures from the ideal Bragg-Gray condition when a ionization chamber is used.

Traditionally, the overall perturbation factor has been divided on the assumption that each separate perturbation factor is small and independent [9]. Several publications have appeared over the last 30 years evaluating the use of the initial analytical expressions for these perturbation factors (cited separately below). Perturbation factors p_Q are generally defined as a product of independent corrections that take into account the different effects (equation 1.10). Several analytical expressions were proposed in the past for these perturbation factors.

$$p_Q = p_{cav} \cdot p_{wall} \cdot p_{dis} \cdot p_{cel} \tag{1.10}$$

The cavity perturbation factor (p_{cav}) corrects the effects that the air cavity produces, mainly the in-scattering, which modifies the electron fluence that would be in the medium in the absence of the cavity. It is considered to be unity for cylindrical ionization chambers at a depth of 5 g/cm^2 in water for photon beams with an uncertainty lower than 0.1% [5].

The wall perturbation factor (p_{wall}) takes into account the differences in radiation response between the chamber wall material and the medium. The initial analytical expression was formulated by Almond and Svensson in 1977 [10] and modified by Gillin et al in 1985 [11] and Hanson and Dominguez-Tinoco in 1985 [12].

The displacement perturbation factor (p_{dis}) depends on the inner radius of the cavity and corrects the effect of replacing the volume of the medium (water) with the detector cavity when the reference point of the chamber is considered to be at the centre of the chamber. An analytical expression was suggested by Johansson et al in 1978 [13].

The central electrode perturbation factor (p_{cel}) corrects the effect created by the presence of a central electrode in the ionization chambers. It was experimentally investigated by Kristensen 1983 [14], Mattsson 1984 [15] and Andreo et al 1992 [8], Nyström and Karlsson 1993 [16], Leither et al 1994 [17], Kosuen et al 1994 [18] and Palm and Mattsson 1999 [9]. It was also studied by Monte Carlo (MC) methods, Nath and Schulz 1981 [19], Smyth and McEwan 1984 [20], Rogers et al 1985 [21] and Ma and Nahum 1993 [22].

It is important to notice that all described factors are energy dependent and p_Q also depends on each particular chamber.

In 2004 J Sempau et al [23], proposed the introduction of $f_{c,Q}$ as a proportionality factor relating the absorbed dose in water with the mean absorbed dose in the detector air cavity.

$$D_w = \bar{D}_{air} \cdot f_{c,Q} \tag{1.11}$$

Consequently, k_{Q,Q_o}can be evaluated as the ratios of the $f_{c,Q}$ for two different qualities. It is important to notice that in spite of the analogy between expressions 1.8 and 1.11, the $f_{c,Q}$ factor is considered to be the proportionality between the doses in the air cavity and in water without any approximation. $f_{c,Q}$ can be obtained using MC simulations for each type of ionization chamber by taking into consideration the real effect of the detector in water or in any other medium.

1.2.5 Small field definition

Although there is no consensus about small field definition, it is accepted that fields smaller than 3 cm x 3 cm present a set of dosimetric properties that must be specifically considered [24]. These properties are the loss of lateral charged particle equilibrium (CPE) and possible partial occlusion of the primary source of radiation. The field size at which these become significant depends on beam energy, focal spot size, and jaw design. Appropriate characterization of the beam and correct modelling of the planning system has a major effect on small fields, and the nature of the detector, geometry and size must be considered for these field sizes [24].

Lateral electron equilibrium (LEE) is compromised when x-ray energy is so high or the beam radius is so small that the latter becomes comparable to the maximum electron range [25]. This has effects on the beam profiles and absorbed dose on the central axis and was one of the reasons why mainly 4 MV or 6 MV beams were originally used for small fields in clinical practice [26]. In 1990 Bjarngard et al [27] showed how the doses on the central axis of 6 MV small photon fields are affected by the incomplete lateral electron equilibrium. They used MC simulations and pointed out that the ratio between absorbed dose and kerma characterizes the degree of electron equilibrium. LEE depends on the energy of the beam and on the density of the medium (electronic density).

Partial occlusion refers to the geometrical issue presented when a finite source collimated below a certain field size will not be completely viewed from points on the central axis at a certain distance from the source. This phenomenon will have an influence on the output factor determined for that field size. At the same time, beam penumbras will also be affected.

1.2.6 Formalism for small-field dosimetry

In 2008 a new formalism [28] was defined as an extension of the existing codes of practice for small-field dosimetry due to the expansion of new treatment units and techniques which lead to situations where codes based on the conversion from ionization to absorbed dose in ionization chambers, were not accurate [29, 30]. The new formalism introduces a new correction factor ($k^{f_{msr},f_{ref}}_{Q_{msr},Q_{ref}}$). The absorbed dose to water, $D^{f_{msr}}_{w,Q_{msr}}$, at the reference depth in water, in a beam quality Q_{msr} and reference machine field f_{msr} and in absence of the chamber is given by

$$D^{f_{msr}}_{w,Q_{msr}} = M^{f_{msr}}_{Q_{msr}} \cdot N_{D,w,Q_o} \cdot k_{Q,Q_o} \cdot k^{f_{msr},f_{ref}}_{Q_{msr},Q_{ref}} \tag{1.12}$$

Where, f_{ref}, f_{msr}, refer to the conventional reference field and the machine specific reference field size. $M^{f_{msr}}_{Q_{msr}}$ are the output readings corrected for quantities of influence (pressure, temperature, polarity and saturation) and $k^{f_{msr},f_{ref}}_{Q_{msr},Q_{ref}}$ is the corresponding correction factor. For machines where the reference field can be established as a conventional machine field ($f_{msr} = f_{ref}$), the absorbed dose to water $D^{f_{clin}}_{w,Q_{clin}}$, at the reference depth in water for a field size f_{clin}, is given by

$$D^{f_{clin}}_{w,Q_{clin}} = M^{f_{clin}}_{Q_{clin}} \cdot N_{D,w,Q_o} \cdot k_{Q,Q_o} \cdot k^{f_{clin},f_{msr}}_{Q_{clin},Q_{msr}} \tag{1.13}$$

In practice, $k^{f_{clin},f_{msr}}_{Q_{clin},Q_{msr}}$ can be obtained by comparing two fields with a primary standard or by using alanine or radiochromic film as a reference detector [28]. Alternatively, it can be calculated by Monte Carlo (MC) simulations.

With the new formalism, the absorbed dose in water at the reference point for a field size f_{clin} in the absence of the chamber is given by:

$$D^{f_{clin}}_{w,Q_{clin}} = D^{f_{msr}}_{w,Q_{msr}} \cdot \Omega^{f_{clin},f_{msr}}_{Q_{clin},Q_{msr}} \tag{1.14}$$

Where $\Omega^{f_{clin},f_{msr}}_{Q_{clin},Q_{msr}}$ represents the FOF (see section 1.2.2). Combining the previous equations (1.12, 1.14) it can be deduced that:

$$\Omega^{f_{clin},f_{msr}}_{Q_{clin},Q_{msr}} = \frac{M^{f_{clin}}_{Q_{clin}}}{M^{f_{msr}}_{Q_{msr}}} \cdot \left[\frac{D^{f_{clin}}_{w,Q_{clin}}/M^{f_{clin}}_{Q_{clin}}}{D^{f_{msr}}_{w,Q_{msr}}/M^{f_{msr}}_{Q_{msr}}}\right] = \frac{M^{f_{clin}}_{Q_{clin}}}{M^{f_{msr}}_{Q_{msr}}} \cdot k^{f_{clin},f_{msr}}_{Q_{clin},Q_{msr}} \tag{1.15}$$

Defining the output ratios ($OR^{f_{clin}}_{f_{ref}}$) as the ratios of the corrected readings (1.16), it can be observed that $k^{f_{clin},f_{msr}}_{Q_{clin},Q_{msr}}$ is a factor which corrects the output ratios of ionisation chambers to field output factors (FOF).

$$OR^{f_{clin}}_{f_{ref}} = M^{f_{clin}}_{Q_{clin}}/M^{f_{msr}}_{Q_{msr}} \tag{1.16}$$

1.2.7 Monte Carlo simulation

The Monte Carlo (MC) method is a statistical method of approximating the solution of complex physical or mathematical systems based on repeated random sampling to obtain numerical results.

In MC simulation of radiation transport, the history (track) of a particle is viewed as a random sequence of free flights that end with an interaction event where the particle changes its direction of movement, loses energy and, occasionally, produces secondary particles [31]. The Monte Carlo simulation of a given experimental arrangement (e.g., an electron beam, coming from an accelerator and impinging on a water phantom) consists of the numerical generation of random histories. To simulate these histories an "interaction model" is needed, i.e., a set of differential cross sections for the relevant interaction mechanisms. The differential cross sections determine the probability distribution functions of the random variables that characterise a track: free path between successive interaction events, the type of interaction taking place and the energy loss and angular deflection for a particular event (and initial state of emitted secondary particles, if any). With these probability functions, random histories can be generated by using appropriate sampling methods. If the number of generated histories is large enough, quantitative information on the transport process may be obtained by simply averaging over the simulated histories, and the Monte Carlo method yields the same information as the solution of the Boltzmann transport equation, with the same interaction model.

1.3 Current challenges in radiotherapy. State of the art

Advances in the detection of cancer combined with new techniques have resulted in a proliferation of new schemes of treatment which reduce the number of treatment fractions. From a clinical point of view, probably the greatest revolution during recent years[1] has been the development of extracranial radiosurgery called SBRT (Stereotactic body radiotherapy) or SABR (stereotactic ablative radiotherapy). Hereinafter this technique will

---

[1] According to the PubMed (www.pubmed.org) database, more than 5000 articles related to SBRT have been published during the last 5 years

be referred to in the text by either term depending on the original source.

In 2010 the American Association of Physicists in Medicine (AAPM) published the Task Group TG-101 [32] devoted to SBRT. In the introduction, the authors state that "in order to achieve high conformation around the volume to irradiate with a rapid fall-off of the dose, [...] the use of non-coplanar beams or arcs and sometimes combined with the use of modulated techniques is a common practice".

The use of non-coplanar beams or arcs can increase the dose conformity and diminish patient entrance doses within the patient, but it also increases the delivery time. Treatment time, including time required for patient set-up and delivery, can range from 15 to 100 minutes [33, 34] depending on the technique, machine and dose per fraction used.

The magnitude and probability of a tumour base line shift from the initial set-up to the end of the treatment increases with extended delivery times [35, 36]. Faster SBRT delivery is therefore not only patient-friendly, but also improves treatment accuracy and allows for more efficient use of departmental resources.

Stereotactic ablative radiotherapy (SABR) is widely regarded as the treatment of choice for early stage lung cancer patients who are medically unfit or decline surgery [37, 38, 39, 40]. In a typical SABR treatment a high biological dose of radiation is delivered in 3 to 8 fractions (#) over a 2- to 3-week time period. Significant improvements in local control have been reported for SABR compared to more conventional radiotherapy (55-66 Gy in 20-33#) delivered over 4 to 7 weeks [41, 42].

Lung treatments have an associated periodic movement of the tumour related to the patient breathing pattern. Several methods have been developed in order to deal with lung breathing. The most well known is *gating*, where the respiratory cycle is controlled and the beam is delivered only in some phases of the breathing cycle. A second method is *tracking*, where the MLC is continuously adapted in order to follow tumour motion. The third option, commonly used, is the definition of a volume that encloses the different positions where the tumour is located during the respiratory cycle and the final planning volume is based on these merged volumes.

The interplay effect is known as the combination of tumour motion and beam motion (as it is shaped by a dynamic MLC) that can cause unexpected hot/cold spots even within the target volume [43]. This has been studied both theoretically and experimentally since the beginning of modulated techniques [44, 45, 46, 47, 48, 49, 50, 51, 52, 53].

In 2006, Berbeco et al [43] concluded, after irradiation of a five-beam lung IMRT plan on a radiochromic film situated on a sinusoidal moving platform, that the standard deviation of the dose to a given pixel in the high dose region could be around 2-3% and that these differences were reduced to 0.3-0.5% after irradiation of 30 fractions.

In 2010 Court et al [50] presented a study based on the irradiation of a house-made phantom containing twenty micro-MOSFET[2]s. Their results showed, that "except in complex IMRT and VMAT plans", the differences in reading for more than 95% of the points within the tumour model were less than 2%. In their conclusions they pointed out that for IMRT the differences can be reduced by lowering the dose rate and for VMAT plans, the deviations are effectively reduced when using two arcs instead of one. In a previous study published the same year [51] the authors related the amplitude of tumour motion with the final deviations as well as associating

---

[2] Metal Oxide Semiconductor Field Effect Transistor. It is a dosemeter with low energy dependence in the MV range, high sensitivity and immediate read out. Not used in this PhD work.

the complexity of the plan with the number of MU.

In addition, in 2012 Rao et al [52] presented a study based on the simulation of the interplay effect and showed a lower dosimetric impact of the intra-fraction motion compared with previous authors. Their conclusions quantified the impact of less than 1% of the prescription dose even for treatments of just three fractions. A few months later, Zhao et al [54], concluded from their analysis on gated lung treatments using a Cyberknife, that the deviation in the dose of PTV and CTV (clinical target volume) is not always negligible in gated SBRT. During the last two years, more studies based on a low number of patients have been presented highlighting the limitation of the interplay effect on the final dose distribution [55, 56, 57]. In 2013 Ong et al [58] found that plans with a unique unflattened arc of 10 MV at 2400 MU/min were susceptible to interplay, but not plans with 2 arcs and more than 2 fractions.

With the new treatment schemes the irradiation time will be extended, also increasing the possibilities of motion during treatment, known as intra-fraction motion. One way to reduce the effect of intra-fraction motion is to reduce irradiation time. This is made possible by removing the flattening filter, as first proposed in several Monte Carlo (MC) studies and prototype designs [59, 60, 61, 62, 63, 64]. In 2010 Varian (Varian Medical Systems, Palo Alto, CA, USA) launched the TrueBeam, a new linear accelerator (LINAC) designed to irradiate using flattened (FF) and flattening filter-free (FFF) beams. Published work on the commissioning of TrueBeam demonstrated the consistency of this LINAC [65, 66, 67]. Varian supported a group of the first European users in which the author of this thesis formed part. So far, two different works from this group have been published. The first was aimed at studing the suitability of the different commercial verification devices for modulated plans using unflattened beams [68] and the second was an inter-comparison between different centres and study of new software based on Monte Carlo simulations [69]. However, all previous cited studies have focused on field sizes larger than 2 cm x 2 cm.

Modulated beams imply the use of small fields or segments. Small fields have been used in radiosurgery at specific centres for the last 30 years. However, the expansion of modulated and hypo-fractionated techniques in most hospitals, has led to the creation of an international working group between the International Atomic Energy Agency (IAEA) with the collaboration of the American Association of Physics in Medicine (AAPM), as cited previously. The aim of this group is to develop standardized recommendations for dosimetry procedures and detectors in reference dosimetry of small and non-standard fields [28].

In parallel with the expansion of the use of small beams, new detectors have appeared. ionization chambers with reduced volumes can be found in most medical physics departments (MPD). The initial recomendations from the manufacturers were their use as relative detectors, but later publications showed that they can also be used as a reference detector and calibration factors, k_{Q,Q_o}, for these models were proposed.

Analytical and MC k_{Q,Q_o} values are derived from the nominal geometry of each ionization chamber model since there is no way of knowing the exact dimensions of each user chamber. In contrast, calibrations in terms of absorbed dose to water in a standard laboratory can be performed under similar conditions to subsequent measurements in the user beam, and consequently, the response of each individual chamber is taken into account in the laboratory. Quality correction factor values have been reported in the literature for several ionization chambers models [70, 71, 72, 73, 74, 75, 76, 77, 78, 79, 80, 81, 82, 83, 84, 85, 86]. However, up until now the differences between k_{Q,Q_o} factors for chambers of the same model, especially for lower volume ionization chambers, have not been definitively discussed. In 2013 Andreo et al [87] studied the discrepancies among the k_Q values published for the NE-2571 model based on MC and experimental determinations in primary laboratories. Recently, a work by Muir [88] analyses experimental fluctuations in $N_{D,w}$ determined by three accredited dosimetry calibration laboratories for several ionization chambers including the PTW-30013 and the NE 2571.

As presented in section 1.2.6, in 2008 [28] a new correction factor $k^{f_{clin},f_{msr}}_{Q_{clin},Q_{msr}}$ was introduced, which corrects the output ratios (OR) of ionization chambers to field output factors (FOF), as shown in equation 1.15. Since the formative work by Alfonso et al [28] other authors have presented either experimental or derived by MC correction factors for a variety of detectors in flattened (FF) and flattening filter-free (FFF) beams [89, 90, 91, 92, 93, 94, 95, 96]. In 2012 Ralston et al [97] proposed splitting the correction factor between geometry/volume effect and the detector material. This allowed quantification and qualification of the correction. However, this adds an additional source of uncertainty.

It is generally understood and all the cited references agree that ionization chambers will need a correction factor, $k^{f_{clin},f_{msr}}_{Q_{clin},Q_{msr}}$, higher than 1 for small field sizes, which is expected due to the volume of any of the actual commercial chambers. On the other hand, diodes can be developed to a much smaller size due to their greater sensitivity. However, the response of these detectors presents a high energy dependence due to their greater density. The relative contribution of secondary radiation to the measurement point is higher for small fields and, as a result, these detectors will have an overestimation for small field sizes and consequently, diodes will require a correction factor lower than 1 [98, 99, 100].

In 2014 Francescon et al [90] analyzed the variation of $k^{f_{clin},f_{msr}}_{Q_{clin},Q_{msr}}$ on percentage depth-dose (PDD) determination for several detectors including small ionization chambers. However, no references analyzing chamber-to-chamber differences of the same type have been presented.

1.4 Aims of the thesis

This PhD thesis is aimed at studing several of the new challenges that medical physics is presently facing. The thesis consist on the analysis of three main topics.

The impact of geometric inaccuracies in a ionization chamber on dosimetric parameters

Ionization chambers have been used as reference detectors in clinical practice for decades. In 2000 a new code of practice [5] was introduced based on the calibration of the ionization chambers in terms of absorbed dose to water instead of the previous code based on air kerma determination [101]. One of the important differences between the previous protocol [101] and the present one [5] is that individual differences between ionization chambers of the same type are taken into account in the new protocol. In the previous one, the user had to calculate factors concerning the particular geometry of their ionization chambers. As it is not possible to know exactly these parameters for a particular chamber, the values for the different dimensions were taken from the chamber specifications without consideration of the particularities of the user ionization chamber.

Not all standard laboratories have linear accelerators with the same user beam qualities. One common practice is that the Primary Standard Dosimetry Laboratory (PSDL) or the Secondary Standard Dosimetry Laboratory (SSDL) performs a calibration of the user ionization chamber in the beam quality of the Co-60 source. Some laboratories also provide calibration factors for the user chamber in other beam qualities whereby correction factors for a particular beam quality are determined by interpolation. When no experimental k_{Q,Q_o} values are provided, the user can calculate them by using a set of expressions derived from Bragg-Gray theory and apply analytical expressions to calculate the overall p_Q perturbation factors. It is also possible to obtain k_{Q,Q_o} values by MC simulation as the ratios of $f_{c,Q}$ factor for two beam qualities as explained previously (section 1.2.4). Analytical and MC values are derived from the nominal geometry of each chamber model since there is no way of knowing the exact dimensions of each user chamber. In contrast, calibrations in terms of absorbed dose to water in a PSDL or SSDL at different beam qualities is the only method where the response of each individual chamber is taken into account.

Within this framework, this thesis has the following aims:

- Determination of the k_{Q,Q_o} values of three thimble ionization chambers and the study of the influence of their manufacturing tolerances (ie, cavity volume, wall thickness...) on k_{Q,Q_o} values.

- Determination of the $k_{Q_{clin},Q_{msr}}^{f_{clin},f_{msr}}$ correction factors for the smallest ionization chamber, PTW-31016, study of the influence of their manufacturing tolerances, and analysis of the influence of the actual field size due to jaw position tolerances.

Small field output factors of the first commercial FFF beams

As mentioned previously, small field characterisation is challenging. In addition, FFF beams have been introduced during the last 5 years. Currently there is no published dosimetric data available on small field sizes (0.5 cm x 0.5 cm to 2 cm x 2 cm) for the TrueBeam LINAC. The most closely related work is by Gete et al [102] in which the authors compare MC simulated 6 MV FFF square field output factors from 1 cm on a TrueBeam. In a similar study, Lechner et al [103] published output factor measurements for an Elekta FFF LINAC. This study aims to determine FOF for four different energies produced by a TrueBeam linear accelerator, two flattened beams and two unflattened and estimate the main sources of uncertainty associated with small field sizes.

Contributions to SABR

The expansion of lung SABR has produced a wide variety in the geometries and techniques used by different institutions. Currently it is possible to find medical departments that use conformed beams, dynamic arcs, IMRT and also VMAT to deliver the prescribed dose. In this chapter a class solution using low modulated coplanar arcs and a method to evaluate the combined effect that modulation and tumour motion (interplay-effect) have on the final dose distribution are proposed. The effect that the use of unflattened beams and the number of breathing cycles have on the final dose distribution is also studied.

As cited previously, several works have been presented since the beginning of modulated techniques on the interplay effect [43, 44, 45, 46, 47, 48, 49, 50, 51, 52, 53, 54]. However, according to the previous references, no consensus exists at present about the final impact of modulated techniques.

In order to contribute to the evaluation of the interplay effect, PUMA (Predicted Upshot Motion Analysis) is proposed as an alternative method to evaluate the interplay-effect. Several modulation indices proposed in the literature are also analyzed to study the suitability of predicting the interplay effect.

Chapter 2

Materials

This chapter presents the main equipment used in the development of the thesis and the MC simulation details used in the different chapters are also described.

2.1 Detectors

The main characteristics of the detectors used in this thesis are summarized in Table 2.1.

2.1.1 Ionization chamber

Three different ionization chambers were used for measurements of the first commercial FFF beams (Chapter 5): two from PTW (PTW–Freiburg) PTW–31010, PTW–31016, and an RK chamber from Scanditronix-Wellhöfer. Following IEC [104] recommendations, each chamber was tested for pre– and post–irradiation leakage, stem leakage, stability and possible dependence of dose rate. The chambers were also cross-calibrated[1] against a reference

---

[1] Not required for relative determinations

Ionization chambers

Model	Cavity Volume (cm^3)	Cavity Radius (mm)	Cavity Length (mm)	Wall material and thickness	Central electrode diameter and Material	Waterproof
RK Scanditronix	0.12	2	10	Encapsulation 1 mm 50% Epoxy resign + 50% graphite	1 mm Al	Yes
PTW-30013	0.6	3.05	23	0.335 mm PMMA + 0.09 mm graphite	1.1 mm Al	Yes
PTW-31010	0.125	2.75	6.5	0.55 mm PMMA + 0.15 mm graphite	1.1 mm Al	Yes
PTW-31016	0.016	1.45	5	0.57 mm PMMA + 0.09 mm graphite	0.3 mm Al	Yes

Diodes

	Type	Radius (mm)	Thickness (mm)	
PFD-Scanditronix	p	1.25	0.45	Silicon. Tungsten powder mixed with epoxy added behind the chip. Shielded
EFD-Scanditronix	p	1.25	0.45	Silicon. Unshielded
Edge SunNuclear	n	square 0.8mm length	0.03	Silicon Epoxy. Housing wall thickness 0.13 mm brass 2.3 mm aperture in front of the active layer (depletion region) 2.1 mm-thick copper substrate

Thermoluminescent detectors

	Dimensions	Thickness (mm)	
TLD-700	square 3.1 mm length	0.9	^{7}LiF:Mg;Ti chips
TLD-700R	Radius 0.5 mm	6	

Radiochromic Film

EBT2 EBT3	0.28 mm thickness. Calibration using a 48-bit colour (Red channel). Resolution of 72 dots per inch (dpi).

Table 2.1: Summary of detectors used in the different studies

chamber NE–2571[2], in a 6 MV photon beam using the International Atomic Energy Agency (IAEA) protocol TRS-398 [5]. For the three models a voltage of 300 V was applied and the OR determinations were performed with a PTW–UNIDOS electrometer. RK model was positioned with the stem parallel to the beam axis, while the PTW-31010 and PTW-31016 were placed perpendicular to the beam axis in all cases.

Details about PTW-30013 are also included since the impact of the manufacturing process on k_{Q,Q_o} for this model is also analyzed in Chapter 4.

2.1.2 Diode

Shielded and unshielded type p-silicon diodes from Scanditronix of 2.5 mm diameter and 0.45 mm thickness were used. Accumulated dose, background signal and fading effects were verified prior to their use as proposed in the literature [99]. A Sun Nuclear Corporation Edge Detector diode, with an active detection area of 0.8 mm x 0.8 mm and a 0.13 mm thick brass housing, was also used. In all cases readings for OR determinations were performed with a PTW–UNIDOS electrometer.

2.1.3 Radiochromic film

Gafchromic EBT2 (International Specialty Products, Wayne, NJ, USA) radiochromic film was used for FOF measurements (Chapter 5). Film calibration was performed on a 30 cm x 30 cm slab of Solid Water (Radiation Measurements Inc.) at 6 MV up to 3 Gy. Scanning was performed on an Epson 10000XL (Seiko Epson Corporation) scanner in which the inhomogeneous response was corrected. Film orientation was also considered. The films were analysed using a 48-bit colour depth and a resolution of 72 dots

---

[2] This chamber has a $N_{D,w}$ factor defined by the NPL Laboratory in the range of $TPR_{20,10}$[0.568-0.755].

per inch (dpi). The pixel value in the red channel of the image was used for calibration [4].

Gafchromic EBT3 was used for SABR verifications on the Quasar phantom (Chapter 6). The calibration range was extended up to 9 Gy and the scanning was done on a Vidar scanner. The analysis was performed with the same resolution as mentioned for the Epson 10000XL. Film Analysis and comparisons with planned doses as well as dynamic and static irradiations were carried out using RIT 113 software (Radiological Imaging Technology, USA).

2.1.4 TLD

The TLDs used were ^{7}LiF:Mg;Ti chips: TLD–700R of 1 mm diameter and 6 mm length and also a square TLD–700 from Thermo Scientific of side 3.1 mm and thickness of 0.9 mm. ^{7}LiF detectors were chosen to avoid possible neutron contributions. Before each irradiation standard annealing was carried out in a PTW–TLD oven: 1 h at 400°C followed by 2 h at 100°C. The detectors were read using a Thermo Scientific Harshaw M5500 hot gas reader. The heating cycle consisted of two stages, a preheating phase at 135°C for 10 s and a reading phase of 10 s from a temperature range of 135°C to 270°C at a linear rate of 25°C s^{-1}. To improve dosemeter accuracy, individual calibration factors were established for each detector and stability checks performed periodically with a caesium–137 beam. Each experiment was repeated a minimum of three times in two different sessions. The calibration and behaviour of these detectors have been described extensively elsewhere [105]. The calibration and reading process was performed at Institut de Tècniques Energètiques (INTE). For all measurements the TLD–700R was placed vertically.

2.2 Electron linear accelerators

Determinations in Chapter 5 were performed on two TrueBeam LINACs from two different institutions, Institut Català d'Oncologia (ICO) and Edinburgh Cancer Centre (ECC).

TrueBeam can deliver 6 and 10 MV FF and FFF photon beams. In FF mode, dose rates up to 600 monitor units per minute (MU/min) in 100 MU/min increments are possible. In 6 MV FFF mode, dose rates from 400 to 1400 MU/min in increments of 200 MU/min are possible and in 10 MV FFF mode, from 400 to 2400 MU/min in increments of 400 MU/min.

Plans for lung SABR treatment with FF beams (Chapter 6) were performed on a Silhouette (Varian) LINAC with 6 MV with a maximum dose rate (600 MU/min).

2.3 Treatment planning system

The Eclipse V.10.1 treatment planning system from Varian was used for optimization and calculation of SABR treatment plans (Chapter 6). Plans were optimized with the algorithm Dose Volume Optimizer (DVO) V 10.0.28 and dose distributions were calculated with the Anisotropic Analytical Algorithm (AAA V.10.0.28).

2.4 Phantoms

Several phantoms were used depending on the type of measurement. PDDs and OAR from TrueBeam were determined with ionization chambers and diodes on a PTW MP3-M water phantom (Chapter 5). These measurements were repeated on a SunNuclear 3D Scanner.

FOF determinations with ionization chambers and diodes from TrueBeam (Chapter 5) were determined in a water phantom and in a solid phantom in the case of Radiochromic films and TLDs. In order to estimate the influence of the phantom material, FOF with ionization chambers were determined in both phantoms.

Quasar phantom

It has been considered useful to present a schematic diagram of the Quasar phantom (Modus Medical Devices) used in Chapter 6, to facilitate understanding of the device.

It is a solid phantom with a cylindrical hole where several inserts can be placed. In our case, a wooden insert, where a radiochromic film can be placed inside, was used.

The insert is attached to a motor that can move it within the phantom with an amplitude and frequency selected by the user. Figure 2.1 shows a schematic diagram.

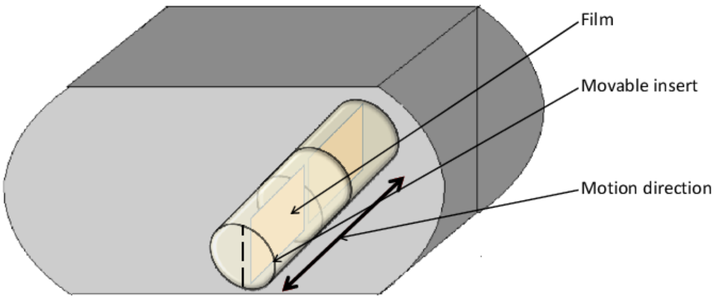

Figure 2.1: Quasar phantom scheme

2.5 Monte Carlo Simulation details

MC simulations in Chapters 4 and 5 were performed with the PENELOPE code system [31]. PENELOPE is coded in Fortran90 and is free and open source that simulates the coupled transport of photons, electrons and positrons in the energy range from a few eV to 1 GeV, and in arbitrary materials. The simulation of photon transport follows the usual analogue procedure, i.e. all the interaction events in a photon history are simulated in chronological succession until the photon reaches an energy lower than a user-defined threshold (the absorption energy, Eabs). The simulation of electron and positron tracks is performed by means of a mixed algorithm. Individual “hard" elastic collisions (deflections larger than a given cut-off angle), “hard" inelastic interactions (energy loss larger than a given cut-off, WCC) and “hard" bremsstrahlung emission (energy loss larger than a given cut-off, WCR) are simulated by random sampling from the corresponding restricted differential cross sections. Energy straggling for inelastic and bremsstrahlung interactions is accounted for in a consistent manner. Thus, electron step size is selectable by means of user-defined parameters: WCC, WCR are mentioned above; C1 is the average angular deflection; C2 is the maximum average energy loss; and DSMAX is the maximum allowed step length. Analogue collision-by-collision electron/positron simulation can be performed by setting C1 = C2 = WCC = WCR = 0. The simulation is fairly stable under variations of the cut-offs and these can be made quite large, thus speeding up the calculation considerably, without altering the results. The track of a particle between successive hard interactions or between a hard interaction and the crossing of an interface (i.e. a surface that separates two media with different compositions) is generated as a series of steps of limited length. The combined effect of all (usually many) soft interactions that occur along a step is simulated as a single “artificial" soft event (a random hinge) where the particle loses energy and changes its direction of motion. The energy loss and angular deflection at the hinge are generated according to a multiple scattering approach that yields energy loss distributions and angular distributions with the correct mean and variance (first and second moments). Secondary particles emitted with initial energy larger than the absorption energy (Monte Carlo transport cut-off) are stored, and simulated after completion of each primary track. Secondary particles are produced in direct interactions (hard inelastic collisions, hard bremsstrahlung emission, positron annihilation, Compton scattering, photoelectric absorption and pair production) and as fluorescent radiation (characteristic x-rays and Auger electrons). PENELOPE users can adapt a steering main program in order to define the radiation source, the simulation parameters, the quantities of interest to be scored, variance reduction (VR) techniques to be applied and report the final results. The modular general-purpose main program for PENELOPE named penEasy [106] has been employed (Version 2009) in this thesis.

To get a reasonably low statistical uncertainty in the dose calculations, the PSF must contain a relatively large number of particles. The generated PSFs used in this work stored up to 2×10^6 particles per cm^2 to ensure that the statistical uncertainty would be below 0.1% for the dose computation. In all cases the uncertainty is expressed as 1 standard deviation (sd).

2.5.1 Particle space files used in k_{Q,Q_o}determination

The energies used in section 3.1.1 were Co, 6 MV, 15 MV and 18 MV. Phase space files (PSF) for Co [107], 6 MV [108] were downloaded from IAEA[3]. In the case of 15 MV [109] and 18 MV [110], PSFs created at the Institut de

---

[3] www-nds.iaea.org/phsp/phsp.htmlx

Tècniques Energètiques (INTE) were used. In both cases, a Varian Clinac 2100 C/D accelerator head was modelled according to the manufacturer's specifications. The initial electron energy, energy spread, and radial intensity of the beams were tuned so that the calculated PDD and dose profile fitted the measured PDD curves and lateral profiles in water.

2.5.2 TrueBeam Particle space files

The PSF recorded just above the movable jaws, and files containing information on the geometry and movement of the jaws, were provided by Varian (Varian Medical System) for the four energies 6 and 10 MV FF and FFF beams. Initial simulations of four square fields were performed (0.5, 1, 2 and 10 cm side length).

To reduce computation time the simulations were carried out in two stages. Firstly, particles were tracked through the treatment head and stored in a PSF at 70 cm. Secondly, dose distributions in the phantom were calculated using these new PSF as the particle source.

2.5.3 Determinations in water

Cylindrical voxels of 0.5 mm radius and 2 mm length were defined for all determinations of absorbed dose in water.

2.5.4 Dose to ionization chamber air cavity determination

The photon energy cut-off was set to 1 keV for all materials throughout the entire geometry, whereas those for charged particles were made zone-dependent as described below. The threshold energies for charged particle radiative and inelastic collisions were set equal to the cut-off energies. The parameters C1 and C2, modulating the limit between detailed and condensed

Measurement type	Shape	X (mm)	Y (mm)	Z (mm)
OAR 1 cm x 1 cm	Cuboids	2	0.5	0.5
OAR 10 cm x 10 cm	Cuboids	10	0.5	0.5
detector accuracy	3 x 3 Matrix of cuboids	1	1	2
		r (mm)		
Field Output Factor	Cylindrical	0.5		2
PDD	Cylindrical	1		0.5

Table 2.2: Shape and size of the voxels used in the TrueBeam MC simulations

charged particle transport simulation, were set to 0.1 for surrounding water and stem (more than one cm away from the air cavity) and detailed simulation of charged particles(C1=C2=0) was performed on the material walls, air cavity and central electrode. The geometry to be simulated for each detector was split into two regions, the first was a spherical volume with a radius of 2 cm around the detector (hereafter called the region of interest, ROI) and the second region was the rest of the geometry. Within the ROI, a cut-off energy of 10 keV was selected for the charged particles, outside the ROI, a cut-off energy of 200 keV was applied in order to satisfy a radiation (bremsstrahlung) yield below the intended uncertainty of the calculations, 0.15% (Type A) in the scored absorbed dose.

2.5.5 Monte Carlo Simulation voxel details on TrueBeam determinations

As will be described in section 3.2.1, PDDs and OAR for 1 and 10 cm side length were simulated by MC and compared with measurements performed with different detectors. Table 2.2 shows the voxel shape and size defined at the four energies for FOF, OAR and PDD determination.

Chapter 3

Methodology

This chapter describes the procedures undertaken with the equipment described in chapter 2 to develop the three main topics studied in this thesis and whose results are presented in chapters 4 to 6.

3.1 The impact of geometric inaccuracies on dosimetric parameters in an ionization chamber

Ionization chambers are the most common detector used in medical physics departments to determine all the dosimetric parameters necessary to characterize beams. As previously presented in the introduction, the absorbed dose determination in reference conditions with ionization chambers requires knowledge of several factors such as $N_{D,w,Qo}$, k_{Q,Q_o}, which can be determined in PSDL or SSDL. In addition, the new correction factor $k_{Q_{clin},Q_{msr}}^{f_{clin},f_{msr}}$ proposed by Alfonso et al [28] must also be considered in small-field dosimetry.

This section describes the methodology used to estimate the differences that can exist between the correction factors k_{Q,Q_o} and $k_{Q_{clin},Q_{msr}}^{f_{clin},f_{msr}}$ due to geometrical manufacturing differences in chambers of the same type . Analysis of k_{Q,Q_o} is performed for three waterproof models of different volume and the study of $k^{f_{clin},f_{msr}}_{Q_{clin},Q_{msr}}$ is centred on the ionization chamber with the smallest cavity volume analysed (0.016 cm^3). Both studies are based on the geometrical tolerances that each model has.

3.1.1 k_{Q,Q_o} determination

Three waterproof ionization chambers models from PTW were selected, PTW-30013, PTW-31010 and PTW-31016. The main characteristics can be found in Table 2.1. Detailed information on the geometry and tolerance dimensions were obtained from the manufacturers. For each of the three PTW models, three different geometries were defined and labelled nominal, maximum and minimum. The nominal geometry was defined using the nominal dimensions and maximum and minimum geometries refer to the maximum and minimum air cavity volume, respectively. They were defined by modifying the wall diameters and length of the walls and central electrode, i.e., the maximum geometry was defined with the maximum cavity walls and the minimum dimensions for the central electrode and the minimum geometry with the minimum cavity walls and the maximum central electrode. The differences between internal and external wall thickness were applied by maintaining a fixed thickness of graphite and applying the variations to the PMMA for all the geometries defined. Figure 3.1 is a schematic diagram of the geometries defined (nominal, maximum and mínimum) from the information provided by the manufacturer.

k_{Q,Q_o} values were obtained by MC simulation following the approach proposed by J Sempau et al [23], where the $f_{c,Q}$ factor was defined as a proportionality factor relating the absorbed dose in water with the mean absorbed dose in the detector air cavity (equation 1.11).

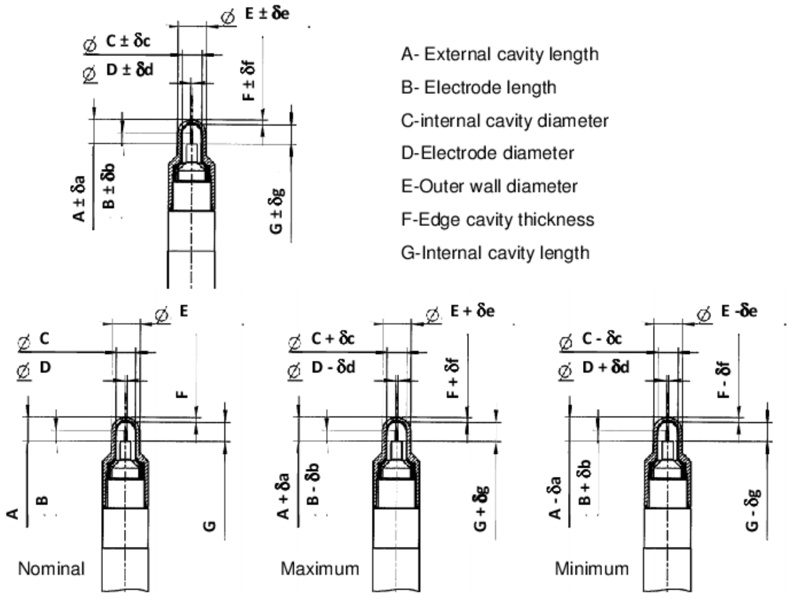

Figure 3.1: Diagram of the three considered geometries defined from the tolerances in the dimensions provided by the manufacturer. (Dimensions and tolerance values are not shown because of confidentiality agreements with the manufacturer)

Consequently, k_{Q,Q_o}, can be evaluated as the ratio of $f_{c,Q}$ for two different beam qualities:

$$k_{Q,Q_o} = \frac{f_{c,Q}}{f_{c,Q_o}} \tag{3.1}$$

A fourth non-waterproof model from Nuclear Enterprise (NE–2571) was used to validate the consistency of the methodology applied. This model was selected to test the MC simulation process due to the great amount of data available in the literature and also because of its small geometrical tolerance in comparison with the other three ionization chambers studied.

3.1.2 Geometrical influence on $k^{f_{clin},f_{msr}}_{Q_{clin},Q_{msr}}$ determination for PTW-31016

The effect that geometrical tolerances from the manufacturing process have on $k^{f_{clin},f_{msr}}_{Q_{clin},Q_{msr}}$ are examined in the smallest chamber (PTW-31016). According to Alfonso et al [28], $k^{f_{clin},f_{msr}}_{Q_{clin},Q_{msr}}$ correction factors are not expected to exhibit an energy dependence in the case of ionization chambers, and this point will be discussed in Chapter 5. The study was performed with a 10 MV FFF beam, which has the most inhomogeneous dose distribution for current beams delivered by LINACs. Thus, this energy was chosen in order to obtain an upper limit for this effect.

The correction factor, for each field size, was obtained as the ratio between the FOF obtained in a water phantom and the ratio of the mean absorbed dose in the air cavity for each field size, while the reference field size was fixed at 10 cm x 10 cm. Equation 3.2

$$k^{f_{clin},f_{msr}}_{Q_{clin},Q_{msr}} = k^{f_{clin},f_{10x10}}_{Q_{clin},Q_{10x10}} = \frac{D^{f_{clin}}_{w,MC}/D^{10x10}_{w,MC}}{\bar{D}^{f_{clin}}_{air,MC}/\bar{D}^{10x10}_{air,MC}} \tag{3.2}$$

Where $D^{f_{clin}}_{w,MC}$ represents the absorbed dose in water for a field size f simulated by MC and $\bar{D}^{f_{clin}}_{air,MC}$ is the mean absorbed dose in the ionization chamber air cavity. The subindex MC was added to clarify that in all cases values are obtained by MC simulation.

Backscatter on the jaws and ionization chambers needs to be considered when FOF are determined by MC simulation. Some authors have estimated it to be 1.5% in small fields [111]. On the other hand, some authors have found good agreement between MC determinations and experimental measurements without taking it into consideration [102]. The method proposed here to determine correction factors removes the influence of backscatter on the monitor chamber since the effect would equally affect both of the terms of the ratio in equation 3.2.

3.1.3 Set-up accuracy in $k^{f_{clin},f_{msr}}_{Q_{clin},Q_{msr}}$ determination

The set-up position of the chamber during measurements is especially critical when using small fields. The option that has been used in all experimental determinations with active dosemeters has been to position the detector at the site that maximizes the reading. It is understood that the same approach is necessary in MC simulations, to set-up the ionization chamber at the position that maximizes the reading in the ionization chamber.

According to the values provided by the manufacturer, PTW-31016 has a nominal diameter equal to the cavity length. However, the tolerance of the cavity length is much higher than for the diameter. As a consequence, the three geometries defined for this model differ mainly in the cavity length as shown in Figure 3.2.

Although this section aims to determine $k^{f_{clin},f_{msr}}_{Q_{clin},Q_{msr}}$ theoretically by MC, where the geometry can be defined “exactly”, it is important to take into account the fact that Varian assigns a 0.5 mm tolerance to the LINAC jaw position and consequently the field size tolerance must also be considered before using these values for experimental determinations. In order to study the effect that these tolerances have on the $k^{f_{clin},f_{msr}}_{Q_{clin},Q_{msr}}$ correction factor, $k^{f_{clin},f_{msr}}_{Q_{clin},Q_{msr}}$ was also determined for a field size of 0.45 cm side length. Assuming that the effect increases when field sizes diminish, only the 0.45 cm size was considered.

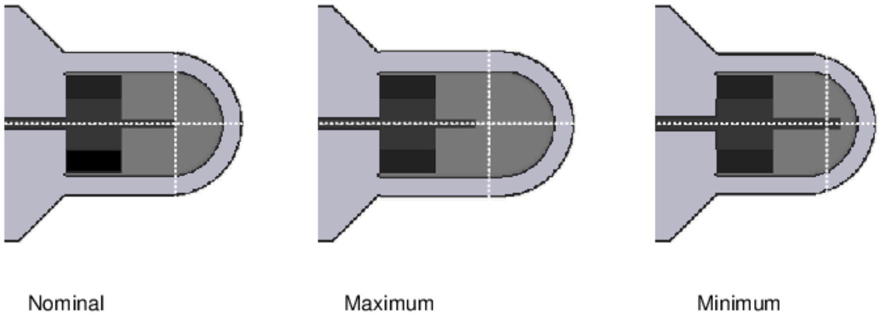

Figure 3.2: Schematic diagram of the three geometries defined for PTW-31016. With detail of the origin coordinates assigned for each geometry

3.2 Small field output factors for first commercial flattened filter free beams

A set of preliminary studies were performed with several detectors and also the PSFs (see section 2.8) from TrueBeam were verified. The experimental FOF determination for field sizes up to 2 cm side length were compared with values from MC simulations.

The main sources of uncertainties (jaw and detector set-up) in small field output factor determination were also studied.

3.2.1 Preliminary verifications

To validate the results above 2.5 cm square length, where there is published data available [67, 65, 66], FOF and tissue phantom ratio at 20 and 10 cm depth ($TPR_{20,10}$) were compared for the four energies studied. Percentage depth dose (PDDs) and off axis ratios (OAR) for 1 and 10 cm side length were simulated by MC and compared with measurements performed on a PTW MP3-M water phantom with four detectors: two ionization chambers (PTW–31016 and RK) and two semiconductor detectors (Edge and PFD).

Gamma analysis [112] at 2%, 2 mm was used to compare MC with the response of the different detectors. OAR for all energies were measured at a SDD of 100 cm at 5 cm and 10 cm depth and normalised to the maximum. The results were compared with MC on square fields of 1 and 10 cm length.

3.2.2 Output ratios determination

Output ratios (OR) were determined in isocentric conditions at 5 cm depth for 6 MV and 6 MV FFF and at 10 cm for higher energies. They were measured for square fields ranging from 0.5 cm x 0.5 cm to 10 cm x 10 cm for the four energies. OR were determined using nine detectors: three ionization chambers: PTW-31010, PTW 31016 and RK; three diodes: Edge, PFD and EFD; radiochromic film EBT2 and two TLDs: TLD–700 and TLD–700R (TLD-700R was only used for the small fields). For active detectors the readings recorded on the detector at sub-millimetre displacements of the TrueBeam treatment couch were used to establish the location of maximum output, otherwise known as the set-up isocentre. To estimate the uncertainty in OR values due to detector position, three measurements were taken at the centre of the field and at four points +/- 1 mm along the X and Y axes for each field size. The charge reading in the centre was used for calculation of the FOF and the relative uncertainty was estimated as the standard deviation of the five different measurement positions. The uncertainty of the radiochromic film was estimated from the standard deviation of the mean pixel value at a radius of 1 mm around the set-up isocentre. Five measurements were taken using the TLDs and repeated on two different days.

3.2.3 Field Output Factor determination for square fields larger than 2 cm side length

The correction factor, $k^{f_{clin},f_{msr}}_{Q_{clin},Q_{msr}}$, was set to unity for square fields equal to, or greater than, 2.5 cm side length and consequently FOF were equal to OR.

In this text f_{ref}, f_{msr} are equal to 10 cm x 10 cm square field size and consequently, from equation 1.16

$$OR^{f_{clin}}_{f_{ref}} = OR^{f_{clin}}_{f_{10cmx10cm}} = \frac{M^{f_{clin}}_{Q_{clin}}}{M^{f_{msr}}_{Q_{msr}}} = \frac{M^{f_{clin}}_{Q_{clin}}}{M^{10cmx10cm}_{Q_{10cmx10cm}}} \qquad (3.3)$$

3.2.4 Field Output Factor determination for square field sizes up to 2 cm side length

As previously metioned, the dosimetric characterisation of small fields is challenging due to the active volume and non-water equivalence of any detector combined with the lack of lateral charged particle equilibrium [24]. In addition, the effect of small changes on the field size due to machine calibration also needs to be considered.

Our strategy to overcome these difficulties was to calculate the field output factors by MC simulation using the nominal field sizes and to determine experimentally all the output ratios for the detectors with a smaller volume. PTW-31016 was chosen because it was the smallest ionization chamber available and the low energy dependence on the $k^{f_{clin},f_{msr}}_{Q_{clin},Q_{msr}}$ correction factors expected for this type of detector [28]. The $k^{f_{clin},f_{msr}}_{Q_{clin},Q_{msr}}$ presented in Figure 4.3 for the nominal model were applied on the OR at the four energies and the results compared with the values obtained with the other detectors. Ion recombination factor differences were considered as part of the final uncertainty, which were expected to be less than 0.5% [113, 114]. TLD-700R and radiochromic film correction factors were considered to be equal to 1 for all field sizes and energies.

3.2.5 Geometric set-up inaccuracies

The main source of set-up inaccuracies was analyzed separately by examining the detector set-up and inaccuracies in the jaw set-up.

Detector set-up

The influence of the PTW-31016 set-up was studied during the determination of $k_{Q_{clin},Q_{msr}}^{f_{clin},f_{msr}}$ by MC simulation as described in section 3.1.3. A more general detector set-up analysis was performed for the FFF energies using a 1 mm x 1 mm x 2 mm voxel matrix defined around the geometrical centre of the beam at reference depth.

Jaw set-up

In order to consider the 0.5 mm tolerance on the jaw position (section 3.1.3), two square fields of 0.45 cm and 0.49 cm side length were defined at all energies to study their influence on FOF determination by MC simulation.

Validation

To corroborate the influence of jaw inaccuracies predicted by MC, OR were determined with both the Edge detector and the TLD-700R on a second TrueBeam at another institution. These detectors were selected to record the output readings because of their greater spatial resolution. It is understood that different LINACS, especially from different institutions, will have submillimetric differences in field size. The original values were measured at the ICO and the second LINAC chosen was at ECC.

3.3 Contributions to SABR treatments

Previous paragraphs present the studies to improve the determination and analysis of dosimetric parameters related with the determination of absorbed dose in reference conditions and also in small fields. This paragraph describes the methodology proposed to improve planning of lung SABR. The main characteristics of SABR have already been introduced in section 1.3.

The studies presented were performed during the implementation of the lung SABR technique in ECC. Some important decisions were taken prior to the introduction of SABR in ECC, such as reducing treatment time as much as possible and developing a standard solution (class solution) valid for most patients. As explained in the introduction, the reduction of the total treatment time implies the use of coplanar beams or arcs, otherwise, a significant part of the time will be spent rotating the couch. Continuous irradiation without the application of gating or tracking was also fixed in advance.

In order to find a solution valid for a high percentage of patients, a certain level of modulation is required. The interplay effect must be considered when modulated plans are delivered, particularly when it is clearly known that the PTV for a lung will have intra-fraction movements due to the breathing cycle.

Present CT scanners allow the generation of a collection of several CT images covering the breathing cycle which are used to fix the motion and deformation of the tumour and also to know the breathing parameters for each patient. Internal Target Volume (ITV) definition can be performed using a special reconstruction that some CTs perform (the maximum intensity projection), merging the GTVs (gross tumour volume) structures defined on different phases of the respiratory cycle or a mix of the former options. Finally, the PTV is defined by adding an appropriate margin to the ITV.

A schematic diagram of a target volume is presented in Figure 3.3 together with the influence of periodic volume motion during irradiation in the final dose distribution. The continuous line in Figure 3.3 corresponds to the planned dose distribution. However, because of the periodic motion of the volume, the final dose distribution will be represented by the dotted line. Dose distribution in zone A is related to the motion amplitude and is almost independent of the modulation of the plan, it would be affected by the total number of cycles during irradiation and would become independent of it for a high number of breathing periods as will be discussed later. Zone B is the zone that would include the GTV. Volume motion during irradiation should not affect the final dose distribution in zone B for a flattened conformed beam, and would produce a smoothing of the peak for the unflattened conformed beams compared with the static situation. Final dose distribution in zone B can potentially be greatly influenced by the motion of the volume for a modulated plan (IMRT/VMAT) since not all points in this zone are continuously and homogeneously irradiated. Thus, this zone is where the suitability of modulated plans must be studied. Gating techniques should be used in case effects in zone A wish to be reduced, such techniques will also affect the final dose distribution in zone B.

The proposed configuration to irradiate lung SABR treatments with low modulated arcs is first introduced, followed by the basis of PUMA, the method to evaluate the suitability of modulated lung SABR plans due to the interplay effect. Finally, there is a study of the published modulation indices to evaluate the interplay effect.

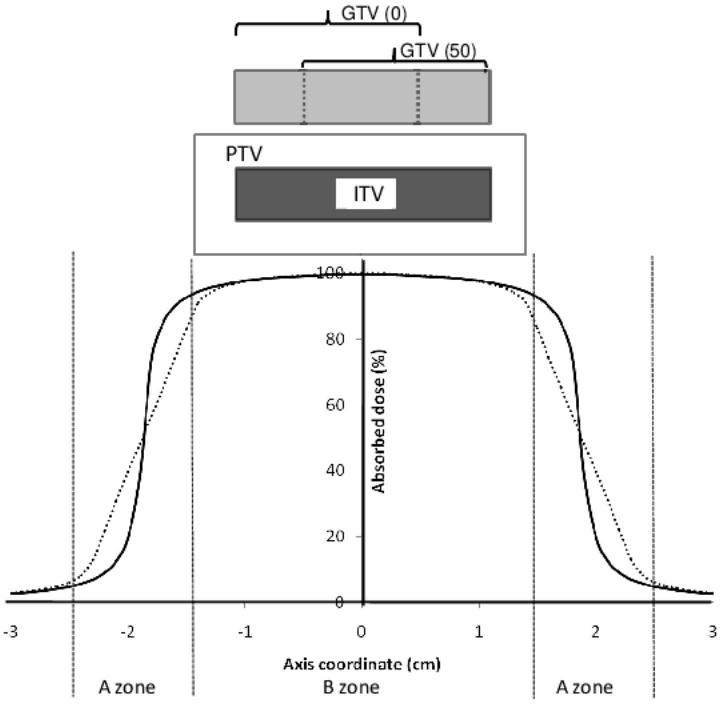

Figure 3.3: Diagram of target volume definition and the effects of periodic volume motion during irradiation on the final dose distribution. Internal Target Volume (ITV) is defined by encompassing the Gross Tumour Volume (GTV) in the different breathing phases. Planning target volume (PTV) is defined by applying an appropriate margin to the ITV. Solid line represents a profile of the planned beam on the projection of PTV and the dotted line represents the final dose distribution on that plane as a consequence of a periodic target motion on the left-right direction

3.3.1 The effect of low modulated plans

Plan set-up proposed is based on four coplanar 6 MV arcs of 200°–220° centred at the centre of the tumour, two clockwise and two counterclockwise with two different collimator rotations, starting or finishing on the back of the patient (180°). To study the effect of the modulation on the interplay effect, a new plan with a lower modulation was created for 6 patients. Low modulation reduces the effect of tumour motion on the final dose distribution, allowing the maximum dose in the GTV to be kept below 125% of the prescribed dose (SABR protocols admit a maximum of 140% of prescription dose within the ITV) [115] . This is achieved in the Eclipse TPS by forcing a reduction in monitor units (MU) during optimization. This configuration implies that gantry speed for low modulated plans is close to the maximum, and represents between 8.5 and 10 breathing cycles during each arc irradiation. The advantages of including a minimum of 8 breathing cycles will be presented later.

4DCT data sets were used to create VMAT plans from Eclipse (V.10.1). The modulation indices of the 12 initial plans were scored using ALPO (Average Leaf Pair Opening). Verification plans were calculated on the Respiratory Quasar phantom (Modus Medical Devices) and irradiated on a LINAC Silhouette. Radiochromic films (EBT3) placed in the phantom were irradiated and analyzed. Each plan was delivered twice on the phantom, the first one with no movement and the second one using fixed parameters (1 cm peak to peak, 12 breaths per minute–BPM). Because of the dose saturation that the red channel of radiochromic film has to high doses, the delivered dose was 1/3 of the prescribed dose per fraction on the 18 Gy/# plans and 1/2 for the 11 Gy/#.

A relative comparison of dose distributions between the measurements and TPS was performed. The criteria for evaluation were set to be $< 5\%$ of points with $\gamma(3\%, 3mm) > 1$ [112] on the comparison between static and dynamic dose distributions recorded on radiochromic films inserted in the Quasar phantom. This method was fixed as the standard method to analyze the interplay effect for all SABR patients. A threshold of 90% of the maximum was fixed since the aim of the analysis was to study the influence of the modulation on the ITV (Zone B on Figure 3.3). As the maximum dose on the plan is approximately 115-120% of the prescribed dose, the chosen threshold approximately represents the prescription dose.

After the acquisition of a TrueBeam at ECC, a new class solution was proposed with just two arcs for the 10 MV FFF, considering the higher dose rate for this energy (2400 UM/min) which implies a similar time per arc, but a reduction in the total treatment time.

3.3.2 Number of breathing cycles included in each arc

A consequence of the irradiation during breathing is an enlargement of the penumbra (zone A on Figure 3.3). To study the influence of the fraction of a cycle included in the total number of breaths during an arc delivery, a convolution of the static beam profile using a sinusoidal function, which represents a simplification of tumour motion was calculated for the most unfavourable situation (n complete cycles plus half). The difference between one complete cycle (or n) and n and a half, was scored, and the minimum number of breathing cycles (n) included on an arc to have the maximum differences in the dose lower than 2% were found for the 3 more common energies used in SABR treatments, i.e. 6 MV from a conventional linear accelerator and 6 MV and 10 MV unflattened beams from a Varian TrueBeam.

3.3.3 Basis of PUMA method

The method used to evaluate the interplay effect on lung SABR patients with the Quasar phantom is time consuming and also requires a minimum of one hour of treatment machine time to set-up the phantom and perform the two irradiations in static and dynamic mode, as explained previously. In addition, the radiochromic film scan is recommended to be performed a minimum of 6 hours after the irradiation. Because of these limitations an alternative method named as PUMA–Predicted Upshot Motion Analysis was developed.

The method is based on the translation of the periodic breathing cycle of the PTV to the beam. It consists of two main steps: first, each arc of the initial plan is split into sub-arcs of 3°. Subsequently, the plan is exported and in-house software developed using Matlab (Mathworks) creates two new plans, the first one applies a sine function to the cranio-caudal coordinate of the isocentre of each sub-arc and a second plan applies a cosine function (Figure 3.4). The absorbed dose distributions of these two new plans (sine and cosine) are calculated and compared with the initial planned distribution.

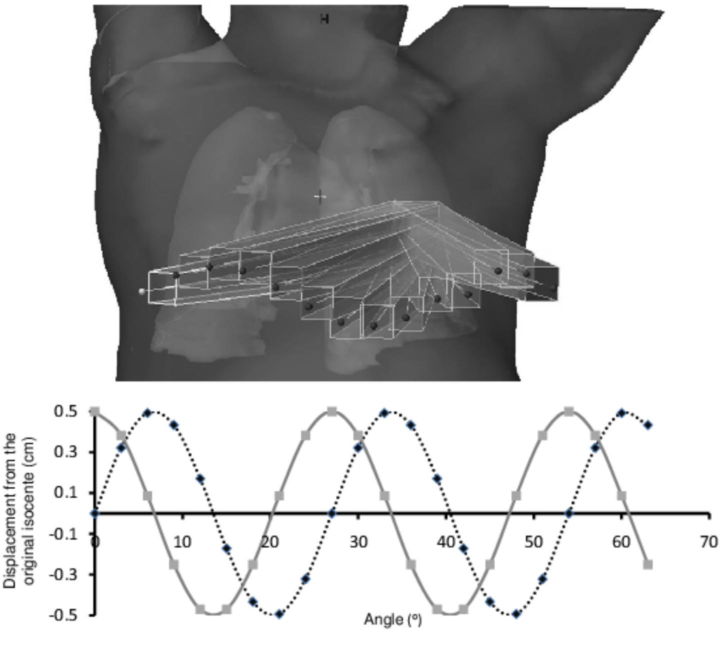

Figure 3.4: Diagram of the split of the arcs and periodic change in the cranio-caudal direction. Period equal to 27° of the original arc that corresponds to 9 sub-arcs

It is important to notice that in routine clinical practice, the irradiation starts without first checking the phase of the breathing cycle, and consequently this approach allows the analysis of the interplay effect in two opposite situations.

The frequency of the sine and cosine functions is calculated from the gantry speed of the arcs (4.5°/s) and 12 BPM is assumed (see Figure 3.4). This implies the equivalence that a breathing cycle corresponds to 27°. These two new plans are imported again to the treatment planning system and dose distributions are compared with the split arcs planned with a unique isocentre.

Using the TPS tools a subtraction of the original dose distributions with the sine or cosines plan is performed and the percentage of the ITV volume with dose differences higher than 3% of the prescription dose on the ITV is scored. In all cases the most unfavourable case is recorded.

Acceptance criteria

The criteria for evaluation are set to be less than 5% of points with more than 3% dose difference between plans created by PUMA and the split plans with the original isocentre inside the ITV.

Evaluation

To test the viability of the PUMA method to evaluate the interplay effect on lung SABR modulated treatments, 23 plans were evaluated with PUMA and compared with the results obtained with the method proposed as standard (radiochromic films in Quasar). The 23 plans evaluated are the 12 plans presented in section 6.1.1, six more low modulated plans and five plans created with 10 MV FFF and two arcs.

Several indices have been proposed in the literature in order to estimate the complexity of a modulated plan which could also imply a higher interplay effect. The selected indices to be analyzed were firstly the Modulation

Complexity Score (MCS) introduced by McNiven in 2010 [116] as one of the first indices proposed; secondly the Modulation Index Total (MIt) proposed in 2014 by Park [117] which introduces speed and MLC acceleration and finally the Aperture Irregularity (AI), Aperture irregularity was introduced by Du in 2014 [118] which analyzes the non-circularity of the MLC apertures. These indices were calculated with Matlab software developed by V. Hernandez and J. Saez.

Possible linear correlation between the mentioned indices and radiochromic films was analyzed [119] and a statistical analysis of their sensitivity and specificity was performed.

Chapter 4

The impact of geometric inaccuracies on dosimetric parameters. Results and discussion

The results presented have been obtained following the methodology detailed in section 3.1. MC simulation details can be found in section 2.5.

4.1 Previous verifications

k_{Q,Q_o} factors were determined for NE–2571 by MC simulation. Results are presented in Figure 4.1 and compared with previously published results. According to the present comparison, the good agreement between the results of these simulations and those reported by others implies that the phase space files, the simulation parameters and the methodology used were appropriate.

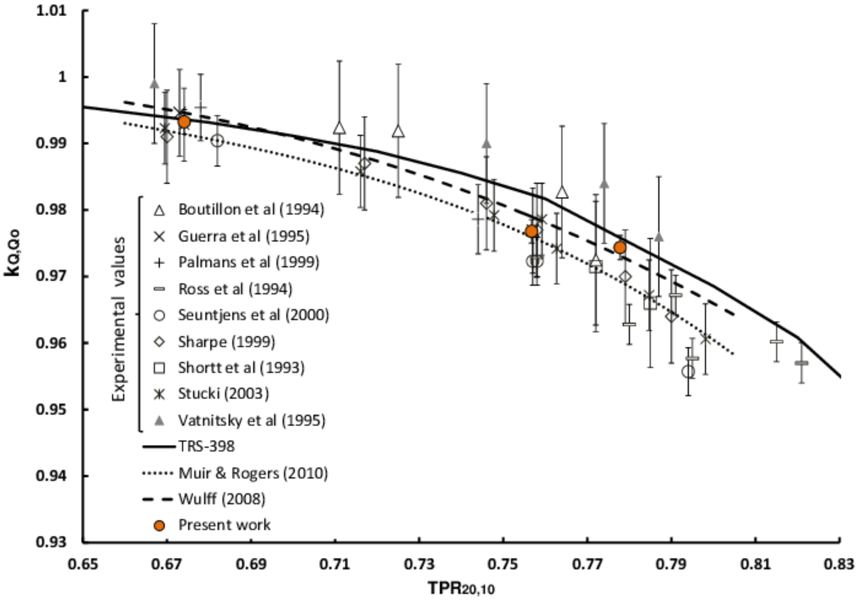

Figure 4.1: k_{Q,Q_o} determined for NE-2571 compared with previously published values. Lines indicate a polynomial function proposed by the authors based on analytical expressions (TRS-398) or MC simulation

4.2 Geometric influence on reference conditions

The relative difference in cavity volume between the nominal, maximum or minimum geometry increases, as expected, for smaller ionization chambers. However, the larger tolerance of both the radius and length of the central electrode for PTW-31010 in comparison with PTW-31016 causes a major difference in the cavity volume for the maximum geometry for this model. Due to the confidentiality agreement with the manufacturer, Table 4.1 only shows the percentage volume difference from the nominal on the central electrode and internal cavity without considering the central electrode for the geometries defined for the three PTW models.

$f_{c,Q}$ factors for the different energies and geometries studied are presented in Table 4.2. Differences in $f_{c,Q}$ within the same model are less than

Model	Geometry	Central electrode	Internal cavity*	Cavity volume
PTW-30013	Nominal	22.02 mm^3	637.10 mm^3	615.1 mm^3
	Maximum	- 3.4%	+ 3.3%	+ 3.6%
	Minimum	+ 3.5%	- 3.9%	- 4%
PTW31010	Nominal	4.42 mm^3	134.33 mm^3	126.55 mm^3
	Maximum	- 16%	+ 36%	+ 40%
	Minimum	+ 21%	- 11%	- 15%
PTW-31016	Nominal	0.11 mm^3	15. 96 mm^3	15.85 mm^3
	Maximum	-34%	+ 22%	+ 23 %
	Minimum	+ 42%	- 22%	- 22%

**Cavity defined by the walls; Cavity volume = Internal cavity - Central electrode*

Table 4.1: Nominal volumes and percentage volume difference, from nominal geometry, for central electrode, internal cavity without central electrode consideration and cavity volume for the geometries defined

0.4% ± 0.2%. The maximum difference is found for PTW-31016 and is much lower than the relative differences in cavity volume which are approximately 23%.

Model	Geometry	Nominal energy ($TPR_{20,10}$)			
		Co	6 MV (0.674)	15 MV (0.757)	18 MV (0.778)
PTW-30013	Nominal	1.111	1.100	1.089	1.081
	Maximum	1.113	1.102	1.087	1.080
	Minimum	1.110	1.101	1.086	1.079
PTW-31010	Nominal	1.122	1.110	1.088	1.089
	Maximum	1.126	1.111	1.088	1.092
	Minimum	1.119	1.107	1.087	1.087
PTW-31016	Nominal	1.134	1.119	1.100	1.092
	Maximum	1.136	1.119	1.101	1.092
	Minimum	1.136	1.116	1.097	1.089
NE-2571	Nominal	1.109	1.101	1.083	1.080

Uncertainties in all values are smaller than 0.15% (1 sd)

Table 4.2: $f_{c,Q}$ factors determined by simulation at the different energies for the different geometries defined in each ionization chamber

The results shown in Table 4.2 imply that the impact of geometric inaccuracies in the manufacturing process mainly affect the calibration factor $N_{D,w,Qo}$ of each chamber while their impact on the k_{Q,Q_o} factors is much smaller, as can be seen in Table 4.3.

Model	Geometry	Nominal energy ($TPR_{20,10}$)		
		6 MV (0.674)	15 MV (0.757)	18 MV (0.778)
PTW-30013	Nominal	0.991	0.981	0.973
	Maximum	0.990	0.977	0.970
	Minimum	0.992	0.978	0.972
PTW-31010	Nominal	0.990	0.970	0.970
	Maximum	0.987	0.967	0.970
	Minimum	0.989	0.971	0.972
PTW-31016	Nominal	0.987	0.970	0.963
	Maximum	0.985	0.969	0.961
	Minimum	0.983	0.966	0.959
NE-2571	Nominal	0.993	0.977	0.974

Uncertainties in all values are smaller than 0.2% (1 sd)

Table 4.3: k_{Q,Q_o}factors determined by simulation at the different energies for the different geometries defined in each ionization chamber

From the results presented in Table 4.3 it can be concluded that the differences in k_{Q,Q_o} due to the manufacturing process of any of the three PTW models studied is less than 0.5% (±0.2% - 1 sd).

A comparison of the k_{Q,Q_o} factors presented in Table 4.3 with values published in the literature was carried out, the results are presented in Figure 4.2. Only experimental data from primary laboratories and MC simulation results are considered.

As shown in Figures 4.1 and 4.2, the differences among different publications are larger than the influence of geometrical tolerance found in the present study (Figure 4.2). The dispersion between published values could

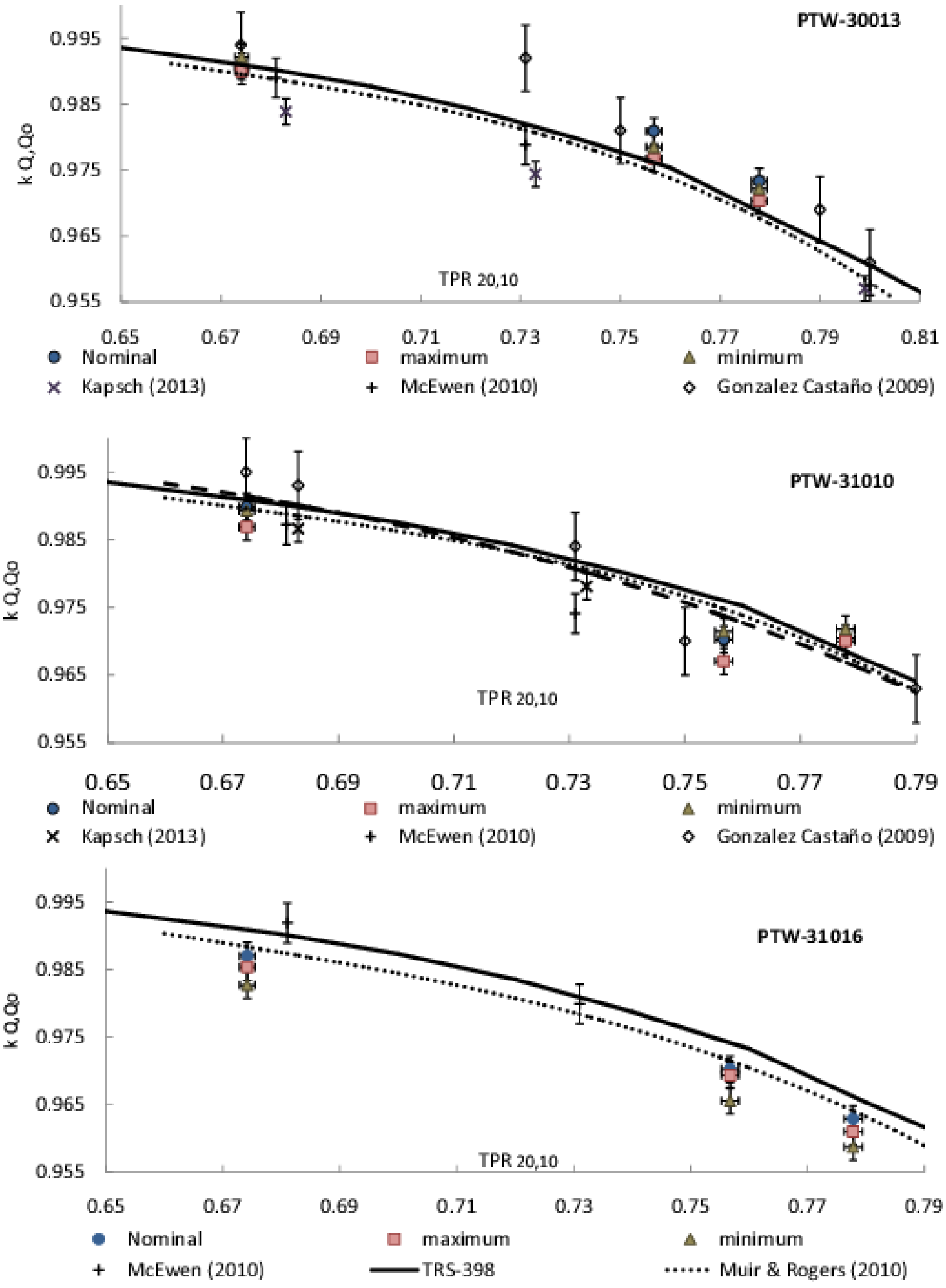

Figure 4.2: k_{Q,Q_o} factors determined by the three geometries defined for each model compared with previously published values. Lines indicate a polynomial function proposed by the authors based on analytical expressions (TRS–398) or MC simulation. Kapsch and McEwen corresponds to experimental values from PSDL

be related to small differences or simplifications during definition of the geometry and simulation parameters, and also due to differences in material composition between chambers of the same model for the experimental published values. Our results indicate that differences in the active collecting volume for the three PTW ionization chambers affects the $N_{D,w,Qo}$ coefficients to the same proportion (see equation 1.6), and that their influence on the k_{Q,Q_o} is less than 0.5%. The dispersion in the $N_{D,w,Qo}$ obtained in our work is in agreement with what was recently published by Muir [88]. In his study he also analysed differences in the manufacturing process and variations due to stability over time for four models including PTW-30013 and NE-2571. From his data, it is not possible to know the variability of volumes in the experimental ionization chambers analyzed. However, the maximum differences in $N_{D,w,Qo}$ from the average is approximately 4% for PTW-30013. This result agrees with the percentage difference in volume between maximum/minimum and nominal geometries defined in our study for this model.

Differences in $s_{w,air}$, W_{air} between two clinical MV photon beam qualities are assumed to be negligible and consequently the differences in k_{Q,Q_o} in chambers of the same type are reduced to ratios of perturbation factors (equation 1.9). The influence of the different perturbation factors (detailed in equation 1.10) on k_{Q,Q_o} was analyzed as the ratio of perturbation factors for two beam qualities.

According to literature previously cited, p_{cav} has been ruled out as a possible cause of chamber-to-chamber differences since it is considered to be equal to 1 independently of photon beam energy with an uncertainty lower than 0.1%.

Variations in the central electrode thickness, for the three models selected, are small in comparison with differences studied in previous publications [22]. Thus, according to the proposed values [22, 9] p_{cel} cannot explain the differences found between chambers of the same type.

p_{dis} has an explicit dependence on both the energy and internal cavity radius [13]. However, differences calculated in $p_{dis,Q}/p_{dis,Qo}$ ratios for the geometries of the same model would imply a much lower effect (differences found were below 0.01%).

As previously explained, variations in wall thickness were applied by fixing the graphite thickness and changing the PMMA thickness. The differences found in $p_{wall,Q}/p_{wall,Qo}$ range from 0.02% for 6 MV to up to 0.31% for 15 MV. These values are of the same order as the k_{Q,Q_o} variations found in our study. Therefore, considering the uncertainties of our results, we could assume that the wall perturbation factor, p_{wall}, is mainly responsible for the k_{Q,Q_o} differences between chambers of the same model. However, p_{wall} ratios calculated for the different energies do not explain why the calculated k_{Q,Q_o} values do not follow the expected sequence: $k_{Q,Q_o(max)} < k_{Q,Q_o(nom)} < k_{Q,Q_o(min)}$. Nevertheless, $f_{c,Q}$ factors presented in Table 4.2 show the espected behaviour, i.e., $f_{c,Q}$ values are larger when the cavity volume increases. All in all, it is worth pointing out that the observed differences between $k_{Q,Q_o}$for the same model are of the same order as their associated uncertainties.

Calibration factor differences between chambers of the same type can be caused by small differences in geometry and also differences in materials and the manufacturing process over the years. In recent years, several compilations of experimental k_Q factors have been published in the literature [82, 85, 120, 121] as well as other studies based on MC simulations [83, 122], which allow for a comparison with experimental data. In all cases uncertainties of k_{Q,Q_o} factors were estimated up to a maximum of 0.5%. Apart from the geometric tolerance studied here, differences between published results in the literature could also be affected by geometry definition, materials and transport radiation parameters in MC simulation and also by small differences in material composition for experimental studies.

4.3 Geometrical influence on $k_{Q_{clin},Q_{msr}}^{f_{clin},f_{msr}}$ determination for PTW-31016

The influence of geometrical tolerances on the manufacturing process was studied, as in the previous section, by the definition of the three geometries for the PTW-31016 model, the smallest ionization chamber studied.

$k_{Q_{clin},Q_{msr}}^{f_{clin},f_{msr}}$ were determined, as explained in section 3.1.2, at 10 MV FFF following equation 3.2. In this section the correction factor differences caused by the small differences in the geometry will be discussed. The $k_{Q_{clin},Q_{msr}}^{f_{clin},f_{msr}}$ values obtained for the nominal geometry will be applied and discussed in Chapter 5.

Prior to the $k_{Q_{clin},Q_{msr}}^{f_{clin},f_{msr}}$ determination for the smallest field sizes by MC, the position that maximizes the mean absorbed dose in the ionization chamber cavity was determined by applying sub-millimetre variations in the longitudinal set-up coordinate of the ionization chamber. The point that maximizes the reading was found at 0.3 mm in the stem direction from the origin defined in the ionization chamber manual for the nominal geometry (Figure 3.2). However, the maximum response was not found in the same position for the three geometries. Differences in position were due to how the geometries were defined. Table 4.4 shows the correction factors determined, following equation 3.2, for the three geometries for the 0.45 and 0.5 cm side lengths. One set of data is for where the geometries were centred according to the

Geometry	Field Size			
	0.5 cm x 0.5 cm		0.45 cm x 0.45 cm	
	Origin	0.3 mm	Origin	0.3 mm
Nominal	1.186	1.176	1.212	1.198
Maximum	1.204	1.211	1.234	1.234
Minimum	1.176	1.157	1.200	1.178

Uncertainties in all values are smaller than 0.2% (1 sd)

Table 4.4: $k^{f_{clin},f_{msr}}_{Q_{clin},Q_{msr}}$ determined for the three geometries by fixing the origin according to the manual and with the origin displaced 0.3 mm along the longitudinal axis where the maximum reading from the ionization chamber was found for the nominal geometry

Geometry	Field size (cm)				
	10	2	1	0.5	0.45
Nominal	1	0.835	0.640	0.324	0.280
Maximum	0.999	0.834	0.635	0.315	0.271
Minimum	1.001	0.835	0.642	0.330	0.284

Uncertainties in all values are smaller than 0.15% (1 sd)

Table 4.5: Mean absorbed dose in the air cavity for the three geometries defined for PTW-31016 at 10 MV FFF. Values normalized to the 10 cm square field for the nominal geometry

manual, while the other set is for 0.3 mm in the longitudinal direction of the stem.

Results presented in Table 4.4 show that inaccuracies in the jaw set-up from the LINAC have a greater influence on the correction factor than the 0.3 mm set-up. Differences in the correction factor due to geometrical inaccuracies during the manufacturing process should also be pointed out.

The deposited energy in the air cavity normalized to the 10 cm square field for the nominal geometry is presented in Table 4.5. In order to study the effect of volume differences on the mean absorbed dose, differences between nominal, maximum and minimum from the average for each field size were calculated. These values are presented in Table 4.6.

Geometry	Field size (cm)				
	10	2	1	0.5	0.45
Nominal	0.0 %	0.0 %	0.1 %	0.4 %	0.4 %
Maximum	-0.1 %	-0.1 %	-0.6 %	-2.6 %	-2.6 %
Minimum	0.1 %	0.1 %	0.5 %	2.1 %	2.3 %

Table 4.6: Differences between deposited energy in the air cavity between nominal, maximum and minimum from the average for each field size

In Figure 4.3 $k_{Q_{clin},Q_{msr}}^{f_{clin},f_{msr}}$ factors determined for the three geometries for square fields up to 2 cm side length are presented. In order to be in line with experimental procedures, the position that maximizes the reading was considered, in other words, the position that minimizes the correction factor.

In Tables 4.5 and 4.6 no differences, within uncertainties, can be observed in the mean absorbed dose in the air cavity of the ionization chamber for field sizes equal to or above 2 cm for the three defined geometries. These results agree with what was observed in the previous section for different energies in reference conditions. For field sizes larger than 2 cm, the effect on the mean absorbed dose in the air cavity due to the geometry of a particular PTW-31016 is negligible. The correction factor for a 2-cm field in isocentric conditions at 10 cm depth is 1.006 independently of the geometries defined (Figure 4.3).

Below 2 cm, the mean absorbed dose in the air cavity varies for the three geometries, indicating that the geometry of each user chamber will affect its correction factor. The largest cavity (maximum geometry) collects a lower mean dose and consequently will need a higher correction factor. On the other hand, the mean dose in the minimum geometry is higher and therefore the correction factor is smaller than the nominal geometry.

The results indicate that the main reason for having correction factors

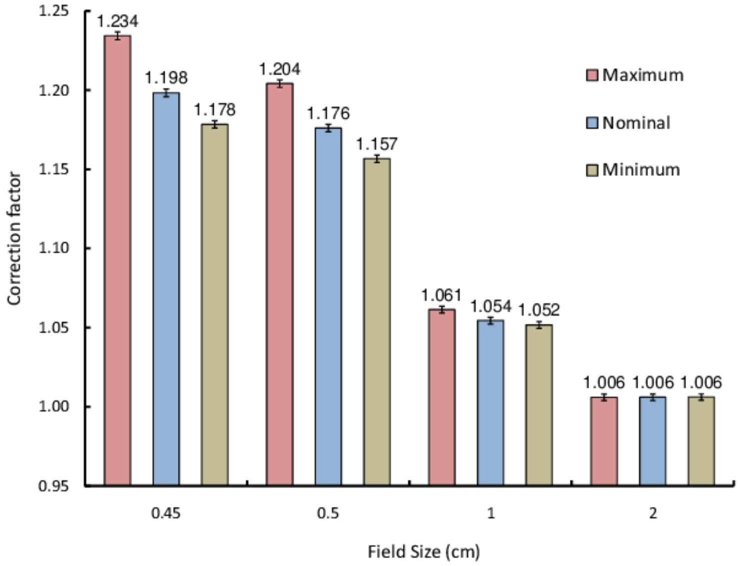

Figure 4.3: MC simulation of $k^{f_{clin},f_{msr}}_{Q_{clin},Q_{msr}}$ for the three geometries defined for PTW-31016 model for square fields up to 2 cm side length determined at 10 MV FFF

larger than 1 in ionization chambers is the volume effect, which represents a limitation that affects square field sizes up to 2 cm. In addition, in square field sizes up to 1 cm the correction factor for the PTW-31016 will also be affected by the particular user chamber, since geometrical variations during the manufacturing process affect the correction factor.

As observed in Figure 4.3, the correction factor increases from 1.8% (minimum geometry - smallest cavity) to 2.5% (maximum geometry - largest cavity) when the field size is diminished 0.5 mm. As discussed previously, the maximum geometry will be greater affected by differences in the field size.

To summarize, the $k^{f_{clin},f_{msr}}_{Q_{clin},Q_{msr}}$ correction factors with appropriate uncertainties proposed for PTW-31016 considering detector set-up, differences between ionization chambers of the same model and tolerances in the field size definition are presented in Table 4.7. Correction factor uncertainty for the 0.5 field size was estimated by considering the uncertainties separately

	Nominal field size (cm)					
	0.5		1		2	
$k^{f_{clin},f_{msr}}_{Q_{clin},Q_{msr}}$	1.17	±2.8%	1.054	±0.6%	1.006	±0.2%

Table 4.7: $k^{f_{clin},f_{msr}}_{Q_{clin},Q_{msr}}$ correction factors for PTW-31016. Assigned uncertainty considering detector set-up, chamber-to-chamber differences and field size tolerance (coverage factor, k=1)

for the three effects (Values obtained from Table 4.4). Combined uncertainties were obtained by geometric addition of uncertainties (1.5% corresponds to the geometrical tolerances of the chamber, 0.8% to the set-up position and 2.2 % to the LINAC jaw set-up).

4.4 Conclusions

The effect that geometrical tolerances during the manufacturing process have on coefficients and factors related to absorbed dose determination in reference conditions have been analyzed.

Differences in the air cavity volume between PTW-31016 chambers of the same model can reach 23%. These differences, in reference conditions, will mainly affect the $N_{D,w,Qo}$. The differences in chamber-to-chamber k_{Q,Q_o} due to differences in the manufacturing process for the three models analyzed were estimated to be below 0.5%. The variation in wall thickness was suggested as the main cause of these differences.

The influence that the particular geometry of an ionization chamber has on the $k^{f_{clin},f_{msr}}_{Q_{clin},Q_{msr}}$ factors was determined for the smallest chamber analyzed, PTW-31016 (0.016 cm^3). According to the results presented, a 2.8% uncertainty should be assigned to the $k^{f_{clin},f_{msr}}_{Q_{clin},Q_{msr}}$ factor for the 0.5 cm square field. This uncertainty would be reduced to 0.6% for a 1 cm square field size. Finally, it is shown that differences in $k_{Q_{clin},Q_{msr}}^{f_{clin},f_{msr}}$ between PTW-31016 chambers for a 2 cm square field are negligible.

Chapter 5

Small field output factors for TrueBeam FFF beams. Results and discussion

The results presented have been obtained following the methodology detailed in section 3.2. MC simulation details can be found in section 2.5.

5.1 Preliminary verification. Percentage depth-dose and off-axis ratios

Figure 5.1 shows PDDs obtained for 1 and 10 cm square fields irradiated with 6 MV FFF and 10 MV FFF beams using four detectors. MC simulation results are included in the graph and are used as reference data for comparison. The behaviour of the different detectors and MC is evaluated by calculating the gamma function (2 %, 2 mm) and is shown on the right Y-axis of the graph. Good agreement is found among RK, PTW-31016, Edge detector and MC simulation for both energies. The particular response of the Scanditronix shielded diode (PFD) did not agree well with the other detectors and MC, which has also been previously reported by other researchers [98].

The values of $TPR_{20,10}$ were found to have differences lower than 1.2% for the four energies and agree with previously published data obtained from averaging results from several LINACs [67, 66].

The OARs for square fields of side length 1 and 10 cm were compared with MC simulations for 6 MV FFF and 10 MV FFF. The volumetric effect of the detectors can be observed on the shoulders (inflexion point of the penumbra) in Figure 5.1. It can be observed that PTW-31016 has better spatial resolution than RK, due to a smaller diameter. However, the small volume of the diodes conform a steeper gradient around the inflexion points, as expected.

PDDs and OARs results show good agreement between experimental and MC simulation. Therefore, it can be concluded that both the the PSFs provided by Varian and jaws configurations defined are correct.

5.2 Output ratio determination

Tables 5.1, 5.2, 5.3 and 5.4 show the OR determined using the nine detectors for field sizes ranging from 0.5 cm to 10 cm. OR were determined in isocentric conditions (SDD = 100 cm) in all cases.

5.3 Field Output Factor determination for square fields larger than 2 cm side length

Percentage differences between the FOF determined by each detector and the average measured by the ionization chambers for square fields larger than 2 cm side length are presented in Figure 5.3. For square fields with a side

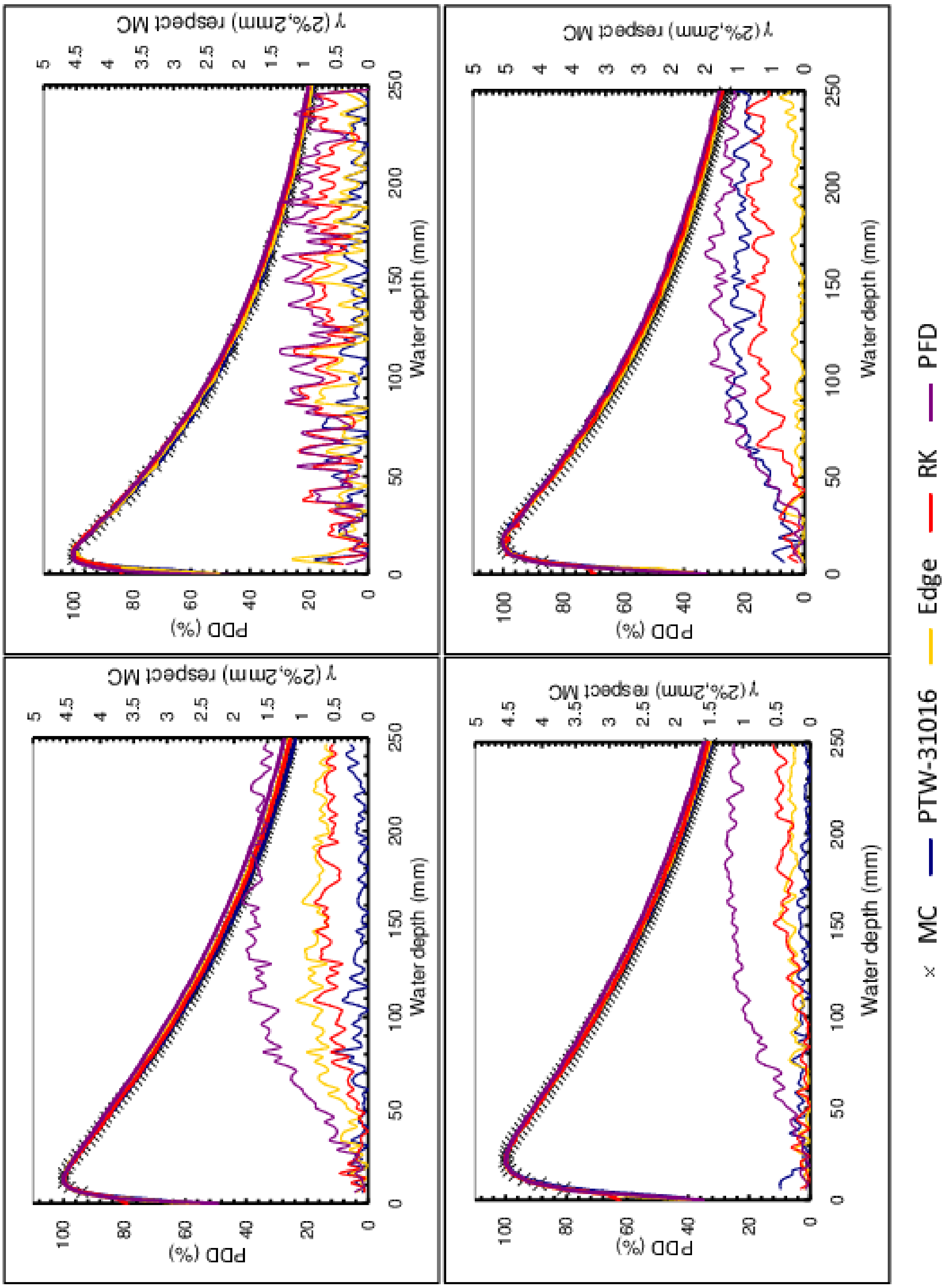

Figure 5.1: Experimental and MC simulated depth-dose curves for 6 MV FFF (top) and 10 MV FFF (bottom) for field sizes of 10 cm and 1 cm. Gamma (2%, 2 mm) for all detectors is also shown with MC as a reference on the right Y-axis

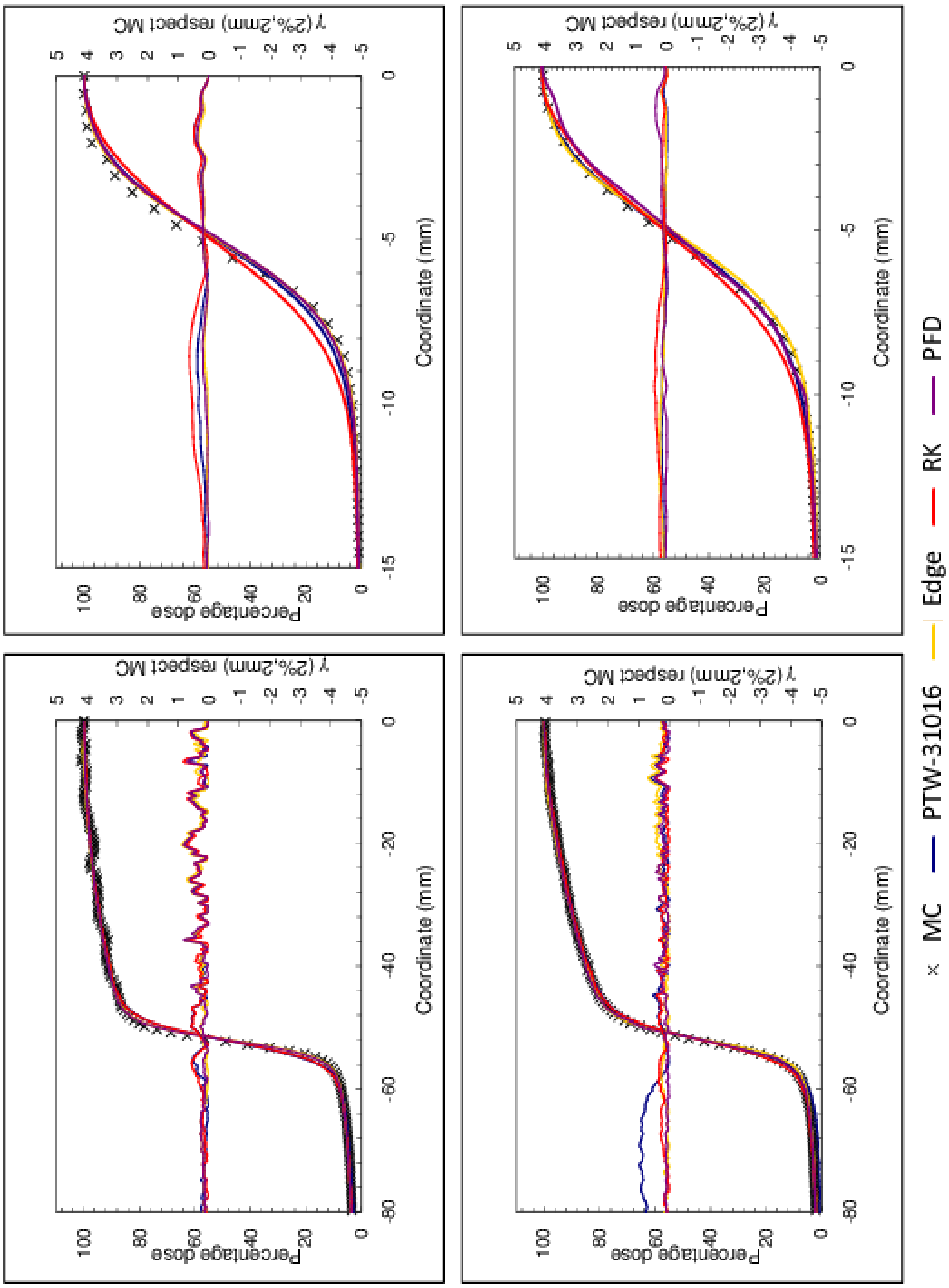

Figure 5.2: Experimental and MC simulated off-axis ratios for 6 MV FFF (top) and 10 MV FFF (bottom) for field sizes of 10 cm and 1 cm. Gamma (2%, 2 mm) for all detectors is also shown with MC as a reference on the right Y-axis

Field size (cm)	Radiochromic film		RK		PTW-31010		PTW-31016		PFD		EFD		Edge		TLD-700		TLD-700R	
	OR	u(%)	OR	u(%)	OR	u(%)	OR	u(%)	OR	u(%)	OR	u(%)	OR	u(%)	OR	u(%)	OR	u(%)
10	1		1		1		1		1		1		1		1		1	
9	0.990	1	0.989	0.05	0.990	0.05	0.990	0.55	0.988	1.2	0.995	0.4	0.989	0.4				
8	0.975	1	0.977	0.03	0.979	0.06	0.979	0.03	0.981	1.2	0.971	0.4	0976	0.4				
7	0.971	1	0.962	0.04	0.966	0.06	0.965	0.04	0.969	1.3	0.953	0.4	0.963	0.4	0.965	0.4		
6	0.956	1	0.946	0.04	0.950	0.07	0.950	0.04	0.949	1.3	0.949	0.4	0.944	0.4				
5	0.949	1	0.926	0.05	0.931	0.08	0.931	0.05	0.934	1.3	0.918	0.4	0.924	0.4	0.920	0.8		
4.5	0.930	1	0.915	0.05	0.921	0.07	0.921	0.05	0.926	1.3	0.901	0.4	0.914	0.4	0.919	0.4		
4	0.923	1	0.904	0.04	0.910	0.07	0.909	0.04	0.911	1.3	0.904	0.4	0.903	0.4	0.903	0.4		
3.5	0.917	1	0.892	0.04	0.897	0.06	0.898	0.04	0.903	1.3	0.884	0.4	0.891	0.4	0.894	0.5		
3	0.906	1	0.878	0.08	0.884	0.06	0.883	0.08	0.893	1.3	0.865	0.4	0.878	0.4	0.868	0.4		
2.5	0.882	1	0.863	0.05	0.868	0.07	0.867	0.05	0.875	1.3	0.865	0.4	0.865	0.3	0.872	0.8		
2	0.856	1	0.841	0.04	0.841	0.2	0.847	0.1	0.861	1.3	0.844	0.3	0.848	0.1	0.830	0.8	0.825	1.0
1.5	0.829	1	0.798	0.1	0.788	0.3	0.807	0.3	0.835	1.4	0.807	0.5	0.823	0.3	0.802	0.4	0.786	0.7
1	0.720	1	0.689	0.9	0.627	1.8	0.690	1.8	0.761	1.7	0.741	0.7	0.764	0.9	0.728	1.3	0.714	1.1
0.5	0.408	3	0.318	0.9	0.237	0.5	0.390	2.2	0.478	3.0	0.495	1.0	0.534	1.3	0.384	0.7	0.460	2.0

Table 5.1: Output ratios determined by 9 detectors and the corresponding calculated uncertainty-u (1sd) for 6 MV. SSD = 95 cm; SDD = 100 cm. (See section 3.2.2)

Field size (cm)	Radiochromic film		RK		PTW-31010		PTW-31016		PFD		EFD		Edge		TLD-700		TLD-700R	
	OR	u(%)	OR	u(%)	OR	u(%)	OR	u(%)	OR	u(%)	OR	u(%)	OR	u(%)	OR	u(%)	OR	u(%)
10	1		1		1		1		1		1		1		1		1	
9	0.986	0.5	0.992	0.03	0.993	0.1	0.993	0.03	0.991	1.5	0.991	0.4	0.990	0.1				
8	0.980	0.5	0.981	0.04	0.985	0.1	0.983	0.04	0.983	1.5	0.979	0.4	0.979	0.1				
7	0.969	0.5	0.969	0.08	0.974	0.1	0.974	0.1	0.973	1.5	0.969	0.4	0.966	0.1	0.971	0.3		
6	0.964	0.8	0.955	0.1	0.962	0.1	0.961	0.1	0.958	1.5	0.955	0.4	0.952	0.1				
5	0.944	0.7	0.939	0.1	0.946	0.1	0.945	0.1	0.945	1.5	0.938	0.4	0.935	0.1	0.949	0.8		
4.5	0.939	0.8	0.930	0.1	0.937	0.2	0.936	0.1	0.937	1.5	0.929	0.4	0.925	0.1	0.928	0.3		
4	0.934	0.7	0.919	0.1	0.927	0.2	0.926	0.1	0.925	1.5	0.919	0.4	0.916	0.1	0.909	0.3		
3.5	0.905	0.6	0.907	0.1	0.916	0.2	0.915	0.1	0.916	1.5	0.906	0.4	0.903	0.1	0.896	0.3		
3	0.905	1.0	0.894	0.1	0.902	0.2	0.901	0.1	0.905	1.5	0.895	0.4	0.890	0.1	0.893	0.4		
2.5	0.895	1.0	0.879	0.1	0.886	0.2	0.886	0.1	0.892	1.5	0.884	0.4	0.878	0.1	0.880	0.3		
2	0.862	0.6	0.857	0.1	0.860	0.3	0.866	0.1	0.875	1.5	0.866	0.4	0.858	0.1	0.860	0.4	0.864	1
1.5	0.822	0.6	0.819	0.1	0.811	0.6	0.829	0.3	0.851	1.5	0.841	0.4	0.833	0.3	0.819	0.4	0.815	1
1	0.750	0.6	0.717	1.0	0.657	2.5	0.726	1.6	0.784	1.8	0.775	0.6	0.775	0.9	0.751	0.3	0.761	1
0.5	0.478	2.4	0.342	1.0	0.261	0.7	0.427	2.2	0.520	3	0.552	1.4	0.552	1.3	0.409	1.4	0.517	1

Table 5.2: Output ratios determined by 9 detectors and the corresponding calculated uncertainty-u (1sd) for 6 MV FFF. SSD = 95 cm; SDD = 100 cm. (See section 3.2.2)

Field size (cm)	Radiochromic film		RK		PTW-31010		PTW-31016		PFD		EFD		Edge		TLD-700		TLD-700R	
	OR	u(%)	OR	u(%)	OR	u(%)	OR	u(%)	OR	u(%)	OR	u(%)	OR	u(%)	OR	u(%)	OR	u(%)
10	1	0.8	1		1		1		1		1		1		1		1	
9	0.998	0.9	0.987	0.05	0.988	0.05	0.988	0.05	0.987	0.05	0.987	0.05	0.990	0.05				
8	0.987	1	0.971	0.05	0.974	0.05	0.974	0.05	0974	0.05	0.973	0.05	0.979	0.05				
7	0.958	0.9	0.954	0.1	0.958	0.1	0.957	0.1	0.959	0.1	0.956	0.1	0.967	0.1	0.950	0.7		
6	0.950	1.4	0.936	0.1	0.939	0.1	0.938	0.1	0.939	0.1	0.935	0.1	0.952	0.1				
5	0.926	1.4	0.913	0.1	0.917	0.1	0.916	0.1	0.919	0.1	0.913	0.1	0.936	0.1	0.910	0.3		
4.5	0.905	1.9	0.901	0.1	0.904	0.1	0.904	0.1	0.909	0.1	0.902	0.1	0.926	0.1	0.892	0.6		
4	0.886	1	0.887	0.1	0.890	0.1	0.890	0.1	0.894	0.1	0.888	0.1	0.914	0.1	0.888	0.8		
3.5	0.859	0.9	0.871	0.1	0.874	0.1	0.874	0.1	0.881	0.1	0.874	0.1	0.904	0.1	0.871	0.9		
3	0.844	1.2	0.852	0.1	0.853	0.1	0.853	0.1	0.865	0.1	0.856	0.1	0.890	0.1	0.847	0.4	0.850	0.7
2.5	0.823	1	0.825	0.1	0.824	0.1	0.826	0.1	0.843	0.1	0.834	0.1	0.873	0.1	0.833	0.9		
2	0.777	0.9	0.783	0.2	0.776	0.3	0.787	0.3	0.813	0.1	0.800	2	0.845	0.1	0.789	0.5	0.778	1.1
1.5	0.734	1.5	0.715	0.3	0.693	0.5	0.720	0.4	0.763	0.1	0.749	0.4	0.800	0.1	0.732	0.3	0.738	0.7
1	0.631	1.8	0.569	1.5	0.518	1.3	0.578	1.2	0.653	0.6	0.639	0.5	0.695	1	0.615	0.5	0.601	1
0.5	0.323	2.4	0.247	0.7	0.196	0.7	0.295	1.1	0.367	1.2	0.363	1.4	0.429	1.4	0.309	0.4	0.339	1.2

Table 5.3: Output ratios determined by 9 detectors and the corresponding calculated uncertainty-u (1sd) for 10 MV. SSD = 90 cm; SDD = 100 cm. (See section 3.2.2)

Field size (cm)	Radiochromic film		RK		PTW-31010		PTW-31016		PFD		EFD		Edge		TLD-700		TLD-700R	
	OR	u(%)	OR	u(%)	OR	u(%)	OR	u(%)	OR	u(%)	OR	u(%)	OR	u(%)	OR	u(%)	OR	u(%)
10	1		1		1		1		1		1		1		1		1	
9	0.996	0.7	0.992	0.03	0.992	0.03	0.992	0.03	0.990	0.03	0.992	0.03	0.996	0.03				
8	1.010	0.8	0.981	0.04	0.982	0.04	0.983	0.04	0.981	0.04	0.982	0.04	0.989	0.04				
7	0.985	0.7	0.969	0.1	0.971	0.1	0.971	0.1	0.973	0.1	0.968	0.1	0.982	0.1	0.964	0.5		
6	0.988	0.5	0.956	0.1	0.958	0.1	0.958	0.1	0.957	0.1	0.955	0.1	0.971	0.1				
5	0.967	0.9	0.937	0.1	0.941	0.1	0.942	0.1	0.944	0.1	0.939	0.1	0.961	0.1	0.948	0.5		
4.5	0.956	1.1	0.929	0.1	0.931	0.1	0.933	0.1	0.935	0.1	0.930	0.1	0.953	0.1	0.930	0.4		
4	0.942	0.8	0.918	0.1	0.920	0.1	0.921	0.1	0.925	0.1	0.918	0.1	0.948	0.1	0.923	1		
3.5	0.917	1	0.905	0.1	0.906	0.1	0.907	0.1	0.914	0.1	0.909	0.1	0.938	0.1	0.900	0.8		
3	0.894	0.9	0.886	0.1	0.888	0.1	0.888	0.1	0.901	0.1	0.896	0.1	0.928	0.1	0.889	0.5	0.898	0.9
2.5	0.866	0.8	0.863	0.1	0.862	0.1	0.865	0.1	0.881	0.1	0.873	0.1	0.914	0.1	0.867	0.4		
2	0.851	1	0.825	0.2	0.819	0.2	0.829	0.2	0.853	0.1	0.845	0.1	0.888	0.1	0.825	0.8	0.839	1
1.5	0.797	0.8	0.760	0.2	0.743	0.4	0.767	0.3	0.807	0.2	0.799	0.1	0.848	0.2	0.769	0.5	0.787	1
1	0.689	1	0.618	1.5	0.572	1.4	0.624	1.5	0.704	0.9	0.704	1	0.747	1	0.655	0.9	0.689	1
0.5	0.370	1.8	0.280	0.7	0.219	0.7	0.335	1	0.416	1.6	0.450	2	0.486	1.4	0.349	0.4	0.392	1

Table 5.4: Output ratios determined by 9 detectors and the corresponding calculated uncertainty-u (1sd) for 10 MV FFF. SSD = 90 cm; SDD = 100 cm. (See section 3.2.2)

length larger than 2.5 cm, FOF were found to be consistent with differences lower than 0.8 % between the averaged FOF determined using ionization chambers and previously published data [67, 66] for the four energies studied. The eight detectors analyzed showed the same behaviour for FF and FFF beams. Higher differences than expected were found when using the radiochromic film EBT-2 for several field sizes.

The response of the RK and PTW-31016 was similar for field sizes with a side length larger than 1 cm. However, it was lower than diodes for field sizes up to 2 cm for all energies. The response of the different ionization chambers is related to their cavity volume. Both models present a similar area on the plane perpendicular to the beam. In the case of the RK model, it was positioned with the stem parallel to the beam axis, while the PTW-31016 was placed perpendicular to the beam axis. The same volume effect could explain the response of the 3.1 mm square TLD. The OR for this detector are higher for the 1 cm square field than for any of the ionization chambers. However, the dimensions of this detector are too large for the 0.5 cm square field.

5.4 Field output factor determination for square fields up to 2 cm side length

Table 5.5 shows PTW-31016 FOF derived from the experimental data corrected by $k_{Q_{clin},Q_{msr}}^{f_{clin},f_{msr}}$ from Table 4.7 compared with MC simulated FOFs. The FOF determined with radiochromic films and TLD-700R are also included. OR are presented in the case of the Edge detector, although no specific correction factors are available for these energies and field sizes, they are included to facilitate comparison. The uncertainty is calculated as men-

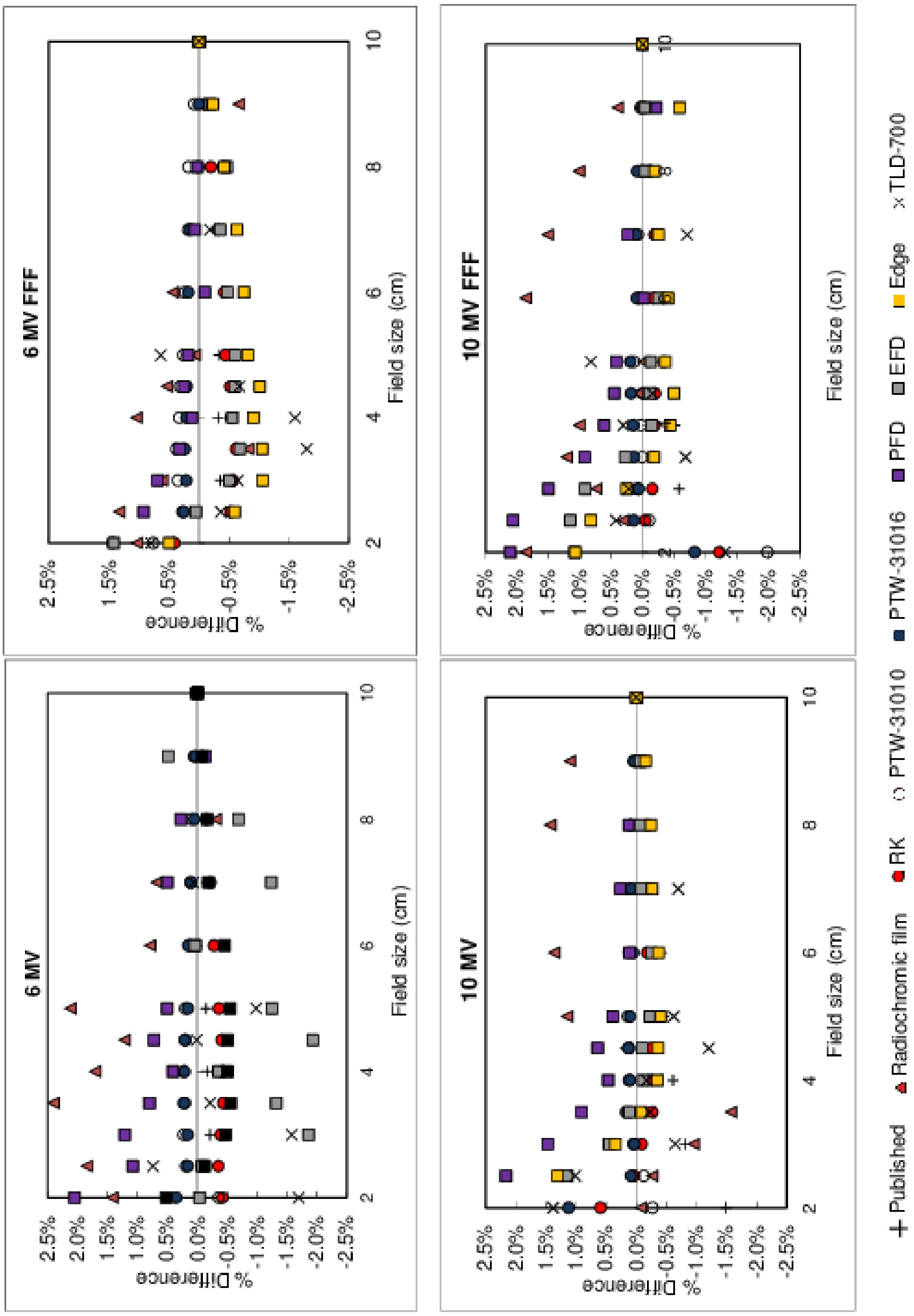

Figure 5.3: Percentage difference in field output factors (FOF) for field sizes from 2.5 to 10 cm, with reference to the average FOF determined by the ionization chambers. Published results acquired under the same conditions are also presented: Chang et al 2012 for 6 MV and 6 MV FFF and Fogliata et al 2012 for 10 MV and 10 MV FFF

tioned in section 3.2.2 except for FOF from PTW-31016 where it is calculated by combining the uncertainty of OR and $k^{f_{clin},f_{msr}}_{Q_{clin},Q_{msr}}$.

The differences between the FOF obtained correcting OR from the PTW-31016 and the ratios obtained using the TLD-700R, radiochromic film and MC simulation are presented in Figure 5.4. It can be observed that there is good agreement for TLD with differences lower than 2.9% except for the 1 cm square for 10 MV FFF. However, the similarity in the response of MC and radiochromic film could suggest some error in the OR determined using the PTW-31016 in this case. On the other hand, the differences with radiochromic film are higher, especially for the smallest field size.

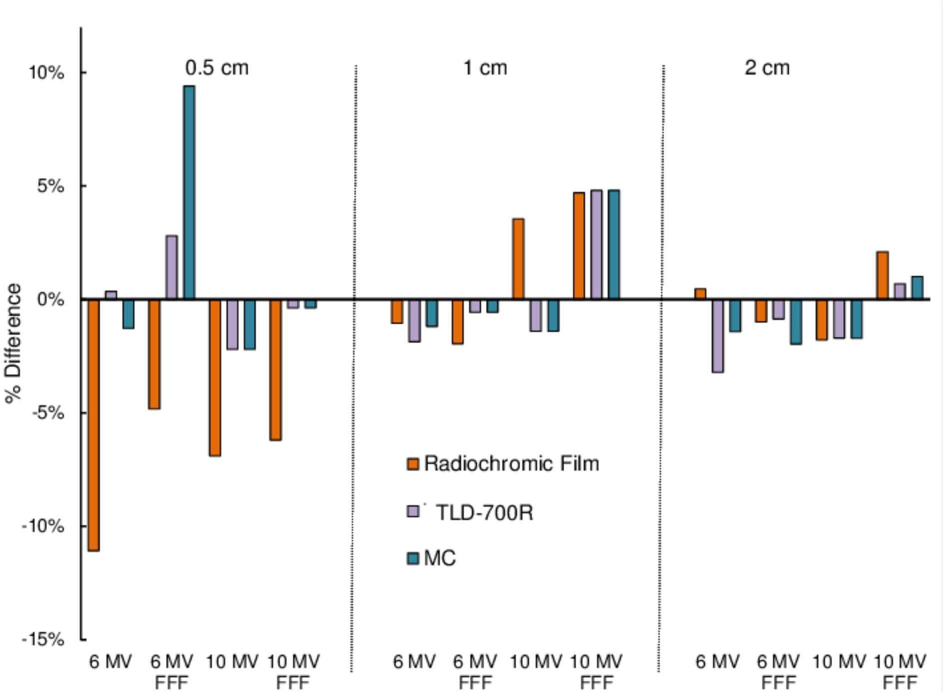

Figure 5.4: TLD-700R, radiochromic film and MC differences on FOF compared with corrected values obtained with PTW-31016

	Field size length (cm)									
	2		1		0.5		0.49		0.45	
	FOF	u (%)	FOF	u (%)	FOF	u (%)	FOF	u (%)	FOF	u (%)
6 MV (SSD = 95 cm; 5 cm depth)										
MC	0.840	1.5	0.720	1.5	0.453	1.5	0.453	1.3	0.296	1.4
PTW-31016	0.852	0.3	0.728	2	0.459	3.6				
TLD-700R	0.825	1.0	0.714	1.1	0.460	2.0				
Rad. Film	0.856	1.0	0.720	1.0	0.408	3.0				
Edge*	0.848	0.1	0.764	0.9	0.534	1.2				
6 MV FFF (SSD = 95 cm; 5 cm depth)										
MC	0.854	1.3	0.780	1.3	0.549	0.9	0.472	1.2	0.439	1.1
PTW-31016	0.871	0.3	0.766	2	0.503	3.6				
TLD-700R	0.864	1.1	0.761	0.6	0.517	1.1				
Rad. Film	0.862	0.6	0.750	0.6	0.478	2.4				
Edge*	0.858	0.1	0.775	0.9	0.552	1.3				
10 MV (SSD = 90 cm; 10 cm depth)										
MC	0.778	1.2	0.594	1.3	0.318	1.3	0.310	1.3	0.280	1.2
PTW-31016	0.792	0.3	0.609	2	0.347	3.				
TLD-700R	0.778	1.1	0.601	1.0	0.339	1.2				
Rad. Film	0.777	0.9	0.631	1.8	0.323	2.4				
Edge*	0.806	0.1	0.658	1.0	0.415	1.4				
10 MV FFF (SSD = 90 cm; 10 cm depth)										
MC	0.840	0.1	0.675	0.1	0.382	0.1	0.373	0.6	0.335	0.1
PTW-31016	0.834	0.3	0.658	2	0.394	3				
TLD-700R	0.839	1.5	0.689	1.3	0.392	0.7				
Rad. Film	0.851	1.0	0.689	1.0	0.370	1.8				
Edge*	0.844	0.1	0.705	0.9	0.459	1.4				

Table 5.5: FOF determined by MC simulation, PTW-31016 obtained by applying the correction factors, TLD-700R and Radiochromic film for the four energies analyzed. *OR (ratios non-corrected) obtained using the Edge detector are also included

5.5 Geometric Inaccuracies

Detector set-up

The influence of the PTW-31016 set-up was studied during the determination of $k^{f_{clin},f_{msr}}_{Q_{clin},Q_{msr}}$ by MC simulation and has already been presented in Table 4.4.

The analysis performed for the FFF energies using a 1 mm x 1 mm x 2 mm voxel matrix defined around the geometric centre for the 0.5 cm square field size shows that differences of 1 mm around the centre result in differences of up to 6.5% in the output factor for all energies studied. These differences are reduced to 1% for the 1 cm square field size.

Jaw set-up

As was explained in section 3.2.5, 0.45 and 0.49 cm square fields were defined for all energies to study the effect of jaw tolerances on FOF determination by MC simulation. The effect of the accuracy of the jaws is shown in Table 5.5 where a 0.5 mm change in the 0.5 cm square field can lead to large differences in the field output factor.

Measurements were repeated using the TLD-700R and the Edge detector in a second TrueBeam from ECC. Figure 5.5 shows the differences between the output ratios for both LINACs. These differences are consistent with MC results given the uncertainty of the 0.5 cm square field. Consistency is reinforced by the fact that at the four energies, the differences in the LINACs show a similar value and the same direction. The comparison also shows better reproducibility of the Edge detector compared with the TLDs. TLDs present a higher variability which is partially associated with set-up difficulties due to the lack of an immediate read-out of these detectors.

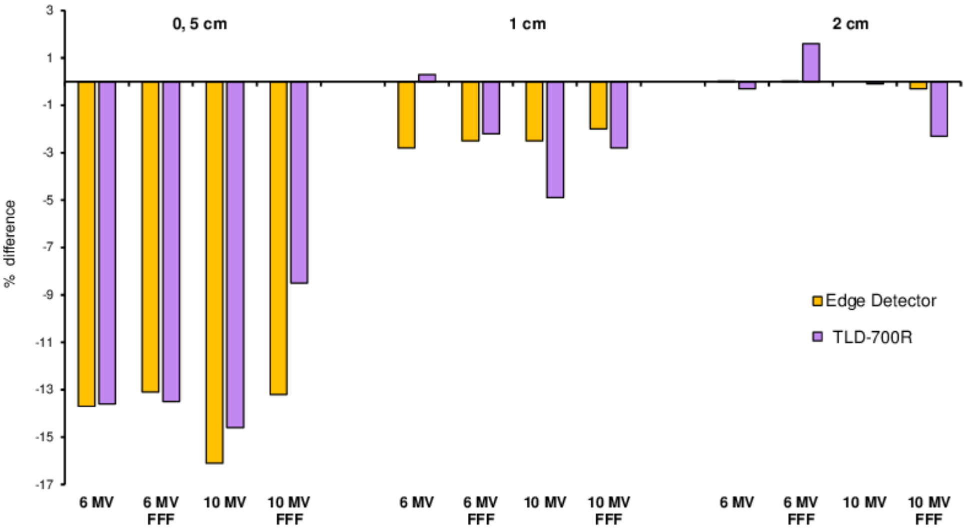

Figure 5.5: Output reading differences between two LINACs. Outputs were determined using the Edge detector and the TLD-700R under isocentric conditions: 5 cm depth for 6 MV and 6 MV FFF and 10 cm depth for 10 MV and 10 MV FFF

5.6 Analysis and discussion

5.6.1 Detector Response

The nine detectors analyzed showed the same behaviour for FF and FFF beams, even for small fields, which had also been noted recently by Lechner et al [103]. Table 5.5 shows good agreement (differences lower than 5%) between corrected PTW-31016 FOF and TLD-700R. Radiochromic film showed a good response in square fields larger than 2 cm and a better response than the ionization chambers for smaller fields. The electronic and mass density of this detector, which is close to water, combined with dose rate independence, low energy dependence and high resolution give it a potential advantage over other detectors. However, custom calibration must be performed and it must be compared with other detectors. At the same time, Figure 5.4 shows a higher dispersion in the differences compared with FOF obtained using PTW-31016.

The largest OR values for the smallest field sizes were found using the diodes. Small differences between the shielded and unshielded diodes from Scanditronix were observed. The Edge detector had the largest OR for the smaller field sizes. Several works show that for small field sizes this type of detector, and diodes in general, need correction factors smaller than 1 [98, 99]. Francescon et al [94, 95] report an overestimation of the Edge detector for nominal 6 MV (FF and FFF) beams from 5 to 8% for 0.5 cm field size. In our case the correction factor seems to be larger. However, the uncertainty assigned to the final FOF determined with PTW-31016 does not allow a better estimate of the Edge correction factors for the 0.5 cm field size. In Table 5.6 the $k_{Q_{clin},Q_{msr}}^{f_{clin},f_{msr}}$ obtained from our measurements for the Edge detector are shown. These ratios are derived from the corrected values using PTW-31016. The uncertainty is derived from the combination of OR with the Edge detector and the FOF uncertainties using PTW-31016. Small differences in $k_{Q_{clin},Q_{msr}}^{f_{clin},f_{msr}}$ between flattened and unflattened beams were found for higher energies.

Field size (mm)	6 MV		6 MV FFF		10 MV		10 MV FFF	
5	0.86	3.2%	0.91	3.3%	0.84	3.3%	0.86	3.3%
10	0.95	2.2%	0.99	2%	0.93	1.7%	0.93	1.9%
20	1.005	0.7%	1.015	0.7%	0.982	0.8%	0.988	0.8%

Square fields. SDD =100 cm. Depth = 5 cm for 6 MV FF and FFF and 10 cm for 10 MV FF and FFF

Table 5.6: $k_{Q_{clin},Q_{msr}}^{f_{clin},f_{msr}}$ for the Edge detector derived from FOF determined with the PTW-31016. (1 sd)

A new work presented by Tanny [123] recently appeared (September, 2015) based on experimental measurements, proposing $k_{Q_{clin},Q_{msr}}^{f_{clin},f_{msr}}$ for an Edge detector for Truebeam beams. However, no direct comparison can be done due to differences in SSD and also field sizes since fields are defined by cones. Values proposed by Tanny are presented in Table 5.7. As Francescon [90] pointed out, $k^{f_{clin},f_{msr}}_{Q_{clin},Q_{msr}}$ depends not only on the field size, but also on the depth where they are determined. However their dependence on larger field sizes is lower. Therefore, the results presented in Tables 5.6 and 5.7 are in agreement (considering the uncertainties) for field sizes of 1 cm and larger.

Field size (mm)	6 MV	6 MV FFF	10 MV FFF
6	0.936	0.949	0.901
8	0.946	0.963	0.929
10	0.957	0.977	0.944
20	1.001	1.006	0.983

Circular fields. SDD =100 cm. Depth = 10 cm

Table 5.7: $k^{f_{clin},f_{msr}}_{Q_{clin},Q_{msr}}$ for Edge detector proposed by Tanny for a TrueBeam. Field sizes defined by cones

5.6.2 Geometrical inaccuracies

The FOF results obtained by MC simulation for the smallest field size, 0.5 cm square, did not agree with the experimental data (Table 5.5). Gete et al [102] also observed such discrepancies for 6 MV FFF for 1.0 cm square field size. However, the 2 mm x 2 mm x 10 mm voxel size used in their case may explain these differences.

Jaw position accuracy has a great influence on the output factor for smaller field sizes due to partial occlusion of the target. This makes it difficult to use MC methods to determine the field output factor of a particular LINAC because, even with high resolution in the simulation, it is impossible to know the true jaw position with the appropriate accuracy. Differences in field size determination using radiochromic film were found to be approximately 0.2 mm. Therefore, a 4.9 mm field was also simulated to study what the influence of 0.1 mm on the final output was.

The standard proposal to determine FOF with detectors that need a correction factor is to apply appropriate $k^{f_{clin},f_{msr}}_{Q_{clin},Q_{msr}}$ either obtained experimentally or by MC, to the detector readings. However, the influence of the jaws and detector set-up on the correction factors has only recently been reported for a field size error of 1 mm for flattened beams [91]. In Chapter 4, we investigated a field size uncertainty of 0.5 mm so a MC simulation of the PTW-31016 was carried out for all energies for 0.45 and 0.5 cm square fields. Jaw inaccuracies were found to have a greater effect on FOF than set-up detector inaccuracies for the smallest field size, which agrees with the findings of Charles et al for FF beams [91].

5.6.3 Correction factors

The PTW-31016 chamber correction factors, $k^{f_{clin},f_{msr}}_{Q_{clin},Q_{msr}}$, calculated by MC for a 10 MV unflattened Truebeam beam in nominal square fields side length of 2.0 cm, 1.0 cm and 0.5 cm (Table 4.7) were used for the four energies. FOF obtained using PTW–31016 agree with experimental FOF measured with TLDs and with values obtained by MC. Differences with TLDs are lower than 3.2% except for the 1 cm square field for 10 MV FFF discussed previously. Differences with MC simulation are lower than 2.3% except for the same field and energy than TLDs (1 cm; 10 MV FFF) and also for the 0.5 cm field size for 6MV FFF (9.4% difference). This discrepancy can be explained by the uncertainty in the field size due to the LINAC jaw inaccuracy. Thus, agreement between the discussed results also shows low energy dependance for $k^{f_{clin},f_{msr}}_{Q_{clin},Q_{msr}}$ for all the energies studied.

The simulation of jaw set-up showed large differences in the output factor for the 0.5 cm square field. These were greatest for 6 MV FFF, where 0.1 mm represents a difference of approximately 15% in the output factor. This effect was checked by comparing two Truebeam LINACs from two different institutions. The strong similarity between all parameters in the two TrueBeams does not apply to the smaller field sizes. A difference of approximately 13% was found for FOF between both LINACs for 6 MV and 0.5 cm field size (Figure 5.5).

It is our recommendation that MC simulated results and measurements should not be merged for determining correction factors for field sizes below 1 cm, where jaw accuracy is relevant. Correction factors derived from MC simulations refer to a specific field size and we have seen that differences of 0.5 mm in jaw position can lead to 2.2% differences in $k_{Q_{clin},Q_{msr}}^{f_{clin},f_{msr}}$ for PTW-31016 (Chapter 4). However, these changes are much smaller than the change in the FOF related to manufacturer jaw uncertainty. The final uncertainty of the FOF includes both the experimental uncertainty in the measurement and the effect of jaw inaccuracies on the correction factor.

The backscatter effect on the final output factors has been estimated to be 1.5% for small fields by Cranmer-Sargison et al [111]. Other authors have found good agreement without considering backscatter [102]. However, due to the final uncertainty in our results no firm conclusions about backscatter can be made.

In a recent work presented by Benmakhlouf et al [124] correction factors for PTW-31016 in a 6 MV Varian beam are proposed. These results cannot be directly compared since their determination conditions are at SSD of 100 cm and 10 cm depth. Nevertheless, agreement is reasonable for the $k_{Q_{clin},Q_{msr}}^{f_{clin},f_{msr}}$ correction factor for a 0.5 cm square. 1.147 in their case for a field size of 0.55 cm on the detector plane, while it is 1.176 in our case for

0.5 cm on the detector plane. For the 1 cm square field our value is closer to that proposed by Czarnecki and Zink [96], where the underestimation for PTW-31016 is expected to be approximately 5%.

5.7 Conclusions

The response of nine detectors has been characterised for both flattened and unflattened beams. In fields larger than 2 cm x 2 cm the detectors showed comparable results. However, in smaller fields the geometry and nature of the detectors had a significant impact on response and this was found to be the same for both flattened and unflattened beams.

The results show that the ionization chambers studied are not suitable for square field sizes below 2 cm, unless correction factors are used. Radiochromic film and TLD-700R gave reasonable results without a specific correction factor. Radiochromic film is a promising detector for small fields when relative measurements are performed on flattened or unflattened fields. However, due to the large variability in their response, it is strongly recommended that it is not used as a single detector, but is compared with the response of other types of detector. Despite their depth resolution (6 mm), TLD-700R are suitable for the field sizes studied. However, set-up is critical, because of the lack of an immediate read-out, their use is not very practical for systematic measurements.

Comparing our results with previously published studies there are negligible differences in the main parameters for field sizes larger than 2 cm side length. This should help new users gain confidence when their measured parameters agree with those published.

The results show the need to perform machine-specific measurements for fields below 1.5 cm, and verification after jaw calibration. The proposed

PTW-31016 correction factors in Chapter 4 have been applied to calculate FOF at the four energies studied (6 MV and 10 MV FF and FFF) and show the low dependence that these factors exhibit for this ionization chamber model.

Chapter 6

Contributions to SABR treatments. Results and discussion

The results presented have been obtained following the methodology detailed in section 3.3.

6.1 Set-up and initial verifications

This section explores the effect that the level of modulation has on final dose distributions in lung SABR treatments and the influence that the number of cycles has on the borders of the fields. Set-up proposal for lung SABR treatments is also included.

6.1.1 The effect of low modulated plans

Figure 6.1 shows the comparison between irradiated films and predicted dose distributions in TPS for both initial and low modulated plans for the first 6 patients (See section 3.3.1). The percentage of points with $\gamma(3\%, 3mm) > 1$ is presented.

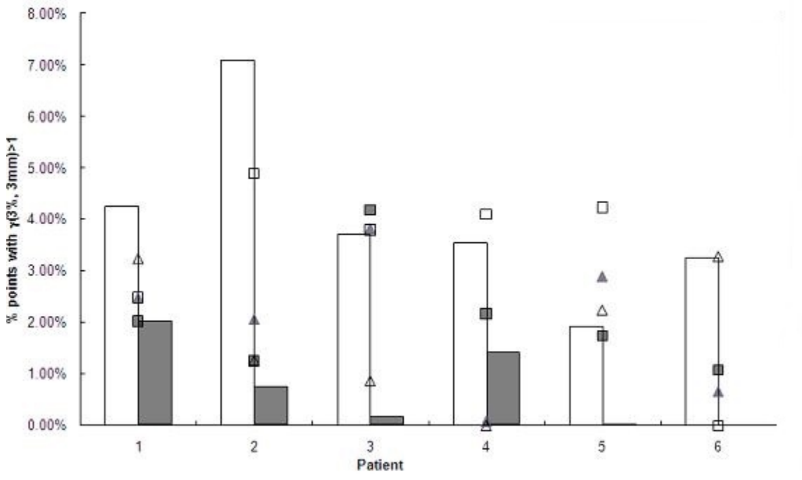

Figure 6.1: Percentage of points with $\gamma(3\%, 3mm) > 1$ for two different levels of modulation for 6 patients. In all cases white represents the initial modulation while grey shows a plan for the same patient and localization with a lower modulation. Comparison between static and dynamic conditions is presented in vertical bars. Triangles represent comparison between TPS dose distributions and measurements on the Quasar phantom in static conditions. Squares show the comparison between TPS and measurements performed in dynamic mode of 12 bpm and 1 cm peak to peak

SABR protocols accept maximum doses in PTV as high as 140% of the prescription dose, this means that there is no need for a high modulation. On the other hand, tests performed on 10 patients showed that it was not possible to achieve all dosimetric constraints for all patients without minimum modulation when coplanar arcs are used.

The vertical bars from Figure 6.1 show that the diminution in modulation has an effect on the final dose distribution compared with static conditions.

In addition, in all cases the static absorbed dose distribution of the 12 plans (triangles) was acceptable when compared with the absorbed dose distribution planned with the TPS. This means that the TPS is properly tuned and the modulation is not excessive in any case in static conditions. This analysis is proposed to be used as a routine method for motion verifications, particularly when hypo-fractionated treatments are considered.

Higher differences between static-TPS plans (triangles) than the dynamic and TPS (squares) were found for patients 1 and 6. This may be due to an effect of compensation at some points between the predicted and delivered doses, together with the uncertainty in the radiochromic film.

Several studies were summarised in the Introduction which analyze the interplay effect. Most of the studies showed a decrease in the final effect when 30 fractions are delivered. However, there is no general consensus in the scientific community on the influence of intra-fraction movement and modulation of the plan when a small number of fractions is delivered. It could be argued that analysis of the interplay effect is only performed in one fraction instead of 3 or 5 fractions which the real treatment would have and consequently a decrease of this effect should be expected. It was decided not to assume any statistical consideration due to the small number of fractions and be more restrictive in the definition of a valid plan, accepting a plan only when the interplay effects fulfill the gamma criteria described for each fraction.

[1]

---

[1] The set-up proposal consisted of 4 arcs 200°-220° long (two arcs for 10 MV FFF) and the verification method proposed, based on the comparison of two irradiations (static and dynamic) on the Quasar phantom were presented at the 2nd Annual UPMC Beacon Hospital and UPMC International SRS/SBRT Symposium in Dublin, and it was awarded 1st prize in the Young Investigator's Award in 2013.

6.1.2 Number of breathing cycles included in each arc

The maximum dose difference between the dose distribution for n periods and n periods and a half is shown in Figure 6.2. The distribution was derived from the convolution of a static profile with a weighted function that represents the time that the volume is in each position when sinusoidal motion of the volume is considered. A minimum of 8 periods must be included to have a maximum difference lower than 2% on the dose distribution for the three energies. The number of cycles needed is not dependent on the type of radiation beam (energy and/or flattening filter). It is important to notice that this effect is independent of the modulation and will also affect conformed beams/arcs.

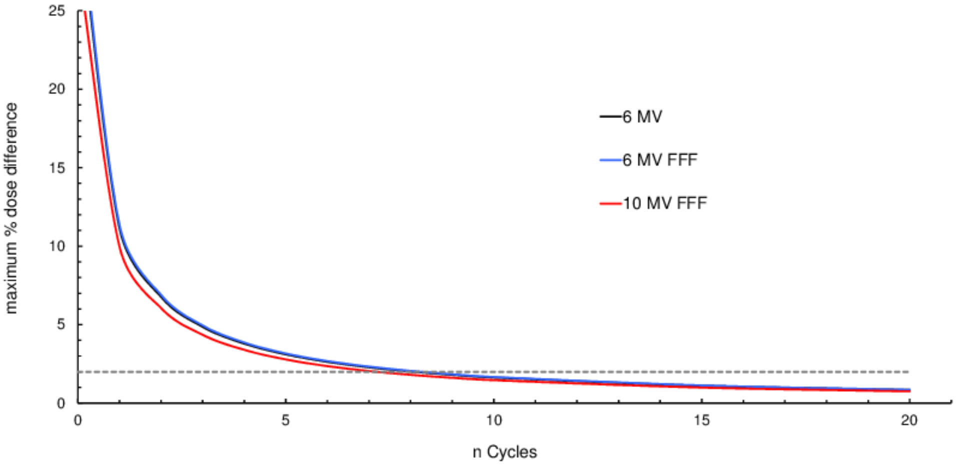

Figure 6.2: Maximum dose difference at any point of the dose distribution, between static profiles and profiles irradiated for n periods and a half as a function of the n periods

6.2 PUMA, a method to evaluate the interplay effect in lung SABR treatments irradiated with VMAT

6.2.1 Analysis and discussion

In the preliminary investigations low modulated versions of plans 1 to 6, were created (plans presented in section 6.1.1). Table 6.1 shows the ALPO for each plan and the results obtained by PUMA compared with those obtained by film irradiation inserted within the QUASAR phantom. The observation that lower modulation resulted in a higher percentage of points passing PUMA and radiochromic film analysis meant that only low modulation plans were considered. Subsequently, a further 6 patients, with low modulated plans were included in the analysis (Plans 13 to 18).

To study the suitability of PUMA for verifying FFF plans, five of the patients in the study were planned using 10 MV FFF. Figure 6.3 presents the results of the comparison between PUMA and the QUASAR phantom for the 23 plans proposed in the study.

ALPO is a statistical parameter that can be used to compare different modulation levels for the same volume, but cannot be used directly to predict the interplay effect, as is suggested by the results included in Table 6.1.

Both PUMA and film have been shown to be sensitive to different levels of modulation. However, PUMA does not require accelerator time and can significantly reduce the total verification time. ALPO can be used to compare different levels of modulation, however, it is affected by tumour volume and is difficult to use to assess the interplay effect.

The PUMA method investigates the interplay effect by emulating periodic tumour motion. Although the sine and cosine waveforms used are

Patient	Plan number	ALPO (cm)	PUMA*	Quasar + Rad. Film*
1	1	1.96	4.9 %	4.3 %
	7	3.42	0.0 %	2.0 %
2	2	2.04	9.2 %	7.1 %
	8	2.71	3.2 %	2.5 %
3	3	2.74	11.7 %	3.7 %
	9	3.10	0.4 %	0.2 %
4	4	1.92	2.1 %	3.6 %
	10	3.56	0.0 %	1.4 %
5	5	1.89	1.2 %	3.3 %
	11	2.39	0.0 %	0.0 %
6	6	1.38	17.8 %	8.1 %
	12	2.35	4.5 %	0.0 %

**Percentage of points failing the acceptance criteria*

Table 6.1: Interplay effect analysis performed on 6 patients for two different levels of modulation using PUMA and the Quasar phantom. Plans 1 to 6 represent the initial modulation and plans 7 to 12 have lower modulation. The average leaf pair aperture (ALPO) is also scored

idealistic, they cover situations where irradiation begins with the tumour at the centre (sine) and at the edge (cosine) of the field. The method could, however, be easily adapted to any breathing waveform or tumour motion.

Both methods agree on the suitability of the plans with the exception of plan 3. The PUMA method predicts an unacceptable interplay effect, which is not identified by the film. This may be due to the fact that PUMA analyses the whole ITV instead of only the sagittal plane in the case of film. These preliminary results indicate that PUMA may be an effective alternative to film-based verification. At present, it is being used to prevent plans failing QUASAR film verification. However, in the future, it could be used as an exclusive method for verification. In addition, the same method could be adapted to verify the interplay effect in IMRT lung SABR plans. It is also

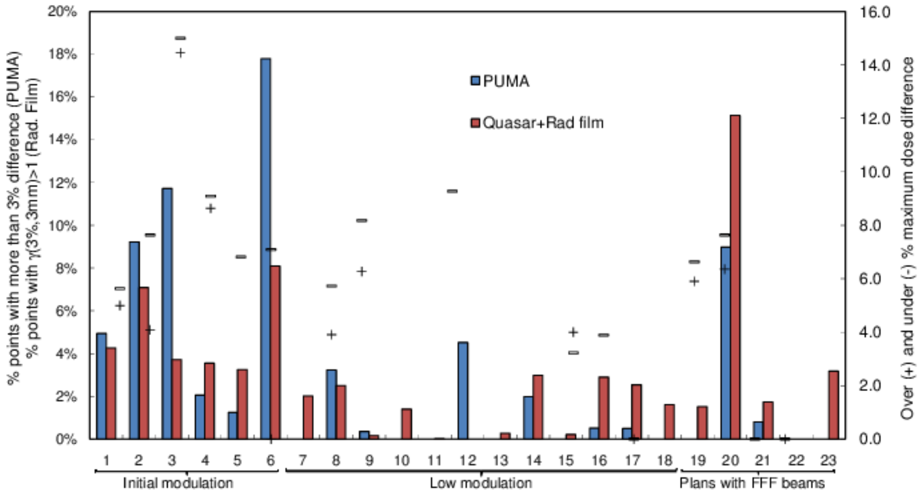

Figure 6.3: Interplay effect analysis. Comparison between PUMA method and verifications performed on a Quasar phantom comparing static and dynamic dose distributions. For the PUMA method the positive and negative difference between the plan with a unique isocentre and the most unfavourable plan created by applying sine or cosine functions at the position of the isocentre on the cranio-caudal direction

important to notice that PUMA method can also be used for all energies as well as with flattened and unflattened beams.

6.2.2 PUMA compared with other methods/modulation indices

Modulation indices calculated for the 23 plans are scored in Table 6.2. At present, there are no published values for the proposed indices to evaluate the interplay effect. As already mentioned previously, the interplay effect is a combined effect of modulation and motion. The initial analysis performed was based on the correlation between the proposed indices and radiochromic film. A statistical analysis of the goodness of fit was done and determined that there is significant correlation ($p < 0.0001$) between radiochromic film and PUMA, radiochromic film and MIt and also between PUMA and MIt.

According to these results just PUMA and MIt seem to be able to predict failing plans in a Quasar phantom.

Plan	Rad. film	PUMA	MCS	MIt	AI
1	4.3	4.9	0.19	0.83	5.75
2	7.1	9.2	0.20	0.72	5.31
3	3.7	11.7	0.24	0.66	6.68
4	3.6	2.1	0.18	0.70	8.33
5	3.3	1.2	0.24	0.49	4.28
6	8.1	17.8	0.60	1.04	1.69
7	2	0.0	0.45	0.33	1.86
8	2.5	3.2	0.28	0.45	3.49
9	0.2	0.4	0.31	0.54	4.69
10	1.4	0.0	0.41	0.37	3.50
11	0.0	0.0	0.31	0.44	3.08
12	0.0	4.5	0.32	0.44	2.81
13	0.3	0.0	0.42	0.38	2.24
14	3.0	2.0	0.43	0.55	5.11
15	0.2	0.0	0.45	0.38	3.68
16	2.9	0.5	0.34	0.60	3.80
17	2.5	0.5	0.30	0.52	4.21
18	1.6	0.0	0.48	0.37	3.29
19	1.5	0.0	0.43	0.41	2.02
20	15.1	9.0	0.24	0.79	4.31
21	1.7	0.8	0.29	0.48	3.54
22	0.0	0.0	0.41	0.42	2.22
23	3.2	0.0	0.35	0.43	2.76

MCS - Proposed by McNiven 2010.[116]
MIt - Based on Park at 2014. [117]
AI - Introduced by Du in 2014. [118]

Table 6.2: Modulation indices proposed in the literature calculated for 23 plans, compared with percentage of points with $\gamma(3\%, 3mm) > 1$ on radiochromic film and percentage of points that fails the PUMA acceptance criterion. 4 arcs and 6 MV FF were used in plans 1 to 17 and two arcs 10 MV FFF for the last five plans

From analysis of Table 6.2, a value of 0.6 for the MIt index is proposed as the upper limit when evaluating the suitability of a plan to the interplay effect. This value was selected in order to minimize the number of false negative plans in the analysis. A positive plan is considered to be a plan suitable for treatment, while a negative plan is an unsuitable plan due to the interplay effect. Table 6.3 shows statistical parameters for PUMA and MIt. Both methods have the same specificity so all failing plans were detected. However PUMA, as discussed previously, has only a single false positive in comparison with the 3 false positives for MIt.

The low number of plans analyzed (23) until now must be considered before using the PUMA or MIt index as exclusive verification methods for the evaluation of the interplay effect.

Finally, it should be mentioned that the MIt analysis is much faster than PUMA and, of course, the Quasar phantom since it only requires the export of the treatment plan in DICOM format and run the software which takes less than one minute. The evaluation of a greater number of plans will contribute to setting 0.6 as the benchmark for MIt analysis or slightly modify it.

	Positive Predictive Value (PPV)	Negative Predictive Value (NPV)	Sensitivity	Specificity	Accuracy
PUMA	100 %	75%	95%	100%	95.7%
MIt	100 %	50%	85%	100%	87.0%

Table 6.3: Statistical analysis of PUMA and MIt

6.3 Conclusions

Low modulated coplanar arcs, properly verified, can be used in lung SABR. The MU delivered per Gy and ALPO are indicators of the modulation of a plan, but they are not suitable for evaluating the interplay effect.

PUMA predicts the effects of the volume motion and can be used to verify the interplay effect. In the future, PUMA could be used as an exclusive method for motion verification since it can be used for all energies as well as with FF and FFF beams.

Most of the modulation indices proposed in the literature are related to the robustness and modulation of a plan. However, none of them has been conceived to appropriately predict the interplay effect in lung SABR. MIt proposed by Park [117] has been found to be the only published index capable of detecting failing plans. MIt and PUMA have the same specificity since both detected all of the failing plans. However, PUMA has a greater accuracy and sensitivity. According to the results presented, 0.6 is proposed as the benchmark for the MIt index to evaluate the interplay effect in lung SABR.

Chapter 7

Final conclusions

This thesis has contributed to improve our knowledge of some of the present challenges in radiotherapy.

1. An upper limit for the influence that differences between chambers of the same model have on their k_{Q,Q_o}has been fixed for three of the most common ionization chambers used in radiotherapy, PTW-30013, PTW-31010 and PTW-31016. In addition, the manufacturing tolerances in the wall thickness of chambers of the same model have been identified as the main source of k_{Q,Q_o} variation. This sets the minimum uncertainty (0.5%) that should be assigned to any k_{Q,Q_o} used from protocols or the literature in general.
2. $k_{Q_{clin},Q_{msr}}^{f_{clin},f_{msr}}$ correction factors have been determined for the PTW-31016 ionization chamber model for unflattened beams from a Truebeam. The effect of the particularities of each individual chamber has been studied and their influence on final values has been found to be 0.6% for field sizes greater than or equal to one and 2.8% for 0.5 cm square field.

3. Output ratios for 6 MV and 10 MV flattened and unflattened beams from a Truebeam have been measured using nine detectors in the range 0.5 to 10 cm square side length. FOF has been determined experimentally and using MC. The FOF determined with the eight detectors analyzed for field sizes larger than 2 cm square show values within 2% between the average of several ionization chambers when compared with results from the literature.

4. FOF for 6 MV and 10 MV flattened and unflattened beams from a Truebeam were determined using PENELOPE MC code in the range 0.5 to 2 cm. It has been shown that below 2 cm, tested ionization chambers and diodes require correction factors.

5. FOF measured with TLDs and with PTW-31016 by applying the proposed $k_{Q_{clin},Q_{msr}}^{f_{clin},f_{msr}}$ correction factors agreed to within 5% even for the smallest field size (0.5 cm).

6. Low energy dependence of $k_{Q_{clin},Q_{msr}}^{f_{clin},f_{msr}}$ correction factors was verified for PTW-31016.

7. The Edge detector requires correction factors lower than 1 for field sizes below 2 cm. A range of values for the four energies analyzed and field sizes up to 2 cm have been proposed.

8. FOF values for the 0.5 cm square side length are machine specific, mainly due to the effect of LINAC jaw uncertainties in this range. Thus, MC calculation of FOF is not suitable in this case. Differences of up to 13% between FOF determined in two TrueBeams were found for 6 MV FFF.

9. A low modulated VMAT class solution has been proposed to deliver

both fast and accurate SABR treatments.

10. A minimum of 8 respiratory cycles should be included for a beam/arc during irradiation to diminish the effect of the number of breathing cycles independently of the modulation of the plan.
11. PUMA, a method to evaluate the interplay effect, has been developed and presents a higher specificity than any other index/method in the literature.
12. The MIt index was found to have a lower accuracy than PUMA. At present the MIt index is the only proposed index in the literature that can accurately predict the interplay effect in lung SABR.

Chapter 8

List of publications

Contributions to conferences proceedings

- Poster discussion **J Puxeu Vaqué**, W H Nailon, A P Sankar. PUMA – Predicted Upshot Motion Analysis; a method to evaluate the interplay effect in lung SABR treatments. 3rd ESTRO FORUM. Barcelona, 2015

- *Oral Communication* **J Puxeu Vaqué,** W H Nailon, P Drewell and A P Sankar. The influence of FFF beams on the interplay effect for SABR treatments. IPEM conference on Flattening Filter Free Photon Beams in Radiotherapy. London 2014

- *Oral Communication* **J. Puxeu Vaqué**, A Comrie , A P Sankar and W H Nailon. Modulation effects on the dose delivery of Stereotactic Ablative Radiation Therapy (SABR) Stereotactic Body Radiation Therapy (SBRT) .2nd Annual UPMC Beacon Hospital and UPMC International Stereotactic Radiosurgery and Stereotactic Body Radiotherapy Symposium. Dublin, 2013 ***awarded the 1st prize in The Young Investigator´s Award***

- *Oral Communication* **J Puxeu Vaqué**, A Comrie , A P Sankar and W H Nailon. Modulation effects on the dose delivery of Sterotactic Ablative Radiation Therapy. Scottish+ Radiotherapy Physics Meeting. Edinburgh, 2013
- *Poster* D Navarro Jimenez, **J Puxeu Vaqué**, R de Blas Piñol and M C Lizuain. Study of the recombination correction in PDD curves for flattening filter free (FFF) Beams. ESTRO Anniversary Conference. London 2011
- *Poster* **J Puxeu Vaqué** , P D Correa, A Shenoy, D J Husband, H M O Mayles. Does Planned-Dose to Organs-At-Risk Reflect Delivered-Dose in Head & Neck Intensity Modulated Radiotherapy? ESTRO Anniversary Conference. London 2011
- *Poster* P. Saldaña Gutierrez, S Llácer Martos, D Navarro Jiménez, **J Puxeu Vaqué**, M C Lizuain Arroyo. Establecimiento del estado de referéncia inicial de un acelerador lineal Varian True Beam. II Congreso conjunto de las Sociedades Españolas de Fisica Médica y Protección Radiológica. Sevilla 2011.(commissioning of TrueBeam- II National congress of the Medical Physics and Radioprotection Spanish societies)
- *Poster* **J Puxeu Vaqué**, I Modolell i Farré, E Zardoya, M C Lizuain, M Macia, A Lucas: Feasibility study of the use of RapidArc in Stereotactic Radiotherapy 29 ESTRO Congress. Barcelona 2010
- *Oral Communication* **J Puxeu**, I Modolell, E Zardoya, MC Lizuain, M Macià, A Lucas. Uso de RapidArc en tratamientos de radiocirugía. XII Congreso de la Sociedad Española de Radiocirugía, Barcelona 2010

(Use of RapidArc in Radiosurgery treatments- XII Congress of the National society in radiosurgery)

- *Poster* **J Puxeu Vaqué**, M C Lizuain Arroyo, I. Modolell Farré, R. de Blas Pinol, C Picon Olmos, F Pino Sorroche, I Sancho Kolster, J Vilar Palop and D Navarro Gimenez. An Analytical function to estimate backscatter contribution from jaws for small photon beams 10th Biennial ESTRO Meeting on Physics and Radiation Technology for clinical Radiotherapy. Maastricht 2009
- *Poster C* Picón Olmos, **J Puxeu Vaqué**, I Modolell i Farré, M C Lizuain Arroyo and D Navarro Jiménez. Utilización de películas radiocrómicas para los controles dosimétricos de aplicadores de Ru-106. XVII Congreso Español de Física Médica, Alicante (Spain) 2009 (Use of radiochromic films for dosimetric controls for Ru-106 applicators - XVII National Spanish congress in Medical Physics)
- *Poster* I Modolell i Farré, F Pino Sorroche, I Sancho Kolster, R de Blas Piñol, C Picón Olmos, **J Puxeu Vaqué**, M C Lizuain Arroyo. Calibración de películas radiocrómicas mediante campo dinámico. XVII Congreso Español de Física Médica, Alicante (Spain) 2009 (Calibration of radiochromic films using a dynamic treatment field - XVII National Spanish congress in Medical Physics)
- *Oral Communication* **J Puxeu Vaqué**, I Sancho Kolster, J Vilar Palop. Controls de qualitat específics que es duen a terme en un tractament de radioteràpia d'intensitat modulada (IMRT). II Jornada de Biofísica. Barcelona. 2007 (Specific quality controls are carried out in an intensity modulated radiotherapy treatment(IMRT)- II meeting in biophysics)

- *Poster* **J. Puxeu Vaqué**, I Sancho Kolster, M C Lizuain Arroyo. Performance tests of a PinPoint ionization chamber following the IEC Standard. 9th Biennial ESTRO Meeting on Physics and Radiation Technology for clinical Radiotherapy. Barcelona 2007

Articles in peer-reviewed journals

- M F Belosi, M Rodriguez, A Fogliata, L Cozzi, J Sempau, A Clivio, G Nicolini, E Vanetti, H Krauss, C Khamphan,P Fenoglietto, **J Puxeu**, D Fedele, P Mancosu and L Brualla. Monte Carlo simulation of TrueBeam flattening-filter-free beams using varian phase-space files: comparison with experimental data. *Med. Phys.*, (41): 051707–01–11 , 2014
- S.Lang, G. Reggiori, **J.Puxeu Vaqué**, C.Calle, J. Hrbacek, S.Klöck, M. Scorsetti, L. Cozzi and P. Mancosu. Pretreatment quality assurance of flattening filter free beams on 224 patients for intensity modulated plans: A multicentric study. *Med. Phys.* (39):1351–1356, 2012

Articles in preparation

- **J Puxeu Vaqué**, W H Nailon, M A Duch Guillen, MC Lizuain Arroyo, A Fogliata, M Ginjaume. Field Output Factor Determination in Unflattened Small Field Photon Beams: Detector Response and Influence of Set-up.
- **J Puxeu Vaqué**, W H Nailon,A P Sankar, M A Duch Guillen. PUMA, a method to predict motion and modulation effects on lung SABR treatments using volumetric modulated arc therapy.

- **J Puxeu Vaqué**, W H Nailon,A P Sankar, S Serridge. Fast and accurate method for dose skin estimation in SABR.
- **J Puxeu Vaqué**, M A Duch Guillen, M C Lizuain Arroyo, W H Nailon, M Ginjaume. Influence of geometric inaccuracies on the beam quality correction factors k_{QQo} in three ionization chambers.

Bibliography

[1] International Atomic Energy Agency. *Relative biological effectiveness in ion beam therapy*, Technical report TRS–461, Vienna, Austria,, 2008.

[2] I Herruzo, A Romero, J andPalacios, A Mañas, P Samper, and E Bayo. Libro Blanco SEOR XXI. 2010.

[3] F H Attix. *Introduction to radiological physics and radiation dosimetry.* 1986.

[4] A Niroomand-Rad, C R Blackwell, B M Coursey, K P Gall, J M Galvin, W L McLaughlin, A S Meigooni, R Nath, J E Rodgers, and C G Soares. Radiochromic film dosimetry: Recommendations of AAPM Radiation Therapy Committee Task Group 55. *Med. Phys.*, 25:2093–2115, 1998.

[5] P. Andreo, D.T. Burns, K. Hohlfeld, M.S. Huq, T. Kanai, F. Laitano, V. Smyth, and S. Vynckier. Absorbed dose determination in external beam radiotherapy. trs-398. Technical report, International Atomic Energy Agency, 2000.

[6] Nahum A. E. *Calculations of electron flux spectra in water irradiated with megavoltage electron and photon beams with applications to dosimetry.* PhD thesis, University of Edinburgh, 1976.

[7] Nahum A E. Water/air mass stopping power ratios for megavoltage photon and electron beams. *Phys. Med. Biol.*, 23:24–38, 1978.

[8] P. Andreo, L.N. Rodrigues, L. Lindborg, and T. Kraepelien. On the calibration of plane-parallel ionization chambers for electron beam dosimetry. *Phys. Med. Biol.*, (37):1147–1165, 1992.

[9] ÅPalm and O.M. Mattsson. Experimental study on the influence of the central electrode in Farmer-type ionization chambers Experimental study on the influence of the central electrode in Farmer-type ionization chambers. *Phys. Med. Biol.*, 44:1299–1308.

[10] P.R Almond and H. Svensson. Ionization chamber dosimetry for photon and electron beams Theoretical considerations. *Acta Radiol. Ther. Phys. Biol.*, (16):177–186, 1977.

[11] M.T. Gillin. The effect of thickness of the waterproofing sheath on the calibration of photon and electron beams. *Med. Phys.*, 12(2):234–236, 1985.

[12] William F. Hanson. Effects of plastic protective caps on the calibration of therapy beams in water. *Med. Phys.*, 12(2):243–248, 1985.

[13] IAEA,Vienna. *Absorbed- dose determination with ionization chambers in electron and photon beams having energies between 1 and 50 MeV*, National and International Standardization of Radiation Dosimetry, Proc. Symp. Atlanta, 1977, 1978.

[14] M. Kristensen. Measured influence of the central electrode diameter and material on the response of a graphite ionisation chamber to cobalt-60 gamma rays. *Phys. Med. Biol.*, (28):1269–1278, 1983.

[15] L.O. Mattsson. *Application of the water calorimeter, Fricke dosimeter and ionization chamber in clinical dosimetry: an evaluation of correction factors and interaction coefficients.* PhD thesis, Goteborg University, Sweden, 1984.

[16] H. Nyström and M. Karlsson. Correction factors applied to plane-parallel ionization chambers. *Phys. Med. Biol.*, (38):311–322, 1993.

[17] IAEA,Vienna. *Investigation of some aspects of the IAEA code of practice for absorbed dose determination in photon and electron beams Measurement Assurance in Dosimetry*, Proc. IAEA Symp, 1994.

[18] IAEA,Vienna. *Optimum calibration of NACP type plane parallel ionization chambers for absorbed dose determination in low energy electron beams Measurement Assurance in Dosimetry*, Proc. IAEA Symp, 1994.

[19] R. Nath and R.J. Schulz. Calculated response and wall correction factors for ionization chambers exposed to 60Co gamma-rays. *Med. Phys.*, (8):85–93, 1981.

[20] A.C. McEwan and V.G. Smyth. Comments on Calculated response and wall correction factors for ionization chambers exposed to 60Co gamma-rays. *Med. Phys.*, (11):216–218, 1984.

[21] D.W.O. Rogers, A.F. Bielajew, and A.E. Nahum. Ion chamber response and Awall correction factors in a 60Co beam by Monte Carlo simulation. *Phys. Med. Biol.*, (30):429–443, 1985.

[22] C. Ma and A.E. Nahum. Effect of size and composition of the central electrode on the response of cylindrical ionization chambers in high-energy photon and electron beams. *Phys. Med. Biol.*, 38(2):267–290, 1993.

[23] J. Sempau, P. Andreo, J. Aldana, J. Mazurier, and F. Salvat. Electron beam quality correction factors for plane-parallel ionization chambers: Monte Carlo calculations using the PENELOPE system. *Phys. Med. Biol.*, 49(18):4427–4444, September 2004.

[24] I J Das, G X Ding, and A Ahnesjö. Small fields: Nonequilibrium radiation dosimetry. *Med. Phys.*, 35(1):206–215, 2008.

[25] J Dutreix, A Dutreix, and M Tubiana. Electronic equilibrium and transition stages. *Phys. Med. Biol.*, 177–190, 1965.

[26] G Chierego, C Marchetti, R C Avanzo, F Pozza, and F Colombo. Dosimetric considerations on multiple arc stereotaxic radiotherapy. *Radiother. Oncol.*, 12:141–152, 1988.

[27] B. E. Bjärngard. Doses on the central axes of narrow 6-MV x-ray beams. *Med. Phys.*, 17(5):794–799, 1990.

[28] R. Alfonso, P. Andreo, R. Capote, M. S. Huq, W. Kilby, P. Kjall, T. R. Mackie, H. Palmans, K. Rosser, J. Seuntjens, W. Ullrich, and S. Vatnitsky. A new formalism for reference dosimetry of small and nonstandard fields. *Med. Phys.*, 35(11):5179–5186, 2008.

[29] R. Capote, F. Sanchez-Doblado, A. Lagares, J.I. Arrans, R Hartmann, and H. Gunther. An EGSnrc Monte Carlo study of the microionization chamber for reference dosimetry of narrow irregular IMRT beamlets. *Med. Phys.*, 31(9):2416, 2004.

[30] P Francescon, S. Cora, C. Cavedon, P. Scalchi, S. Reccanello, and F Colombo. Use of a new type of radiochromic film, a new parallel-plate micro-chamber, mosfets, and tld 800 microcubes in the dosimetry of small beams. *Med. Phys.*, 25:503–511, 1998.

[31] F Salvat, J.M. Fernandez-Varea, and J. Sempau. *PENELOPE: A Code System for Monte Carlo Simulation of Electron and Photon Transport.* Issy-les-moulineaux, France: OECD Nuclear Energy Agency, 2003. Available in pdf format at http://www.nea.fr.

[32] Stanley H. Benedict, Kamil M. Yenice, David Followill, James M. Galvin, William Hinson, Brian Kavanagh, Paul Keall, Michael Lovelock, Sanford Meeks, Lech Papiez, Thomas Purdie, Ramaswamy Sadagopan, Michael C. Schell, Bill Salter, David J. Schlesinger, Almon S. Shiu, Timothy Solberg, Danny Y. Song, Volker Stieber, Robert Timmerman, Wolfgang A. Tome, Dirk Verellen, Lu Wang, and Fang-Fang Yin. Stereotactic body radiation therapy: The report of aapm task group 101. *Med. Phys.*, 37(8):4078–4101, 2010.

[33] J. Boda-Heggemann, S. Mai, J. Fleckenstein, K. Siebenlist, A. Simeonova, M. Ehmann, V. Steil, F. Wenz, F Lohr, and F. Stieler. Flattening-filter-free intensity modulated breath-hold image-guided sabr (stereotactic ablative radiotherapy) can be applied in a 15-min treatment slot. *Radiother. Oncol.*, 109(3):505–509, 2013.

[34] N.C Van der Voort van Zyp, J.B. Prevost, M.S. Hoogeman, J. Praag, B. Van der Holt, P.C. Levendag, R.J. Van Klaveren, P. Pattynama, and J.J. Nuyttens. Stereotactic radiotherapy with real-time tumor tracking for non-small cell lung cancer: clinical outcome. *Radiother. Oncol.*, 91:296–300, 2009.

[35] M.S. Hoogeman, J.J. Nuyttens, P.C. Levendag, and B.J. Heijmen. Time dependence of intrafraction patient motion assessed by repeat stereoscopic imaging. *Int. J. Radiat. Oncol. Biol. Phys.*, 70:609–618, 2008.

[36] T.G. Purdie, J.P. Bissonnette, K. Franks, A. Bezjak, D. Payne, F. Sie, M.B. Sharpe, and D.A. Jaffray. Cone-beam computer tomography for online image guidance of lung stereotactic radiotherapy: localization, verification, and intrafraction tumor position. *Int. J. Radiat. Oncol. Biol. Phys.*, 68:243–252, 2007.

[37] C.J.A Haasbeek, S. Senan, E.F. Smit, M.A. Paul, B.J. Slotman, and F.J. Lagerwaard. Critical Review of Non-Surgical Treatment Options for Stage I Non-Small Cell Lung Cancer. *Oncologist*, 13:309–319, 2008.

[38] A. Chi, Z. Liao, N.P. Nguyen, J. Xu, B. Stea, and R. Komaki. review of the patterns of failure following stereotactic body radiation therapy in early-stage non-small-cell lung cancer: clinical implications. *Radiother. Oncol.*, 94:1–11, 2010.

[39] D Palma, O. Visser, F.J. Lagerwaard, J. Belderbos, B.J. Slotman, and S. Senan. The impact of introducing stereotactic lung radiotherapy for elderly patients with stage i nsclc: A population-based time-trend analysis. *J. Clin. Oncol.*, 28:5153–5159, 2010.

[40] D. Palma and S. Senan. Stereotactic radiation therapy: changing treatment paradigms for stage i non-small cell lung cancer. *Curr. Opin. Oncol.*, 23:133–139, 2011.

[41] F.J. Lagerwaard, N.E. Verstegen, C.J. Haasbeek, B.J. Slotman, M.A. Paul, E.F. Smit, and S. Senan. Outcomes of stereotactic ablative radiotherapy in patients with potentially operable stage i non-small cell lung cancer. *Int. J. Radiat. Oncol. Biol. Phys.*, 83:348–353, 2012.

[42] T.B. Jr Lanni, I.S. Grills, LL. Kestin, and J.M. Robertson. Stereotactic radiotherapy reduces treatment cost while improving overall sur-

vival and local control over standard fractionated radiation therapy for medically inoperable non-small-cell lung cancer. *Am. J. Clin. Oncol.*, 34(5):494–498, 2011.

[43] R.I. Berbeco, C.J Pope, and S.B. Jiang. Measurement of the interplay effect in lung IMRT treatment using EDR2 films. *J. Appl. Clin. Med. Phys.*, 7(4):33–42, 2006.

[44] C.X. Yu, D.A. Jaffray, and J.W. Wong. The effects of intra-fraction organ motion on the delivery of dynamic intensity modulation. *Phys. Med. Biol.*, 43(1):91–104, 1998.

[45] T. Bortfeld, K. Jokivarsi, M. Goitein, J Kung, and S.B. Jiang. Effects of intra-fraction motion on IMRT dose delivery: statistical analysis and simulation. *Phys. Med. Biol.*, 47(13):2203–2220, 2002.

[46] C.S. Chui, E. Yorke, and Hong L. The effects of intra-fraction organ motion on the delivery of intensity-modulated field with a multileaf collimator. *Med. Phys.*, 30(7):1736–1746, 2003.

[47] S.B. Jiang, C. Pope, K.M. Al Jarrah, J.H. Kung, T. Bortfeld, and G.T.Y. Chen. An experimental investigation on intra-fractional organ motion effects in lung imrt treatments. *Phys. Med. Biol.*, 48(12):1773, 2003.

[48] M Schaefer, M.W. MÃŒnter, C. Thilmann, F. Sterzing, P. Haering, S.E. Combs, and J. Debus. Influence of intra-fractional breathing movement in step-and-shoot imrt. *Phys. Med. Biol.*, 49(12):N175, 2004.

[49] E. Nelms, B.E.and Ehler, H. Bragg, and Tome W.A. Quality assurance device for four-dimensional imrt or sbrt and respiratory gating using

patient-specific intrafraction motion kernels. *J. Appl. Clin. Med. Phys.*, 8(4):2683, 2007.

[50] L.E. Court, J. Seco, X.Q. Lu, K. Ebe, C. Mayo, D. Ionascu, B. Winey, N. Giakoumakis, M. Aristophanous, R. Berbeco, J. Rottman, M. Bogdanov, D. Schofield, and T. Lingos. Use of a realistic breathing lung phantom to evaluate dose delivery errors. *Med. Phys.*, 37(11):5850–5857, 2010.

[51] L.E. Court, M. Wagar, R. Berbeco, A. Reisner, B. Winey, D. Schofield, D. Ionascu, A.M. Allen, R. Popple, and T. Lingos. Evaluation of the interplay effect when using rapidarc to treat targets moving in the craniocaudal or right-left direction. *Med. Phys.*, 37(1):4–11, 2010.

[52] M. Rao, J. Wu, D. Cao, T. Wong, V. Mehta, D. Shepard, and J. Ye. Dosimetric impact of breathing motion in lung stereotactic body radiotherapy treatment using image- modulated radiotherapy and volumetric modulated arc therapy. *Int. J. Radiat. Oncol. Biol. Phys.*, 83(2):e251–e256, 2012.

[53] V. Feygelman, C. Stambaugh, G. Zhang, D. Hunt, D. Opp, T.K. Wolf, and B.E. Nelms. Motion as a perturbation: measurement-guided dose estimates to moving patient voxels during modulated arc deliveries. *Med. Phys.*, 40(2):021708, 2013.

[54] B. Zhao, Y. Yang, T. Li, X. Li, D.E. Heron, and M.S. Huq. Dosimetric effect of intrafraction tumor motion in phase gated lung stereotactic body radiotherapy. *Med. Phys.*, 39(11):6629–6637, 2012.

[55] X. Li, Y. Yang, T. Li, K. Fallon, and M.S. Heron, D.E. Huq. Dosimetric effect of respiratory motion on volumetric-modulated arc therapy-

based lung SBRT treatment delivered by TrueBeam machine with flattening filter-free beam. *J. Appl. Clin. Med. Phys.*, 6(14):4370, 2013.

[56] C. Stambaugh, B.E. Nelms, T. Dilling, C. Stevens, K. Latifi, G. Zhang, E. Moros, and V. Feygelman. Experimentally studied dynamic dose interplay does not meaningfully affect target dose in VMAT SBRT lung treatments. *Med. Phys.*, 9(40):091710, 2013.

[57] W. Zou, L. Yin, J. Shen, M.N. Corradetti, M. Kirk, R. Munbodh, P. Fang, S.K. Jabbour, C.B. Simone, N.J. Yue, R. Rengan, and B.K. Teo. Dynamic simulation of motion effects in IMAT lung SBRT. *Radiat. Oncol.*, (9):225, 2014.

[58] C.L. Ong, M. Dahele, B.J. Slotman, and W.F. Verbakel. Dosimetric impact of the interplay effect during stereotactic lung radiation therapy delivery using flattening filter-free beams and volumetric modulated arc therapy. *Int. J. Radiat. Oncol. Biol. Phys.*, 4(86):743–748, 2013.

[59] U. Titt, O.N. Vassiliev, F. Pönisch, L. Dong, H. Liu, and R. Mohan. A flattening filter free photon treatment concept evaluation with Monte Carlo. *Med. Phys.*, 6(33):1595–1602, 2006.

[60] U. Titt, O.N. Vassiliev, F. Pönisch, S.F. Kry, and R. Mohan. Monte Carlo study of backscatter in a flattening filter free clinical accelerator. *Med. Phys.*, 9(33):3270–3273, 2006.

[61] O.N. Vassiliev, U. Titt, F. Pönisch, S.F. Kry, R. Mohan, and M.T. Gillin. Dosimetric properties of photon beams from a flattening filter free clinical accelerator. *Phys. Med. Biol.*, 7(51):1907–1917, 2006.

[62] J. Cashmore. The characterization of unflattened photon beams from a 6 mv linear accelerator. *Phys. Med. Biol.*, 7(53):1933–1946, 2008.

[63] G. Kragl, S. af Wetterstedt, B. Knausl, M. Lind, P. McCavana, T. Knoos, B. McClean, and D. Georg. Dosimetric characteristics of 6 and 10mv unflattened photon beams. *Radiother. Oncol.*, 1(93):141–146, 2009.

[64] Oleg N Vassiliev, U Titt, S F Kry, F Pönisch, M T Gillin, and R Mohan.

[65] J. Hrbacek, S. Lang, and S. Klöck. Commissioning of photon beams of a flattening filter-free linear accelerator and the accuracy of beam modeling using an anisotropic analytical algorithm. *Int. J. Radiat. Oncol. Biol. Phys.*, 80(4):1228–1237, 2011.

[66] Z. Chang, Q Wu, J. Adamson, L. Ren, J Bowsher, H. Yan, A. Thomas, and F.F. Yin. Commissioning and dosimetric characteristics of TrueBeam system: composite data of three TrueBeam machines. *Med. Phys.*, 11(39):6981–7018, 2012.

[67] A. Fogliata, R. Garcia, T. Knoos, G. Nicolini, A. Clivio, E. Vanetti, C. Khamphan, and L. Cozzi. Definition of parameters for quality assurance of flattening filter free (FFF) photon beams in radiation therapy. *Med. Phys.*, 10(39):6455–6464, 2012.

[68] S Lang, G Reggiori, J Puxeu Vaqué, C Calle, J Hrbacek, S Klock, M Scorsetti, L Cozzi, and P Mancosu. Pretreatment quality assurance of flattening filter free beams on 224 patients for intensity modulated plans: a multicentric study. *Med. Phys.*, 39:1351–6, 2012.

[69] M F Belosi, M Rodriguez, A Fogliata, L Cozzi, J Sempau, A Clivio, G Nicolini, E Vanetti, H Krauss, C Khamphan, P Fenoglietto, J Puxeu, D Fedele, P Mancosu, and L Brualla. Monte Carlo simulation of True-

Beam flattening-filter-free beams using varian phase-space files: comparison with experimental data. *Med. Phys.*, 41:051707, 2014.

[70] J Wulff, J T Heverhagen, and K Zink. Monte-Carlo-based perturbation and beam quality correction factors for thimble ionization chambers in high-energy photon beams. *Phys. Med. Biol.*, 53(11):2823–36, 2008.

[71] International Atomic Energy Agency. *The METAS absorbed dose to water calibration service for high energy photon and electron beam radiotherapy*, in Proceedings of the International Symposium on Standards and Codes of Practice in Medical Radiation Dosimetry, Vienna, Austria,, 2003.

[72] D M González-Castaño, G H Hartmann, F Sánchez-Doblado, F Gómez, R-P Kapsch, J Pena, and R Capote. The determination of beam quality correction factors: Monte Carlo simulations and measurements. *Phys. Med. Biol.*, 54(15):4723–41, 2009.

[73] A. S. Guerra, R.F. Laitano, and M. Pimpinella. Experimental determination of the beam quality dependence factors, kQ, for ionization chambers used in photon and electron dosimetry. *Phys. Med. Biol.*, 40(7):1177–1190, 1995.

[74] Medizinische Physik. *44. Jahrestagung der Deutschen Gesellschaft fÃŒr Medizinische Physik*, Köln, Germany, September 2013.

[75] J. P. Seuntjens, C. K. Ross, K. R. Shortt, and D. W. O. Rogers. Absorbed–dose beam quality conversion factors for cylindrical chambers in high energy photon beams. *Med. Phys.*, 27(12):2763, 2000.

[76] P. Sharpe. Progress report on radiation dosimetry at npl. Technical report, BIPM Report CCRI /99-20, 1999.

[77] K.R. Shortt, C.K. Ross, M. Schneider, K. Hohlfeld, M. Roos, and A.M. Perroche. A comparison of absorbed dose standards for high-energy x-rays. *Phys. Med. Biol.*, 38(12):1937, 1993.

[78] S.M. Vatnitsky, J.V. Siebers, and D.W. Miller. Calorimetric determination of the absorbed dose-to-water beam quality correction factor kq for high-energy photon beams. *Med. Phys.*, 22(11):1749, 1752.

[79] H. Palmans, W. Mondelaers, and H. Thierens. Absorbed dose beam quality correction factors kq for the ne2571 chamber in a 5 mv and a 10 mv photon beam. *Phys. Med. Biol.*, 44(3):647–663, 1999.

[80] International Atomic Energy Agency. *A Test of TPR10,20 as a Beam Quality Specifier for High-Energy Photon Beams*, IAEA-SM-330/10, Proceedings of Symposium on Measurement Assurance in Dosimetry, Vienna, Austria, 1994.

[81] International Atomic Energy Agency. *Comparisons and Calibrations at the Bureau International des Poids et Mesures in the field of X and g rays*, IAEA-SM-330/22, Proceedings of Symposium on Measurement Assurance in Dosimetry, Vienna, Austria,, 1994.

[82] M.R. McEwen. Measurement of ionization chamber absorbed dose k[sub Q] factors in megavoltage photon beams. *Med. Phys.*, 37(5):2179–2193, 2010.

[83] B. R. Muir and D. W. O. Rogers. Monte Carlo calculations of k[sub Q], the beam quality conversion factor. *Med. Phys.*, 37(11):5939–5950, 2010.

[84] F. Erazo and A.M. Lallena. Calculation of beam quality correction

factors for various thimble ionization chambers using the Monte Carlo code PENELOPE. *Physica medica*, 29(2):163–170, 2013.

[85] A. Krauss and R.P. Kapsch. Experimental determination of kq factors for cylindrical ionization chambers in 10 cm x10 cm and 3 cm x 3 cm photon beams from 4 mv to 25 mv. *Phys. Med. Biol.*, 59(15):4227–4246, 2014.

[86] M Le Roy, L de Carlan, F Delaunay, M Donois, P Fournier, a Ostrowsky, a Vouillaume, and J M Bordy. Assessment of small volume ionization chambers as reference dosimeters in high-energy photon beams. *Phys. Med. Biol.*, 56(17):5637–50, 2011.

[87] P. Andreo, J. Wulff, D.T. Burns, and H. Palmans. Consistency in reference radiotherapy dosimetry: resolution of an apparent conundrum when (60)Co is the reference quality for charged-particle and photon beams. *Phys. Med. Biol.*, 58(19):6593–6621, 2013.

[88] B.R. Muir. Ion chamber absorbed dose calibration coefficients, N(D,w), measured at ADCLs: distribution analysis and stability. *Med. Phys.*, 42(4):1546–1554, 2015.

[89] J. E. Morales, S.B. Crowe, R. Hill, N. Freeman, and J.V. Trapp. Dosimetry of cone-defined stereotactic radiosurgery fields with a commercial synthetic diamond detector. *Med. Phys.*, 41(11):111702, 2014.

[90] P. Francescon, S. Beddar, N. Satariano, and I.J. Das. Variation of kQclin,Qmsr (fclin,fmsr) for the small-field dosimetric parameters percentage depth dose, tissue-maximum ratio, and off-axis ratio. *Med. Phys.*, 41(10):101708, 2014.

[91] P.H. Charles, G. Cranmer-Sargison, D.I. Thwaites, T. Kairn, S.B. Crowe, G. Pedrazzini, T. Aland, J. Kenny, C.M. Langton, and J.V. Trapp. Design and experimental testing of air slab caps which convert commercial electron diodes into dual purpose, correction-free diodes for small field dosimetry. *Med. Phys.*, 41(10):101701, 2014.

[92] T.S. Underwood, H.C. Winter, M. Hill, and J.D. Fenwick. Detector density and small field dosimetry: integral versus point dose measurement schemes. *Med. Phys.*, 40(8):082102, 2013.

[93] C. Bassinet, C. Huet, S. Derreumaux, M. Brunet, G .and Chéa, M. Baumann, T. Lacornerie, S. Gaudaire-Josset, F. Trompier, P. Roch, G. Boisserie, and I. Clairand. Small fields output factors measurements and correction factors determination for several detectors for a CyberKnife and linear accelerators equipped with microMLC and circular cones. *Med. Phys.*, 40(7):071725, 2013.

[94] P. Francescon, S. Cora, and N. Satariano. Calculation of k(Q(clin),Q(msr)) (f(clin),f(msr)) for several small detectors and for two linear accelerators using Monte Carlo simulations. *Med. Phys.*, 38(12):6513–27, 2011.

[95] P. Francescon, W. Kilby, N. Satariano, and S. Cora. Monte Carlo simulated correction factors for machine specific reference field dose calibration and output factor measurement using fixed and iris collimators on the CyberKnife system. *Phys. Med. Biol.*, 57(12):3741–58, 2012.

[96] D. Czarnecki and K. Zink. Corrigendum: Monte Carlo calculated

correction factors for diodes and ion chambers in small photon fields. *Phys. Med. Biol.*, 59(3):791–794, 2014.

[97] A. Ralston, P. Liu, K. Warrener, D. McKenzie, and N. Suchowerska. Small field diode correction factors derived using an air core fibre optic scintillation dosimeter and EBT2 film. *Phys. Med. Biol.*, 57(9):2587–602, 2012.

[98] M Bucciolini, F Banci Buonamici, S. Mazzocchi, C De Angelis, S Onori, and G a. P Cirrone. Diamond detector versus silicon diode and ion chamber in photon beams of different energy and field size. *Med. Phys.*, 30(8):2149, 2003.

[99] K Eklund and A Ahnesjö. Spectral perturbations from silicon diode detector encapsulation and shielding in photon fields. *Med. Phys.*, 37(11):6055, 2010.

[100] Alison J D Scott, Sudhir Kumar, Alan E Nahum, and John D Fenwick. Characterizing the influence of detector density on dosimeter response in non-equilibrium small photon fields. *Phys. Med. Biol.*, 57(14):4461–76, 2012.

[101] International Atomic Energy Agency. *Absorbed Dose Determination in Photon and Electron Beams: An International Code of Practice*, Technical report TRS–461, Vienna, Austria,, 1987.

[102] E Gete, C Duzenli, M P Milette, A Mestrovic, D Hyde, A M Bergman, and T Teke. A Monte Carlo approach to validation of FFF VMAT treatment plans for the TrueBeam linac. *Med. Phys.*, 40(2):021707–01/13, 2013.

[103] W Lechner, H Palmans, L Sölkner, P Grochowska, and D Georg. Detector comparison for small field output factor measurements in flattening filter free photon beams. *Radiother. Oncol.*, 109(3):356–60, 2013.

[104] International Electrotechnical Commission (IEC). *Dosimeters with ionization chambers as used in radiotherapy*, IEC–60731, 1997.

[105] M Ginjaume, X Ortega, M A Duch, N Jornet, and A SÃ¡nchez-Reyes. Characteristics of LiF:Mg,Cu,P for clinical applications. *Radiation Protection Dosimetry*, 85(1–4):389–91, 1999.

[106] *penEasy: a modular main program and voxelized geometry package for PENELOPE*, www.upc.edu/inte/downloads/penEasy.htm, 2009.

[107] G Mora, A Maio, and D W O Rogers. Monte Carlo simulation of a typical 60Co therapy source. *Med. Phys.*, 26(11):2494–2502, 1999.

[108] L Brualla, F Salvat, and R Palanco-Zamora. Efficient Monte Carlo simulation of multileaf collimators using geometry-related variance-reduction techniques. *Phys. Med. Biol.*, 54:4131–4149, 2009.

[109] M A Duch, P Carrasco, N Jornet, F Hernandez, R Camats, O Jordi, and M Ribas. Detector comparison for dose measurements un the build-up zone. *Radiother. Oncol.*, 115 (sup 1):S426, 2015.

[110] M Bueno, P Carrasco, N Jornet, C Muñoz Montplet, and M A Duch. On the suitability of ultrathin detectors for absorbed dose assessment in the presence of high-density heterogeneities. *Med. Phys.*, 41(8):081710–1/12, 2009.

[111] G Cranmer-Sargison, S Weston, J A Evans, N P Sidhu, and D I Thwaites. Implementing a newly proposed Monte Carlo based small

field dosimetry formalism for a comprehensive set of diode detectors. *Med. Phys.*, 38(12):6592–602, 2011.

[112] D A Low, W B Harms, S Mutic, and J A Purdy. A technique for the quantitative evaluation of dose distributions. *Med. Phys.*, (25):656–661, 1998.

[113] D Navarro Jimenez, J Puxeu Vaqué, R De Blas Piñol, and M C Lizuain. Study of the recombination correction in PDD curves for flattening filter free (FFF) Beams. *Radiother. Oncol.*, (01/2011):99, 2011.

[114] S F Kry, R Popple, A Molineu, and D S Followill. Ion recombination correction factors (P ion) for Varian TrueBeam high–dose–rate therapy beams. *J. Appl. Clin. Med. Phys.*, 13(6):3803, 2012.

[115] SABR UK Consortium. Stereotactic Ablative Body Radiation Therapy (SABR): A Resource. *Version 4.0, January 2013*, http://actionradiotherapy.org/wp-content/uploads/2014/03/UK-SABR-Consortium-Guidelines.pdf, 2013.

[116] Andrea L. McNiven, Michael B. Sharpe, and Thomas G. Purdie. A new metric for assessing IMRT modulation complexity and plan deliverability. *Med. Phys.*, 37:505–15, 2010.

[117] J M Park, S Y Park, H Kim, J H Kim, J Carlson, and SJ Ye. Modulation indices for volumetric modulated arc therapy. *Phys. Med. Biol.*, 59(23):7315–40, 2014.

[118] W Du, S H Cho, X Zhang, K E Hoffman, and R J Kudchadker. Quantification of beam complexity in intensity-modulated radiation therapy treatment plans. *Med. Phys.*, 41(2):021716, February 2014.

[119] R Core Team. *R: A Language and Environment for Statistical Computing.* R Foundation for Statistical Computing, Vienna, Austria, http://www.R-project.org/, 2013.

[120] A Krauss and R P Kapsch. Calorimetric determination of kq factors for ne 2561 and ne 2571 ionization chambers in 5 cm x 5 cm and 10 cm x 10 cm radiotherapy beams of 8 mv and 16 mv photons. *Phys. Med. Biol.*, 52:6243–6259, 2007.

[121] A Krauss and R P Kapsch. Calorimetric determination of kq factors for ne 2561 and ne 2571 ionization chambers in 5 cm x 5 cm and 10 cm x 10 cm radiotherapy beams of 8 mv and 16 mv photons. *Phys. Med. Biol.*, 53:1152–1152, 2008.

[122] J Wulff, J T Heverhagen, K Zink, and I Kawrakow. Investigation of systematic uncertainties in Monte Carlo-calculated beam quality correction factors. *Phys. Med. Biol.*, 55(16):4481–4493, 2010.

[123] S Tanny, N Sperling, and E I Parsai. Correction factor measurements for multiple detectors used in small field dosimetry on the Varian Edge radiosurgery system. *Med. Phys.*, 42(9):5370–6, 2015.

[124] H Benmakhlouf, J Sempau, and P Andreo. Output correction factors for nine small field detectors in 6 MV radiation therapy photon beams: a PENELOPE Monte Carlo study. *Med. Phys.*, 41(4):041711, 2014.